

Syracuse University

SURFACE

Dissertations - ALL

SURFACE

May 2019

Use of Computational Electromagnetics to Enhance the Accuracy and Efficiency of Antenna Pattern Measurements

Heng Chen
Syracuse University

Follow this and additional works at: <https://surface.syr.edu/etd>



Part of the [Engineering Commons](#)

Recommended Citation

Chen, Heng, "Use of Computational Electromagnetics to Enhance the Accuracy and Efficiency of Antenna Pattern Measurements" (2019). *Dissertations - ALL*. 1008.

<https://surface.syr.edu/etd/1008>

This Dissertation is brought to you for free and open access by the SURFACE at SURFACE. It has been accepted for inclusion in Dissertations - ALL by an authorized administrator of SURFACE. For more information, please contact surface@syr.edu.

Abstract

The objective of this dissertation is to illustrate that computational electromagnetics can be used to improve the accuracy and efficiency of antenna pattern measurements.

This can be accomplished in many different ways, such as moving a single probe over the measurement plane to generate accurate planar near field to far field transformation methodology over the classical Fourier based modal expansion methods. Also, one can use an array of probes instead of moving a single probe over the measurement plane to eliminate the inaccuracy of a mechanical movement of the probe antenna over a large planar surface and make the measurement methodology more accurate and efficient. Another unique feature of this methodology is that as long as the sizes of the measurement planes are chosen to be approximately equal to or larger than the size of the actual source plane of the antenna under test, one is guaranteed to obtain the accurate results.

In addition, other two approaches are proposed which under some conditions to further increase the efficiency of the whole processes of the methodology. For example, for a linearly polarized antenna, performance is often described in terms of its principal E-plane and H-plane patterns. If that is the goal, then one can use a planar dipole probe array to measure the near field over a sector and then use that to obtain the far field pattern along principal planes with engineering accuracy and so precision mechanical measurement gadgets will not be required and thus minimizing the cost and speeding up the measurement process. Another scenario is that the near field data contain complex numbers, and it's very difficult to measure the complex data, especially for high frequency applications, say at M,

V and W-bands. One can still obtain acceptable far field results by using the amplitude only data of the near field measurements, which significantly reduced the workload of the measurements, hence increased the efficiency.

The whole methodology is accomplished by solving for the equivalent magnetic current over a plane near the original source antenna under test and then employing the Method of Moments approach to solve for the equivalent magnetic currents on this fictitious surface. The two components of the equivalent currents can be solved independently from the two components of the measured electric fields. The resultant method of moments matrix equation can be solved very efficiently and accurately by using the iterative conjugate gradient method enhanced through the incorporation of the Fast Fourier Transform techniques. In all these approaches, there is no need to incorporate probe correction unlike in the existing approaches, no need to satisfy the Nyquist sampling criteria and a super resolution can be achieved in the solution of the equivalent magnetic current to predict the operation of the antenna. Also, the presence of evanescent fields does not make this methodology unstable unlike the Fourier based techniques.

Sample numerical results are presented to illustrate the potential of a novel planar near field to far field transformation for the planar near field measurement technique.

Use of Computational Electromagnetics to Enhance the Accuracy and Efficiency of Antenna Pattern Measurements

by

Heng Chen

B.E., Anhui Agricultural University, 2012
M.S., Syracuse University, 2014

Dissertation

Submitted in partial fulfillment of the requirements for the degree of
Doctor of Philosophy in Electrical and Computer Engineering.

Syracuse University

May 2019

Copyright © Heng Chen 2019

All Rights Reserved

Acknowledgement

I'd like to thank my advisor, Professor Tapan K. Sarkar, for his continuous support and guidance. Doing research is quite different than doing normal studies as I had for years, Prof. Sarkar really helped me a lot. He not only taught me electromagnetics, but also guided me the way of doing research from which I benefitted a lot. His experience helped me overcome many difficulties in my PhD period and made me knowledgeable.

I'd like to thank Prof. Jay K. Lee who taught me many high-level electromagnetic courses and made me very confident to understand the complicated equations in the papers. Dr. Lee also gave me a lot of valuable suggestions in my fields.

I'd like to thank all my exam committee members including Dr. Shen, Dr. Lee, Dr. Song, Dr. Gursoy and Dr. Graham. I know that it would take excessive amount of time to review my work.

I'd like to thank everyone I have met in our CEMLAB. Dr. Walid Dyab, Dr. Hongsik Moon, Mohammad Abdallah, Dr. Kai Lu, Dr. Yong Zhou, Dr. Mingda Zhu, Dr. Chainatong, Nicholas Dicara thank you all for the help and all the happy time we spend together.

I'd like to thank my parents, who supported me unconditionally all the time. I know how hard work my father did to support me a better life in America. I remember how my mother encouraged me when I feel depressed. I love you!

Table of Contents

Abstract	i
Acknowledgement	v
Table of Contents	vi
List of Figures	ix
1 Introduction	1
2 Development of the Proposed Methodology	2
3 Philosophy of the Computational Methodology	4
3.1 Brief Introduction of the Uniqueness Theorem and the Equivalence Principle... 4	
3.2 Modeling of Antenna Measurement System.....	7
4 Formulation of the Integral Equations	10
4.1 Near-Field Measurement System.....	10
4.2 Near-Field Formulations	11
4.3 Far-Field Formulations.....	14
5 Formulation of Matrix Equations From the Integral Equations	18
5.1 Discrete Formulation of the Source Plane.....	19
5.2 Discrete Formulation of the Measurement Plane.....	21
5.3 Discrete Formulation of the Integral Equations	23

6	Solution for the Matrix Equations	25
6.1	Method Choosing	25
6.2	Procedures of Conjugate Gradient Method.....	26
6.3	Brief Introduction of Toeplitz Matrix	27
6.4	Block Toeplitz Matrix	29
7	Analysis of Single Probe and Probe Array Measurements.....	32
7.1	Objective and Unique Features	32
7.2	Implementation of the Single Probe and Probe Array Measurements	33
7.3	Example7.1: Numerical results of choosing Horn antenna to be the AUT.....	35
7.4	Example7.2: Numerical results of choosing Horn array to be the AUT	40
7.5	Example7.3: Numerical results of choosing Yagi antenna to be the AUT.	45
7.6	Example7.4: Numerical results of choosing Yagi array to be the AUT.	48
8	The Influence of the Size of Square Dipole Probe Array Measurement on the Accuracy of NF-FF Pattern.....	53
8.1	Objective and Necessity of the Analysis.....	53
8.2	Implementation Procedure	54
8.3	Example 8.1: Numerical results of choosing Horn antenna to be the AUT.....	56
8.4	Example 8.2: Numerical results of choosing Horn array to be the AUT.	62
8.5	Example 8.3: Numerical results of choosing Yagi antenna to be the AUT.	71
8.6	Example 8.4: Numerical results of choosing Yagi array to be the AUT.	75

9	A Fast and Efficient Methodology for Determining the Far Field Patterns of an Antenna along Principal Planes Using a Probe Array	84
9.1	Objective and Unique Features	84
9.2	Implementation of the Methodology Over a Sector	86
9.3	Example 9.1: Numerical results of choosing Horn to be the AUT.	89
9.4	Example 9.2: Numerical results of choosing Horn array to be the AUT.	96
9.5	Example 9.3: Numerical results of choosing Yagi antenna to be the AUT.	102
9.6	Example 9.4: Numerical results of choosing Yagi Array to be the AUT.	106
10	Use Amplitude Only Data to Enhance the Efficiency of NF-FF Method	112
10.1	Objective and Necessity	112
10.2	Implementation of the Methodology	113
10.3	Example 10.1: Numerical results of choosing Horn antenna to be the AUT... ..	116
10.4	Example 10.2: Numerical results of choosing Horn Array to be the AUT.	119
10.5	Example 10.3: Numerical results of choosing Yagi antenna to be the AUT. ..	122
10.6	Example 10.4: Numerical results of choosing Yagi Array to be the AUT.	125
11	Conclusions and Future Work.....	128
	Reference	130
	Biographical Data	134

List of Figures

Fig. 3.1. Original problem.....	5
Fig. 3.2. The equivalent problem with both J and M produces the same field exterior to S as do the original sources.....	5
Fig. 3.3. Equivalent magnetic currents with an electric conductor.....	6
Fig. 3.4. Equivalent electric currents with a magnetic conductor.....	6
Fig. 3.5. Original Problem of antenna measurement.	7
Fig. 3.6. Equivalent Problem.	8
Fig. 4.1. Near-field measurement.	10
Fig. 4.2. Far-field system.	14
Fig. 5.1. Discretization of the source plane.	19
Fig. 5.2. Discretization of both source plane and measurement plane.	21
Fig. 6.1. Example of Block Toeplitz Matrix.....	29
Fig. 7.1. Near field Measurement Structure.....	33
Fig. 7.2. x-directed single probe.	36
Fig. 7.3. x-directed single probe (side view).	36
Fig. 7.4. x-directed probe array.....	37
Fig. 7.5. x-directed probe array (side view).....	37
Fig. 7.6. E total when $\phi=0$ (dB Scale).....	38
Fig. 7.7. E total when $\phi=90$ (dB Scale).....	38
Fig. 7.8. A x-directed single probe.	41
Fig. 7.9. A x-directed single probe (side view).....	41
Fig. 7.10. A x-directed probe array.....	42

Fig. 7.11. A x-directed probe array (side view).....	42
Fig. 7.12. E_{total} when $\phi = 0^\circ$ (dB Scale).	43
Fig. 7.13. E_{total} when $\phi = 90^\circ$ (dB Scale).	43
Fig. 7.14. A three-element Yagi-Uda antenna.	45
Fig. 7.15. E_{total} when $\phi = 0^\circ$ (dB Scale).	46
Fig. 7.16. E_{total} when $\phi = 90^\circ$ (dB Scale).	47
Fig. 7.17. A x-directed single probe.	49
Fig. 7.18. A x-directed single probe (side view).....	49
Fig. 7.19. A x-directed probe array.....	50
Fig. 7.20. A x-directed probe array (side view).....	50
Fig. 7.21. E_{total} when $\phi = 0^\circ$ (dB Scale).	51
Fig. 7.22. E_{total} when $\phi = 90^\circ$ (dB Scale).	52
Fig. 8.1. Near field measurement structure of different sizes.	54
Fig. 8.2. 10 by 10 x-directed probe array with 0.2λ separations in both directions.	57
Fig. 8.3. 10 by 10 x-directed probe array with 0.2λ separations in both directions (side view).	57
Fig. 8.4. E_{total} when $\phi = 0^\circ$ (dB Scale) for all sizes of the measurement planes from 0.8λ by 0.8λ to 20λ by 20λ with 0.2λ separations in both directions.	58
Fig. 8.5. E_{total} when $\phi = 90^\circ$ (dB Scale) for all sizes of the measurement planes from 0.8λ by 0.8λ to 20λ by 20λ with 0.2λ separations in both directions.	58
Fig. 8.6. Relative error at different sizes of measurement planes with 0.2λ separations in both directions ($\phi = 0^\circ$).	59

Fig. 8.7. Relative error at different sizes of measurement planes with 0.2λ separations in both directions ($\phi = 90^\circ$).....	60
Fig. 8.8. E_{total} when $\phi = 0^\circ$ (dB Scale) for all sizes of the measurement planes from 2λ by 2λ to 20λ by 20λ with 0.2λ separations in both directions.	61
Fig. 8.9. E_{total} when $\phi = 0^\circ$ (dB Scale) for all sizes of the measurement planes from 2λ by 2λ to 20λ by 20λ with 0.2λ separations in both directions.	61
Fig. 8.10. 50 by 50 x-directed probe array with 0.2λ separations in both directions. ...	63
Fig. 8.11. 50 by 50 x-directed probe array with 0.2λ separations in both directions (side view).	64
Fig. 8.12. E_{total} when $\phi = 0^\circ$ (dB Scale) for all sizes of the measurement planes from 0.8λ by 0.8λ to 20λ by 20λ with 0.2λ separations in both directions.	65
Fig. 8.13. E_{total} when $\phi = 90^\circ$ (dB Scale) for all sizes of the measurement planes from 0.8λ by 0.8λ to 20λ by 20λ with 0.2λ separations in both directions.	65
Fig. 8.14. Relative error at different sizes of measurement planes with 0.2λ , 0.4λ , 0.5λ separations in both directions ($\phi = 0^\circ$).....	66
Fig. 8.15. Relative error at different sizes of measurement planes with 0.2λ , 0.4λ , 0.5λ separations in both directions ($\phi = 90^\circ$).....	66
Fig. 8.16. E_{total} when $\phi = 0^\circ$ (dB Scale) for all sizes of the measurement planes from 10λ by 10λ to 20λ by 20λ with 0.2λ separations in both directions.	67
Fig. 8.17. E_{total} when $\phi = 90^\circ$ (dB Scale) for all sizes of the measurement planes from 10λ by 10λ to 20λ by 20λ with 0.2λ separations in both directions.	68
Fig. 8.18. E_{total} when $\phi = 0^\circ$ (dB Scale) for all sizes of the measurement planes from 10λ by 10λ to 20λ by 20λ with 0.4λ separations in both directions.	68

Fig. 8.19. Etot _{total} when $\phi = 90^\circ$ (dB Scale) for all sizes of the measurement planes from 10λ by 10λ to 20λ by 20λ with 0.4λ separations in both directions.	69
Fig. 8.20. Etot _{total} when $\phi = 0^\circ$ (dB Scale) for all sizes of the measurement planes from 10λ by 10λ to 20λ by 20λ with 0.5λ separations in both directions.	69
Fig. 8.21. Etot _{total} when $\phi = 90^\circ$ (dB Scale) for all sizes of the measurement planes from 10λ by 10λ to 20λ by 20λ with 0.5λ separations in both directions.	70
Fig. 8.22. A three-element Yagi-Uda antenna.	71
Fig. 8.23. Etot _{total} when $\phi = 0^\circ$ (dB Scale) for all sizes of the measurement planes from 0.8λ by 0.8λ to 20λ by 20λ with 0.2λ separations in both directions.	72
Fig. 8.24. Etot _{total} when $\phi = 90^\circ$ (dB Scale) for all sizes of the measurement planes from 0.8λ by 0.8λ to 20λ by 20λ with 0.2λ separations in both directions.	73
Fig. 8.25. Relative error at different sizes of measurement planes with 0.2λ separations in both directions ($\phi = 0^\circ$).	74
Fig. 8.26. Relative error at different sizes of measurement planes with 0.2λ separations in both directions ($\phi = 90^\circ$).	74
Fig. 8.27. 24 by 24 x-directed probe array with 0.2λ separations in both directions. ...	76
Fig. 8.28. 24 by 24 x-directed probe array with 0.2λ separations in both directions (side view).	77
Fig. 8.29. Etot _{total} when $\phi = 0^\circ$ (dB Scale) for all sizes of the measurement planes from 0.8λ by 0.8λ to 20λ by 20λ with 0.2λ separations in both directions.	78
Fig. 8.30. Etot _{total} when $\phi = 90^\circ$ (dB Scale) for all sizes of the measurement planes from 0.8λ by 0.8λ to 20λ by 20λ with 0.2λ separations in both directions.	78

Fig. 8.31. Relative error at different sizes of measurement planes with 0.2λ , 0.4λ , 0.5λ separations in both directions ($\phi = 0^\circ$).....	79
Fig. 8.32. Relative error at different sizes of measurement planes with 0.2λ , 0.4λ , 0.5λ separations in both directions ($\phi = 90^\circ$).....	79
Fig. 8.33. Etotal when $\phi = 0^\circ$ (dB Scale) for all sizes of the measurement planes from 5λ by 5λ to 20λ by 20λ with 0.2λ separations in both directions.	80
Fig. 8.34. Etotal when $\phi = 90^\circ$ (dB Scale) for all sizes of the measurement planes from 5λ by 5λ to 20λ by 20λ with 0.2λ separations in both directions.	81
Fig. 8.35. Etotal when $\phi = 0^\circ$ (dB Scale) for all sizes of the measurement planes from 4.8λ by 4.8λ to 20λ by 20λ with 0.4λ separations in both directions.	81
Fig. 8.36. Etotal when $\phi = 90^\circ$ (dB Scale) for all sizes of the measurement planes from 4.8λ by 4.8λ to 20λ by 20λ with 0.4λ separations in both directions.	82
Fig. 8.37. Etotal when $\phi = 0^\circ$ (dB Scale) for all sizes of the measurement planes from 5λ by 5λ to 20λ by 20λ with 0.5λ separations in both directions.	82
Fig. 8.38. Etotal when $\phi = 90^\circ$ (dB Scale) for all sizes of the measurement planes from 5λ by 5λ to 20λ by 20λ with 0.5λ separations in both directions.	83
Fig. 9.1. Planar scanning for x-z plane.	87
Fig. 9.2. Planar scanning for y-z plane.	88
Fig. 9.3. x-directed rectangular probe array (step1).....	90
Fig. 9.4. y-directed rectangular probe array (step1).....	91
Fig. 9.5. x-directed probe array (side view of step1).	91
Fig. 9.6. E total when $\phi=0$ (dB Scale) as in step1.....	92
Fig. 9.7. x-directed rectangular probe array (step2).....	93

Fig. 9.8. y-directed rectangular probe array (step2).....	94
Fig. 9.9. E total when $\phi=90$ (dB Scale) of step 2.....	95
Fig. 9.10. x-directed rectangular probe array (step1).....	97
Fig. 9.11. y-directed rectangular probe array (step1).....	97
Fig. 9.12. x-directed probe array (side view of step1).....	98
Fig. 9.13. E total when $\phi=0$ (dB Scale) of step1.....	99
Fig. 9.14. x-directed rectangular probe array (step2).....	100
Fig. 9.15. y-directed rectangular probe array (step2).....	100
Fig. 9.16. E total when $\phi=90$ (dB Scale) of step2.....	101
Fig. 9.17. A three-element Yagi-Uda antenna.	102
Fig. 9.18. E total when $\phi=0$ (dB Scale) of step1.....	103
Fig. 9.19. E total when $\phi=90$ (dB Scale) of step 2.....	104
Fig. 9.20. x-directed rectangular probe array (step1).....	107
Fig. 9.21. y-directed rectangular probe array (step1).....	107
Fig. 9.22. x-directed probe array (side view of step1).....	108
Fig. 9.23. E total when $\phi=0$ (dB Scale) of step 1.....	108
Fig. 9.24. x-directed rectangular probe array (step2).....	110
Fig. 9.25. y-directed rectangular probe array (step2).....	110
Fig. 9.26. E total when $\phi=90$ (dB Scale) of step 2.....	111
Fig. 10.1. Two planes measurement.	113
Fig. 10.2. x-directed probe array.....	116
Fig. 10.3. x-directed probe array(side view).....	117
Fig. 10.4. E_{total} when $\phi = 0^\circ$ (dB Scale).	118

Fig. 10.5. E_{total} when $\phi = 90^\circ$ (dB Scale).	118
Fig. 10.6. x-directed probe array.....	119
Fig. 10.7. x-directed probe array(side view).....	120
Fig. 10.8. E_{total} when $\phi = 0^\circ$ (dB Scale).	121
Fig. 10.9. E_{total} when $\phi = 90^\circ$ (dB Scale).	121
Fig. 10.10. A three-element Yagi-Uda antenna.	122
Fig. 10.11. E_{total} when $\phi = 0^\circ$ (dB Scale).	123
Fig. 10.12. E_{total} when $\phi = 90^\circ$ (dB Scale).	124
Fig. 10.13. x-directed probe array.....	125
Fig. 10.14. A x-directed probe array (side view).....	126
Fig. 10.15. E_{total} when $\phi = 0^\circ$ (dB Scale).	127
Fig. 10.16. E_{total} when $\phi = 90^\circ$ (dB Scale).	127

1 INTRODUCTION

The source reconstruction method (SRM) is a recent computational technique developed for antenna diagnostics and for carrying out near-field (NF) to far-field (FF) transformation [1]-[13]. The SRM is based on the application of the electromagnetic Equivalence Principle [17], in which one establishes an equivalent current distribution that radiates the same fields as the actual currents induced in the antenna under test (AUT). The knowledge of the equivalent currents allows the determination of the antenna radiating elements, as well as the prediction of the AUT-radiated fields outside the equivalent currents domain. The unique feature of the novel methodology has been illustrated that it has the potential to resolve equivalent currents that are smaller than half a wavelength in size, thus providing super-resolution. Furthermore, the measurement field samples can be taken at field spacing greater than half a wavelength, thus going beyond the classical sampling criteria. These two distinctive features are possible due to the incorporation of computational techniques into antenna measurement techniques thereby enhancing their accuracy and efficiency. In this methodology the unknowns are approximated by a continuous basis and, secondly, through the use of the analytic free space Green's function which is quite easy to compute numerically [17]-[20]. The latter condition also guarantees the inevitability of the electric field operator and provides a stable solution for the currents even when evanescent waves are present in the measurements. In addition, the use of the iterative conjugate gradient (CG) method in solving the ill-conditioned matrix equations can also be implemented [21]-[24]. Four different near field measurement approaches are presented to illustrate the accuracy and efficiency of the proposed methodology.

2 DEVELOPMENT OF THE PROPOSED

METHODOLOGY

The earliest near-field to far-field transformation methodologies are based on the model expansion method which use the measured near field data to calculate the coefficients of the wave functions [1]-[4]. The wave functions are expanded in terms of planar, cylindrical and spherical forms from the radiated fields of the antenna under test. The modeling and calculations are difficult to carry out sometimes. For the near-field antenna measurements, it started by using ideal probes scanning on arbitrary surfaces and ended up with arbitrary probes scanning on planar, cylindrical, and spherical surfaces [5]. The equivalent magnetic current approach is a widely used alternate method to calculate far field from near field data [6]-[13]. Based on the equivalent principle [17], this method uses the near-field data to determine an equivalent magnetic current source on a fictitious planar surface that encompasses the antenna under test, and under certain approximations, the magnetic currents will produce the same field as the antenna under test in the region of interest. In our work, the equivalent current approach of computing far fields from the near fields measured by different approaches. Using a single probe antenna measurement has been discussed without incorporating probe correction [6]. The introduction of a measurement probe appears to have minimal mutual effects between the AUT and the probe as shown in [7][8]. We further pointed out that the size of the measurement plane chosen to be close to or larger than the size of the actual source plane of the antenna under test, our NF-FF approach provides acceptable results [9]. Under some circumstance, two efficient approaches are proposed, the first one is measuring the near field over a sector and then

using that to obtain the far field pattern along principal planes with engineering accuracy [10] and the other one is that the accurate far field pattern can be obtained efficiently by using the amplitude only data of the square dipole array measurement [11].

3 PHILOSOPHY OF THE COMPUTATIONAL

METHODOLOGY

3.1 Brief Introduction of the Uniqueness Theorem and the Equivalence Principle

Uniqueness theorem and Equivalence Principle are important to solving complex problems, Equivalence Principle tells us what information is needed to obtain the solution and Uniqueness theorem makes sure that a solution is the only solution[17].

Uniqueness Theorem:

A field in some region is uniquely specified by the sources within the region plus any one of the following three:

- ① the tangential components of \vec{E} over the boundary
- ② the tangential components of \vec{H} over the boundary
- ③ the tangential components of \vec{E} over part of the boundary and the tangential components of \vec{H} over the rest of the boundary.

Equivalence Principle:

Let electromagnetics sources contained in a volume V bounded by surface S with outward normal \hat{n} to be the original problem as shown in Fig. 3.1. The fields \vec{E} and \vec{H} exterior to S can be found by removing sources in V and placing the following current densities on S :

$$\bar{J}_s = \hat{n} \times \bar{H}(s) \quad \text{on } S \quad (3-1)$$

$$\bar{M}_s = \bar{E}(s) \times \hat{n} \quad \text{on } S \quad (3-2)$$

where $\bar{H}(s)$ and $\bar{E}(s)$ are the fields produced by the original sources and evaluated at the surface S as shown in Fig. 3.2.

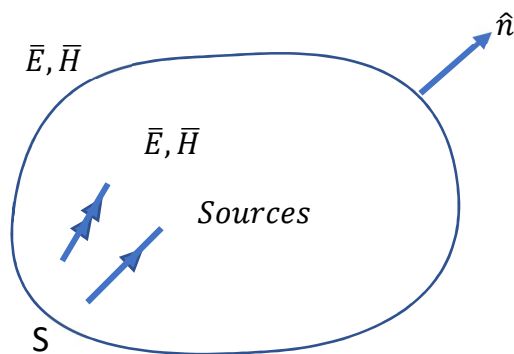


Fig. 3.1. Original problem.

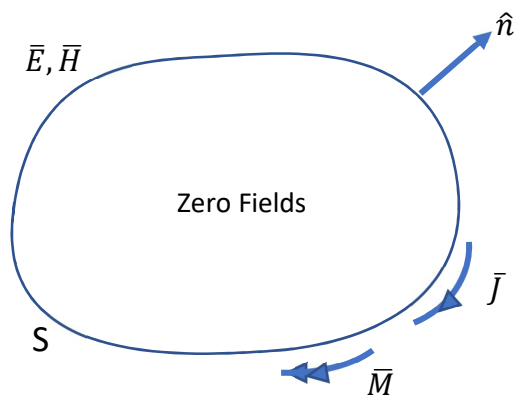


Fig. 3.2. The equivalent problem with both \bar{J} and \bar{M} produces the same field exterior to S as do the original sources.

In above, we used both the tangential components of \bar{E} and \bar{H} over the boundary, which gives us infinitely many equivalent currents as far as the external region is concerned.

According to Uniqueness Theorem, we can further simplify the equivalent problem that only the tangential components of \bar{E} as shown in Fig. 3.3 or tangential components of \bar{H} as shown in Fig. 3.4 are needed to determine the field. Our equivalent problems can be found in terms of only magnetic currents or only electric currents which makes the problems much easier to solve due to only one kind of equivalent current exist in the problem.

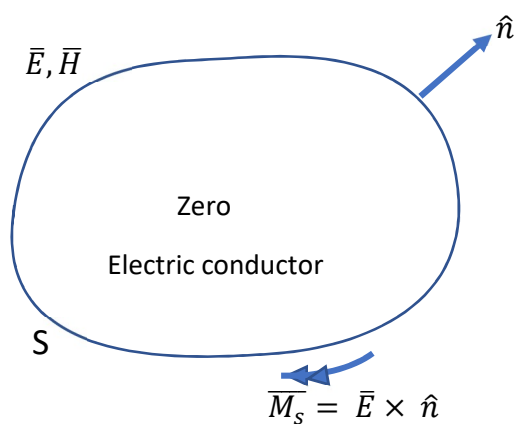


Fig. 3.3. Equivalent magnetic currents with an electric conductor.

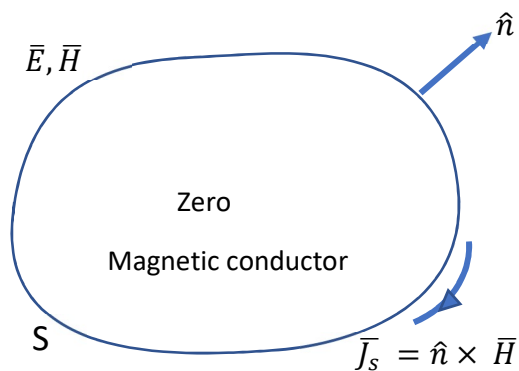


Fig. 3.4. Equivalent electric currents with a magnetic conductor.

3.2 Modeling of Antenna Measurement System

In our antenna measurement circumstances, we consider an arbitrary shaped antenna radiating into free space with the aperture of the antenna being a plane surface (assumed for simplicity but this assumption can be relaxed), which separates the total space into two: left-half (Region I) and right-half (Region II) spaces as shown in Fig. 3.5.

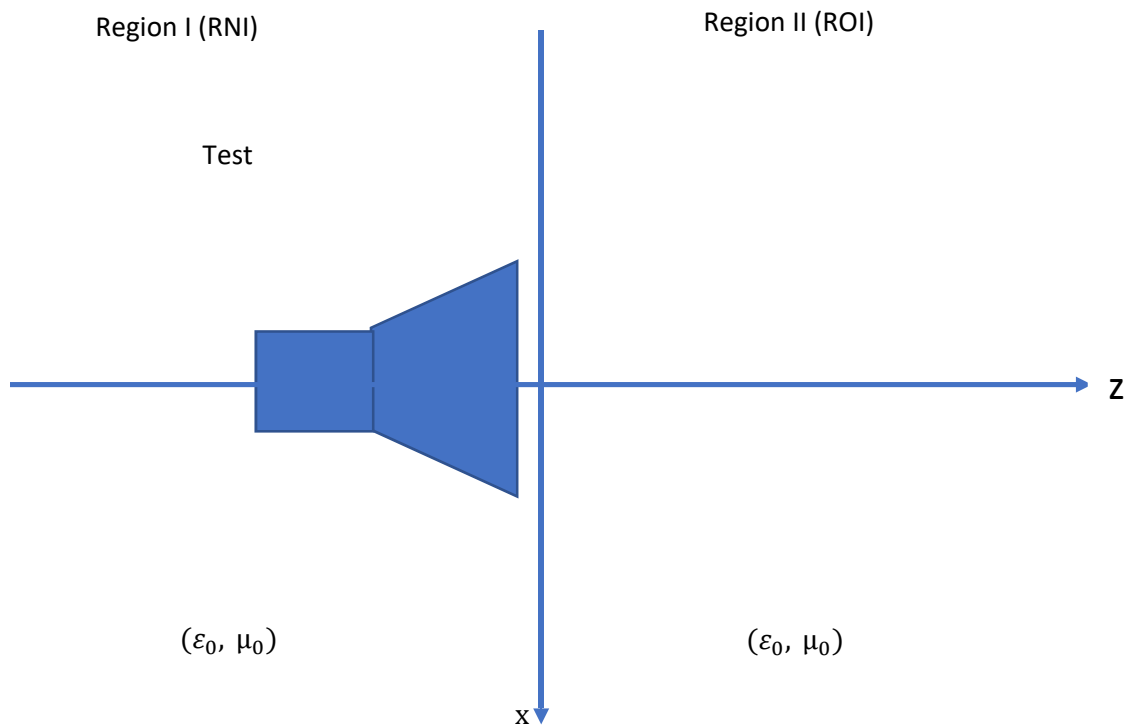


Fig. 3.5. Original Problem of antenna measurement.

For the antenna measurements purpose, we are interested in the radiation performance of the antenna, which means we are more interested in the Region II. Here we define Region I to be our Region of No Interest (RNI), and Region II to be our Region of Interest (ROI). By applying the Equivalence Principle, here we chose the equivalent magnetic approach [6]-[13] as shown above in Fig. 3.3. We postulate the electromagnetic fields in

the RNI to be zero and place a PEC (perfect electric conductor) on the x-y plane (as shown in Fig. 3.6). The PEC plane is supposed to be infinite extent can be thought of as closed at infinity.

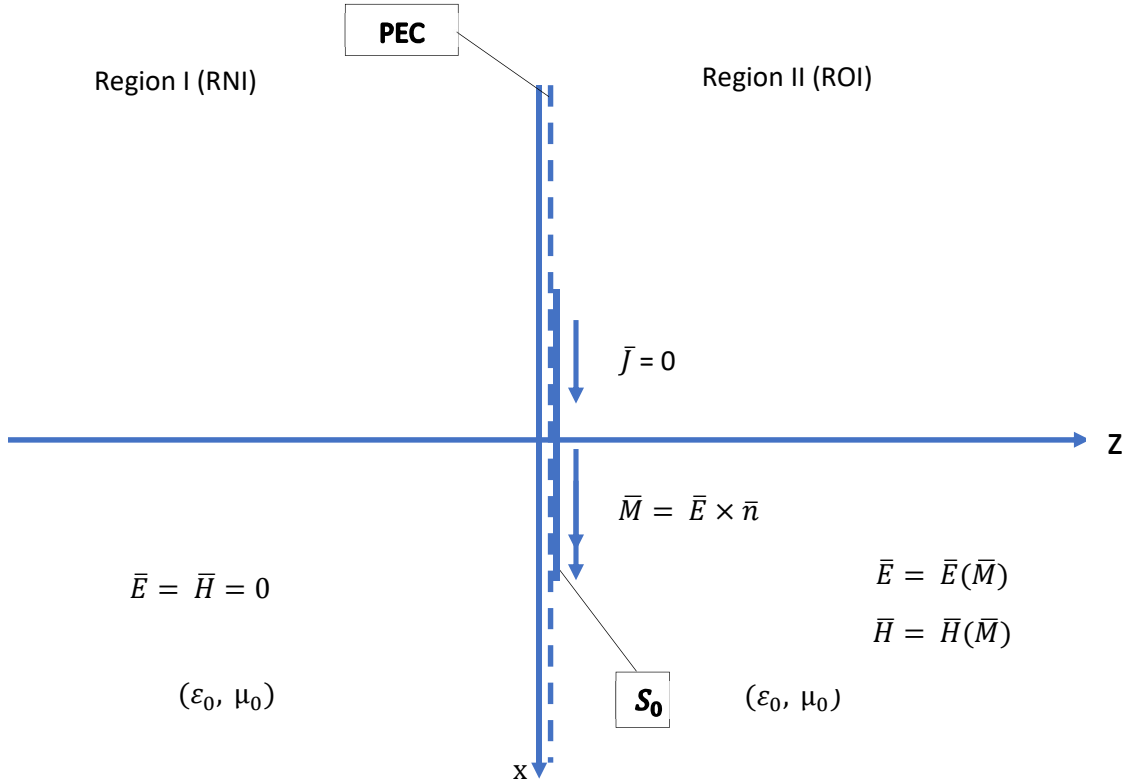


Fig. 3.6. Equivalent Problem.

We can further assume for the general case that the tangential component of the electrical field on the PEC is zero except over S_0 , and then \bar{M} exist only on S_0 as shown in Fig. 3.6. Then applying the image theory, the equivalent magnetic current \bar{M} is obtained as

$$\bar{M} = 2\bar{E} \times \hat{n} \text{ on } S_0 \quad (3-3)$$

where now \bar{M} radiates into free space. \bar{M} is determined from the measured electric field components. For computational purposes the measurement plane and hence the source plane has to be truncated to a finite region S_0 . The fields decay almost exponentially on this plane as we go away from the radiating aperture, thereby one can truncate the surface without introducing any significant error in this approximation.

Now, the far fields can easily be obtained from the measured electric near field via the equivalent magnetic current approach. Furthermore,

$$\bar{E}_{meas} = \bar{E}(\bar{M}) \quad (3-4)$$

where \bar{E}_{meas} is the measured electric near field, and \bar{M} is the equivalent magnetic current that exists on S_0 . After we find \bar{M} we can calculate the far field.

4 FORMULATION OF THE INTEGRAL EQUATIONS

4.1 Near-Field Measurement System

The near-field measurements are assumed to be performed over a planar surface which is parallel with the source plane as shown in Fig. 4.1.[6]-[13]

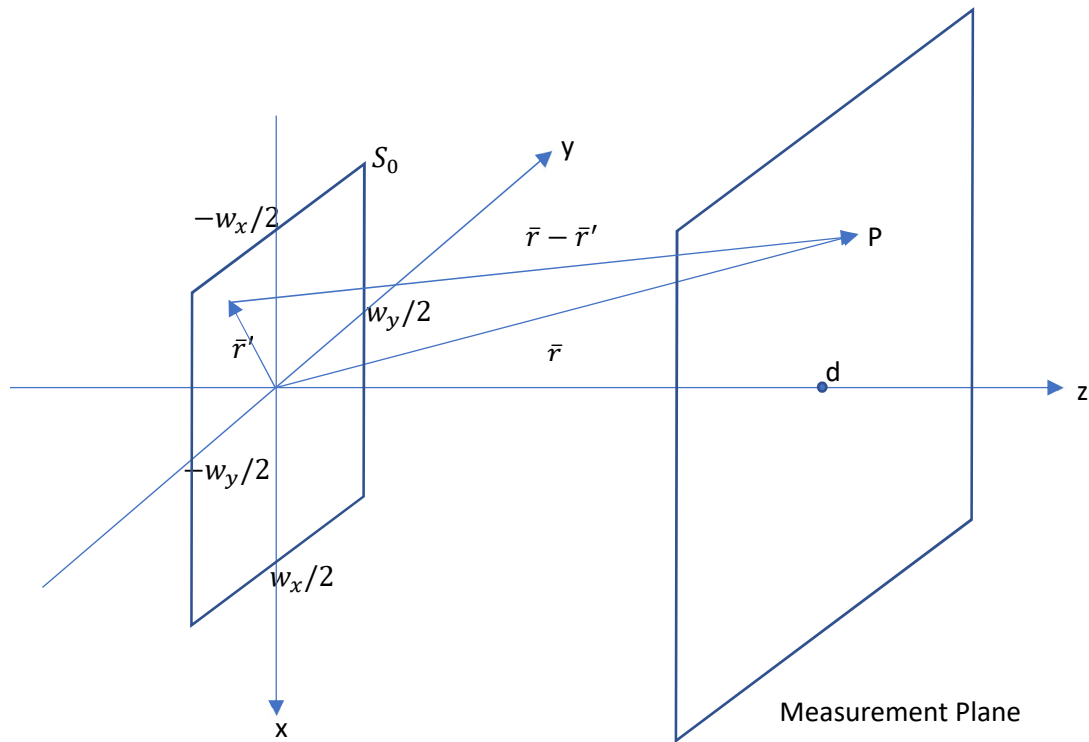


Fig. 4.1. Near-field measurement.

The source plane (S_0) is assumed to be a rectangular surface in the x-y plane with the dimensions w_x and w_y . The distance between the source plane and the measurement plane is d . The x and y components of the electric field of the points on the measurement plane are usually measured to calculate the equivalent magnetic current on the source plane.

4.2 Near-Field Formulations

The electric field at any point P can be found from

$$\bar{E}(\bar{r}) = - \iint_{S_0} [\bar{M}(\bar{r}') \times \nabla' g(\bar{r}, \bar{r}')] ds' \quad (4-1)$$

where $\bar{E}(\bar{r})$ is the electric field at an arbitrary located observation point \bar{r} , $\bar{M}(\bar{r}')$ is the equivalent magnetic current at the source point \bar{r}' , ∇' is the gradient operator according to the primed variables (sources), and $g(\bar{r}, \bar{r}')$ is the three-dimensional free space Green's function, and k_0 is the free space wave number.

$$g(\bar{r}, \bar{r}') = \frac{e^{-jk_0|\bar{r}-\bar{r}'|}}{4\pi|\bar{r}-\bar{r}'|} \quad (4-2)$$

Because \bar{M} is a 2-D current sheet,

$$\bar{M}(\bar{r}') = \hat{a}_x M_x + \hat{a}_y M_y \quad (4-3)$$

we can get

$$\bar{E}(\bar{r}) = - \iint_{S_0} [(\hat{a}_x M_x + \hat{a}_y M_y) \times \nabla' g(\bar{r}, \bar{r}')] ds' \quad (4-4)$$

where,

$$\nabla' g(\bar{r}, \bar{r}') = \hat{a}_x \frac{\partial g(\bar{r}, \bar{r}')}{\partial x'} + \hat{a}_y \frac{\partial g(\bar{r}, \bar{r}')}{\partial y'} + \hat{a}_z \frac{\partial g(\bar{r}, \bar{r}')}{\partial z'} \quad (4-5)$$

Substitute (4-5) into (4-4),

$$\bar{E}(\bar{r}) = - \iint_{S_0} \left\{ (\hat{a}_x M_x + \hat{a}_y M_y) \times \left[\hat{a}_x \frac{\partial g(\bar{r}, \bar{r}')}{\partial x'} + \hat{a}_y \frac{\partial g(\bar{r}, \bar{r}')}{\partial y'} + \hat{a}_z \frac{\partial g(\bar{r}, \bar{r}')}{\partial z'} \right] \right\} ds' \quad (4-6)$$

$$\bar{E}(\bar{r}) = - \iint_{S_0} \left\{ \hat{a}_z M_x \frac{\partial g(\bar{r}, \bar{r}')}{\partial y'} - \hat{a}_y M_x \frac{\partial g(\bar{r}, \bar{r}')}{\partial z'} - \hat{a}_z M_y \frac{\partial g(\bar{r}, \bar{r}')}{\partial x'} + \hat{a}_x M_y \frac{\partial g(\bar{r}, \bar{r}')}{\partial z'} \right\} ds' \quad (4-7)$$

Rearranging the components,

$$\bar{E}(\bar{r}) = - \iint_{S_0} \left\{ \hat{a}_x M_y \frac{\partial g(\bar{r}, \bar{r}')}{\partial z'} - \hat{a}_y M_x \frac{\partial g(\bar{r}, \bar{r}')}{\partial z'} + \hat{a}_z M_x \frac{\partial g(\bar{r}, \bar{r}')}{\partial y'} - \hat{a}_z M_y \frac{\partial g(\bar{r}, \bar{r}')}{\partial x'} \right\} ds' \quad (4-8)$$

$$\begin{aligned} \bar{E}(\bar{r}) = & -\hat{a}_x \iint_{S_0} \left\{ M_y \frac{\partial g(\bar{r}, \bar{r}')}{\partial z'} \right\} ds' + \hat{a}_y \iint_{S_0} \left\{ M_x \frac{\partial g(\bar{r}, \bar{r}')}{\partial z'} \right\} ds' - \hat{a}_z \iint_{S_0} \left\{ M_x \frac{\partial g(\bar{r}, \bar{r}')}{\partial y'} - \right. \\ & \left. M_y \frac{\partial g(\bar{r}, \bar{r}')}{\partial x'} \right\} ds' \end{aligned} \quad (4-9)$$

We can obtain the three components of the electric field as follows,

$$E_x = - \iint_{S_0} M_y \frac{\partial g(\bar{r}, \bar{r}')}{\partial z'} ds' \quad (4-10)$$

$$E_y = \iint_{S_0} M_x \frac{\partial g(\bar{r}, \bar{r}')}{\partial z'} ds' \quad (4-11)$$

$$E_z = - \iint_{S_0} \left\{ M_x \frac{\partial g(\bar{r}, \bar{r}')}{\partial y'} - M_y \frac{\partial g(\bar{r}, \bar{r}')}{\partial x'} \right\} ds' \quad (4-12)$$

where,

$$R = |\bar{r} - \bar{r}'| = \sqrt{(x - x')^2 + (y - y')^2 + (z - z')^2} \quad (4-13)$$

$$\frac{\partial g(\bar{r}, \bar{r}')}{\partial z'} = \frac{\partial}{\partial z'} \left(\frac{e^{-jk|\bar{r}-\bar{r}'|}}{4\pi|\bar{r}-\bar{r}'|} \right) = \frac{\partial}{\partial z'} \left(\frac{e^{-jkR}}{4\pi R} \right) \quad (4-14)$$

$$\frac{\partial g(\bar{r}, \bar{r}')}{\partial z'} = \frac{-jk \frac{\partial R}{\partial z'} e^{-jkR} R - e^{-jkR} \frac{\partial R}{\partial z'}}{4\pi R^2} = \frac{-jkR - 1}{4\pi R^2} \frac{\partial R}{\partial z'} e^{-jkR} \quad (4-15)$$

$$\frac{\partial R}{\partial z'} = \frac{-(z-z')}{\sqrt{(x-x')^2+(y-y')^2+(z-z')^2}} = \frac{-(z-z')}{R} \quad (4-16)$$

$$\frac{\partial g(\vec{r}, \vec{r}')}{\partial z'} = \frac{jkR+1}{4\pi R^2} \frac{(z-z')}{R} e^{-jkR} \quad (4-17)$$

Substitute(4-17) into (4-10) & (4-11),

$$E_x = - \iint M_y \frac{jkR+1}{4\pi R^2} \frac{z-z'}{R} e^{-jkR} ds' = - \iint M_y \frac{e^{-jkR}}{4\pi R^2} (jk + \frac{1}{R})(z - z') ds' \quad (4-18)$$

$$E_y = \iint M_x \frac{jkR+1}{4\pi R^2} \frac{z-z'}{R} e^{-jkR} ds' = \iint M_x \frac{e^{-jkR}}{4\pi R^2} (jk + \frac{1}{R})(z - z') ds' \quad (4-19)$$

Similarly,

$$E_z = - \iint \left\{ M_x \frac{\partial g(\vec{r}, \vec{r}')}{\partial y'} - M_y \frac{\partial g(\vec{r}, \vec{r}')}{\partial x'} \right\} ds' = - \iint \left\{ M_x \frac{jkR+1}{4\pi R^2} \frac{(y-y')}{R} e^{-jkR} - M_y \frac{jkR+1}{4\pi R^2} \frac{(x-x')}{R} e^{-jkR} \right\} ds' \quad (4-20)$$

Equation (4-18) and (4-19) show that the integral equation is a decoupled one with respect to the two components of the magnetic currents. So, the following two integral equations can be solved separately.

$$E_x = -GM_y \quad (4-21)$$

$$E_y = GM_x \quad (4-22)$$

where,

$$G = \iint_{S_0} \frac{e^{-jkR}}{4\pi R^2} (jk + \frac{1}{R})(z - z') ds' \quad (4-23)$$

We can obtain the equivalent magnetic current M_x and M_y on the source plane by using the x and y components of the measured electric near fields $E_{meas,x}(\vec{r})$ and $E_{meas,y}(\vec{r})$.

4.3 Far-Field Formulations

After we obtained the M_x and M_y on the source plane, we want to calculate the far field radiated by the equivalent magnetic currents on the source plane[14][15] as shown in Fig. 4.2.

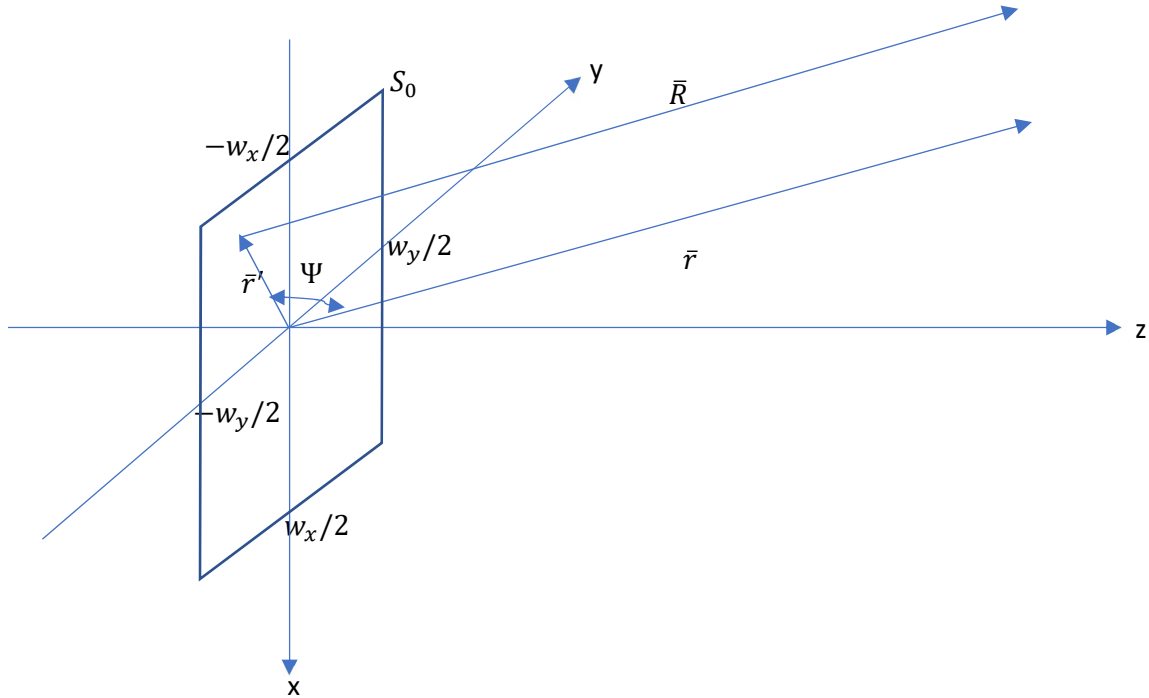


Fig. 4.2. Far-field system.

For far-field observations R can most commonly be approximated by

$$R \cong r - r' \cos \Psi \quad (4-24)$$

where Ψ is the angle between the vectors \bar{r} and \bar{r}' . Geometrically the approximation of (4-24) assumes that the vectors \bar{R} and \bar{r} are parallel.

In our case, the potential function \bar{A} generated by electric current \bar{J} is zero, because \bar{J} is zero, and the potential function \bar{F} generated by the magnetic currents \bar{M} can be written as

$$\bar{F} = \frac{\epsilon}{4\pi} \iint_{S_0} \bar{M}_s \frac{e^{-jkR}}{R} ds' \quad (4-25)$$

Substitute (4-24) into (4-25),

$$\bar{F} \cong \frac{\epsilon}{4\pi} \iint_{S_0} \bar{M}_s \frac{e^{-jk(r-r'\cos\Psi)}}{r} ds' \quad (4-26)$$

$$\bar{F} = \frac{\epsilon e^{-jkr}}{4\pi r} \iint_{S_0} \bar{M}_s e^{jkr'\cos\Psi} ds' \quad (4-27)$$

$$\bar{F} = \frac{\epsilon e^{-jkr}}{4\pi r} \bar{L} \quad (4-28)$$

where

$$\bar{L} = \iint_{S_0} \bar{M}_s e^{jkr'\cos\Psi} ds' \quad (4-29)$$

In the far-field only the θ and φ components of the fields are dominant, we have

$$\bar{H}_F \cong -j\omega\bar{F} \quad (4-30)$$

$$\bar{E}_F = -\eta\hat{a}_r \times \bar{H}_F = j\omega\eta\hat{a}_r \times \bar{F} \quad (4-31)$$

From (4-30) and (4-31) we can obtain all components of the fields in the spherical coordinate due to the equivalent magnetic currents,

$$H_r \cong 0 \quad (4-32)$$

$$H_\theta \cong -j\omega F_\theta \quad (4-33)$$

$$H_\varphi \cong -j\omega F_\varphi \quad (4-34)$$

$$E_r \cong 0 \quad (4-35)$$

$$E_\theta \cong -j\omega\eta F_\varphi \quad (4-36)$$

$$E_\varphi \cong +j\omega\eta F_\theta \quad (4-37)$$

Combine (4-28), (4-29) with (4-32) to (4-37), all components of the fields can be written as

$$H_r \cong 0 \quad (4-38)$$

$$H_\theta \cong -\frac{jke^{-jkr}}{4\pi r} \frac{L_\theta}{\eta} \quad (4-39)$$

$$H_\varphi \cong -\frac{jke^{-jkr}}{4\pi r} \frac{L_\varphi}{\eta} \quad (4-40)$$

$$E_r \cong 0 \quad (4-41)$$

$$E_\theta \cong -\frac{jke^{-j}}{4\pi r} L_\varphi \quad (4-42)$$

$$E_\varphi \cong +\frac{jke^{-jkr}}{4\pi r} L_\theta \quad (4-43)$$

where L_θ and L_φ by applying the rectangular-to-spherical component transformation (4-44) on (4-29),

$$\begin{pmatrix} \hat{a}_x \\ \hat{a}_y \\ \hat{a}_z \end{pmatrix} = \begin{pmatrix} \sin\theta\cos\varphi & \cos\theta\cos\varphi & -\sin\varphi \\ \sin\theta\sin\varphi & \cos\theta\sin\varphi & \cos\varphi \\ \cos\theta & -\sin\theta & 0 \end{pmatrix} \times \begin{pmatrix} \hat{a}_r \\ \hat{a}_\theta \\ \hat{a}_\varphi \end{pmatrix} \quad (4-44)$$

which is,

$$\bar{L} = \iint_{S_0} \bar{M}_s e^{jkr'\cos\Psi} ds' = \iint_{S_0} (\hat{a}_x M_x + \hat{a}_y M_y) e^{jkr'\cos\Psi} ds' \quad (4-45)$$

Then we have,

$$\bar{L} = \iint_{S_0} [(\hat{a}_r \sin\theta \cos\varphi + \hat{a}_\theta \cos\theta \cos\varphi - \hat{a}_\varphi \sin\varphi)M_x + (\hat{a}_r \sin\theta \sin\varphi + \hat{a}_\theta \cos\theta \sin\varphi + \hat{a}_\varphi \cos\varphi)M_y] e^{jkr' \cos\Psi} ds' \quad (4-46)$$

$$\bar{L} = \iint_{S_0} [\hat{a}_r (\sin\theta \cos\varphi M_x + \sin\theta \sin\varphi M_y) + \hat{a}_\theta (\cos\theta \cos\varphi M_x + \cos\theta \sin\varphi M_y) + \hat{a}_\varphi (-\sin\varphi M_x + \cos\varphi M_y)] e^{jkr' \cos\Psi} ds' \quad (4-47)$$

finally, we obtain L_θ and L_φ as

$$L_\theta = \iint_{S_0} [\cos\theta \cos\varphi M_x + \cos\theta \sin\varphi M_y] e^{jk' \cos} ds' \quad (4-48)$$

$$L_\varphi = \iint_{S_0} [-\sin\varphi M_x + \cos\varphi M_y] e^{jk' \cos} ds' \quad (4-49)$$

also,

$$ds' = dx' dy' \quad (4-50)$$

and,

$$\cos\Psi = \bar{r}' \cdot \hat{a}_r = (\hat{a}_x x' + \hat{a}_y y') \cdot (\hat{a}_x \sin\theta \cos\varphi + \hat{a}_y \sin\theta \sin\varphi + \hat{a}_z \cos\theta) \quad (4-51)$$

$$\cos\Psi = x' \sin\theta \cos\varphi + y' \sin\theta \sin\varphi \quad (4-52)$$

every component in the calculation of E_θ and E_φ is in terms of θ and φ , which means the far-field $E_\theta(\theta, \varphi)$ and $E_\varphi(\theta, \varphi)$ can be obtained from the equivalent magnetic current \bar{M}_s as shown above.

5 FORMULATION OF MATRIX EQUATIONS FROM THE INTEGRAL EQUATIONS

The concept of near-field to far-field transformation is first to measure E_x and E_y in the near-field, and then solve for M_x and M_y on the equivalent plane and calculate the radiated far-field E_θ and E_ϕ accordingly. The question left is how to solve for M_x and M_y from the integral equations we derived above in (4-21) and (4-22)

$$E_x = -GM_y \quad (5-1)$$

$$E_y = GM_x \quad (5-2)$$

where,

$$G = \iint_{S_0} \frac{e^{-j}}{4\pi R^2} (jk + \frac{1}{R})(z - z') ds' \quad (5-3)$$

Here we use Method of Moment (MOM)[18]-[20] procedure to transform the E-field integral equations (5-1) and (5-2) into matrix equations, so that they can be numerically calculated using the computer.

5.1 Discrete Formulation of the Source Plane

First, for the above description, the source plane (S_0) is assumed to be a rectangular one in the x - y plane with extensions $-w_x/2 \leq x' \leq w_x/2$ and $-w_y/2 \leq y' \leq w_y/2$ as shown in Fig. 5.1.

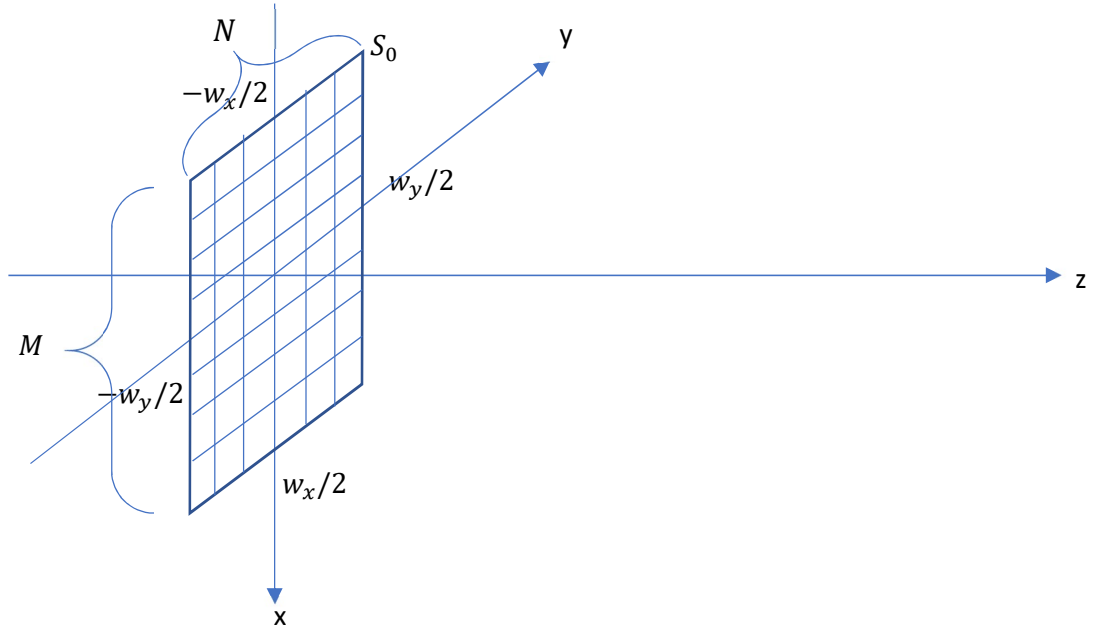


Fig. 5.1. Discretization of the source plane.

The source plane is divided into $M \cdot N$ equally spaced rectangular patches with dimensions $\Delta x'$ and $\Delta y'$

$$\Delta x' = w_x/M \quad (5-4)$$

$$\Delta y' = w_y/N \quad (5-5)$$

The center of the i, j^{th} patch x_i' and y_i' are given by

$$x_i' = -\frac{w_x}{2} + \frac{\Delta x'}{2} + i\Delta x' \quad (5-6)$$

$$y_i' = -\frac{w_y}{2} - \frac{\Delta y'}{2} + j\Delta y' \quad (5-7)$$

Then, a point matching procedure at the center of each patch is chosen, both M_x and M_y are approximated by equally spaced two-dimensional pulse basis functions

$$M_x(x', y') = \sum_{i=1}^M \sum_{j=1}^N \alpha_{ij} \Pi_{ij}(x', y') \quad (5-8)$$

$$M_y(x', y') = \sum_{i=1}^M \sum_{j=1}^N \beta_{ij} \Pi_{ij}(x', y') \quad (5-9)$$

where α_{ij} and β_{ij} are the unknown amplitudes of the x and y directed magnetic currents, respectively on the i, j^{th} patch, and $\Pi_{ij}(x', y')$ is the two-dimensional pulse basis function of the i, j^{th} patch and defined as

$$\Pi_{ij}(x', y') = \begin{cases} 1 & \text{if } x_i' - \frac{\Delta x'}{2} \leq x' \leq x_i' + \frac{\Delta x'}{2} \\ & y_i' - \frac{\Delta y'}{2} \leq y' \leq y_i' + \frac{\Delta y'}{2} \\ 0 & \text{otherwise} \end{cases} \quad (5-10)$$

5.2 Discrete Formulation of the Measurement Plane

The measurement plane is assumed to be a rectangular one in the x-y plane with extensions $-l_x/2 \leq x \leq l_x/2$ and $-l_y/2 \leq y \leq l_y/2$ as shown in Fig. 5.2.

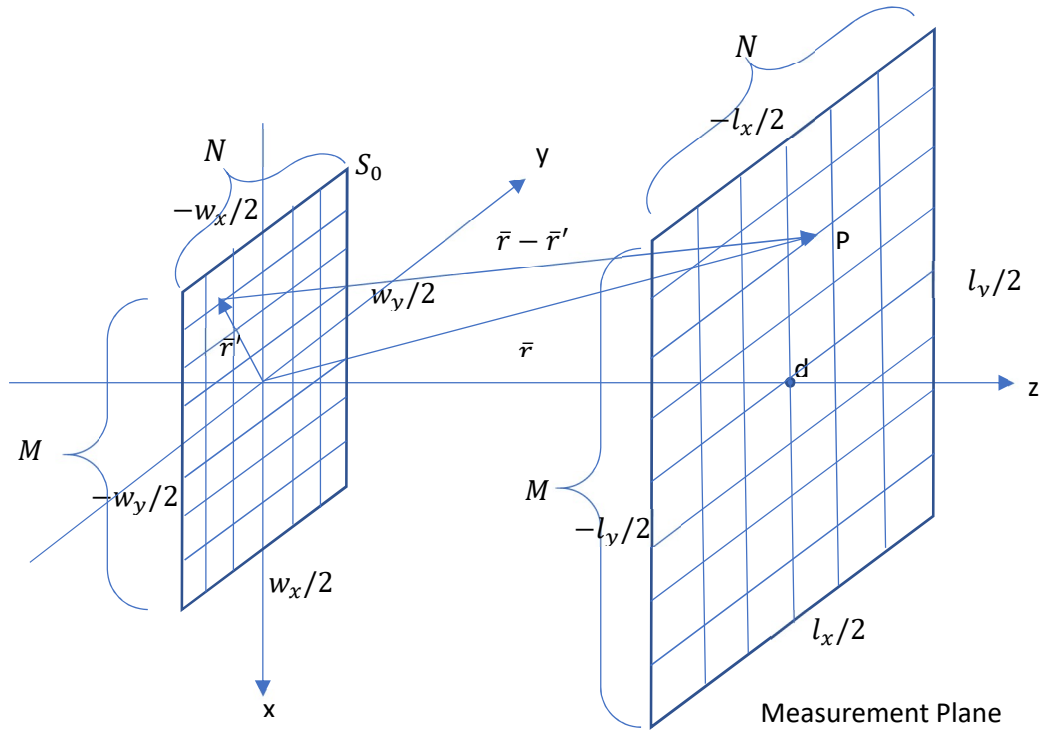


Fig. 5.2. Discretization of both source plane and measurement plane.

It is also assumed that the measured electric near-fields are known at discrete points on the measurement plane, which is also divided into $M \cdot N$ equally spaced rectangular patches with dimensions Δx and Δy ,

$$\Delta x = l_x/M \quad (5-11)$$

$$\Delta y = l_y/N \quad (5-12)$$

The center of the i, j^{th} patch x_i and y_i are given by

$$x_i = -\frac{l_x}{2} - \frac{\Delta x}{2} + i\Delta x \quad (5-13)$$

$$y_i = -\frac{l_y}{2} - \frac{\Delta y}{2} + j\Delta y \quad (5-14)$$

Then, a point matching procedure at the center of each patch is chosen, both E_x and E_y are approximated by equally spaced two-dimensional pulse basis functions

$$E_x(x, y) = \sum_{i=1}^M \sum_{j=1}^N \gamma_{ij} \Pi_{ij}(x, y) \quad (5-15)$$

$$E_y(x, y) = \sum_{i=1}^M \sum_{j=1}^N \delta_{ij} \Pi_{ij}(x, y) \quad (5-16)$$

where γ_{ij} and δ_{ij} are the measured x and y directed electric fields, respectively on the i, j^{th} patch, and $\Pi_{ij}(x, y)$ is the two-dimensional pulse basis function of the i, j^{th} patch and defined as

$$\Pi_{ij}(x, y) = \begin{cases} 1 & \text{if } x_i - \frac{\Delta x}{2} \leq x \leq x_i + \frac{\Delta x}{2} \\ & y_i - \frac{\Delta y}{2} \leq y \leq y_i + \frac{\Delta y}{2} \\ 0 & \text{otherwise} \end{cases} \quad (5-17)$$

5.3 Discrete Formulation of the Integral Equations

Substituting (5-8), (5-9) and (5-15), (5-16) into (5-1), (5-2) and utilizing point matching procedure, the following two decoupled matrix equations are obtained,

$$\begin{pmatrix} E_{meas,x}(1,1) \\ E_{meas,x}(1,2) \\ \vdots \\ E_{meas,x}(1,N) \\ E_{meas,x}(2,1) \\ E_{meas,x}(2,2) \\ \vdots \\ E_{meas,x}(2,N) \\ \vdots \\ \vdots \\ E_{meas,x}(M,N) \end{pmatrix} = -G \times \begin{pmatrix} M_y(1,1) \\ M_y(1,2) \\ \vdots \\ M_y(1,N) \\ M_y(2,1) \\ M_y(2,2) \\ \vdots \\ M_y(2,N) \\ \vdots \\ \vdots \\ M_y(M,N) \end{pmatrix} \quad (5-18)$$

$$\begin{pmatrix} E_{meas,y}(1,1) \\ E_{meas,y}(1,2) \\ \vdots \\ E_{meas,y}(1,N) \\ E_{meas,y}(2,1) \\ E_{meas,y}(2,2) \\ \vdots \\ E_{meas,y}(2,N) \\ \vdots \\ \vdots \\ E_{meas,y}(M,N) \end{pmatrix} = G \times \begin{pmatrix} M_x(1,1) \\ M_x(1,2) \\ \vdots \\ M_x(1,N) \\ M_x(2,1) \\ M_x(2,2) \\ \vdots \\ M_x(2,N) \\ \vdots \\ \vdots \\ M_x(M,N) \end{pmatrix} \quad (5-19)$$

where $E_{meas,x}$, $E_{meas,y}$, M_x and M_y are all $M \cdot N$ by 1 matrix. G is the moment matrix for the planar scanning case, the explicit expressions for G is given by

$$G_{k,l} = \iint_{\Omega_l} \frac{e^{-jk_0 R}}{4\pi R^2} (z_k - z') \left[jk_0 + \frac{1}{R} \right] ds' \quad (5-20)$$

where Ω_l is the area of the l^{th} patch, and R is the distance between the k^{th} field point (\vec{r}_k) and l^{th} source point (\vec{r}_l'), $ds' = dx' \cdot dy'$. There are $M \cdot N$ patches on the source plane and

$M \cdot N$ patches on the measurement plane, which makes the G matrix to be a $M \cdot N$ by $M \cdot N$ matrix as follows,

$$\begin{pmatrix} G(1_1,1_1) & G(1_1,1_2) & \cdots & G(1_1,1_N) & G(1_1,2_1) & \cdots & G(1_1,2_N) & \cdots & G(1_1,M_N) \\ G(1_2,1_1) & G(1_2,1_2) & \cdots & G(1_2,1_N) & G(1_2,2_1) & \cdots & G(1_2,2_N) & \cdots & G(1_2,M_N) \\ \vdots & \vdots & \vdots & \vdots & \vdots & \vdots & \vdots & \vdots & \vdots \\ G(1_N,1_1) & G(1_N,1_2) & \cdots & G(1_N,1_N) & G(1_N,2_1) & \cdots & G(1_N,2_N) & \cdots & G(1_N,M_N) \\ G(2_1,1_1) & G(2_1,1_2) & \cdots & G(2_1,1_N) & G(2_1,2_1) & \cdots & G(2_1,2_N) & \cdots & G(2_1,M_N) \\ \vdots & \vdots & \vdots & \vdots & \vdots & \vdots & \vdots & \vdots & \vdots \\ G(2_N,1_1) & G(2_N,1_2) & \cdots & G(2_N,1_N) & G(2_N,2_1) & \cdots & G(2_N,2_N) & \cdots & G(2_N,M_N) \\ \vdots & \vdots & \vdots & \vdots & \vdots & \vdots & \vdots & \vdots & \vdots \\ G(M_N,1_1) & G(M_N,1_2) & \cdots & G(M_N,1_N) & G(M_N,2_1) & \cdots & G(M_N,2_N) & \cdots & G(M_N,M_N) \end{pmatrix} \quad (5-21)$$

where $G(1_1,1_1)$ represent the G expression between the $1,1^{th}$ patch on the source plane and the $1,1^{th}$ patch on the measurement plane, $G(1_1,1_2)$ represent the G expression between the $1,1^{th}$ patch on the source plane and the $1,2^{th}$ patch on the measurement plane, etc.

6 SOLUTION FOR THE MATRIX EQUATIONS

6.1 Method Choosing

The remaining problem is how to solve equation (5-18) and (5-19) to calculate M_x and M_y from $E_{meas,x}$, $E_{meas,y}$. They are both result in the same type of problem as follows,

$$AX = Y \quad (6-1)$$

where A is the coefficient matrix G, X is the column matrix of the unknowns to be determined, and Y is the column matrix of the measured fields. To solve this type of equation, there are many methods to choose from [18]-[26]. For example, direct methods, including Cramer's rule, LU-Decomposition and Gaussian Elimination, which are good options when the sizes of the matrices are small. For systems with the large matrices, the round-off errors and truncation errors build up in direct methods and the elimination procedures become very time consuming. To reduce the effect of round-off error, iterative methods are good alternatives to rectify this problem. There are many kinds of iterative methods. Linear iterative methods include Gauss' Method, Jacobi's Method, Seidel's Method, Back and Forth Seidel Method, SOR Techniques, etc. Non-linear iterative methods include Steepest Descent Method and Conjugate Gradient Method (CGM). The advantage of Non-linear iterative methods over linear iterative ones is faster convergence making non-linear iterative methods very useful when the sizes of the matrices are large. Hence, we choose to use a Non-linear iterative method to solve these matrix equations. Specifically we choose the Conjugate Gradient Methods because a Fourier Transform may be utilized to evaluate some terms further accelerating the speed of calculation.

6.2 Procedures of Conjugate Gradient Method

The Conjugate Gradient Method[20]-[24] starts with an initial guess X_1 and computes

$$R_1 = Y_1 - AX_1 \quad (6-2)$$

$$P_1 = A^*R_1 \quad (6-3)$$

For $i = 1, 2, \dots$ let

$$a_i = \frac{\|A^*R_i\|^2}{\|AP_i\|^2} \quad (6-4)$$

$$X_{i+1} = X_i + a_iP_i \quad (6-5)$$

$$R_{i+1} = R_i - a_iAP_i \quad (6-6)$$

$$b_i = \frac{\|A^*R_{i+1}\|^2}{\|A^*R_i\|^2} \quad (6-7)$$

$$P_{i+1} = A^*R_{i+1} + b_iP_i \quad (6-8)$$

where A^* is the conjugate transpose of A .

Most of the computational cost in CGM occurs in the calculation of AP_i and A^*R_{i+1} . These two calculations have to be performed inside a loop which needs to be carried out many times. This is the most time-consuming part if we multiply them directly.

6.3 Brief Introduction of Toeplitz Matrix

Any n by n matrix of the form

$$A = \begin{pmatrix} a_0 & a_{-1} & a_{-2} & \cdots & \cdots & a_{-(n-1)} \\ a_1 & a_0 & a_{-1} & \ddots & & \vdots \\ a_2 & a_1 & \ddots & \ddots & \ddots & \vdots \\ \vdots & \ddots & \ddots & \ddots & a_{-1} & a_{-2} \\ \vdots & & \ddots & a_1 & a_0 & a_{-1} \\ a_{n-1} & \cdots & \cdots & a_2 & a_1 & a_0 \end{pmatrix} \quad (6-9)$$

is a Toeplitz Matrix[21]. If the i, j^{th} element of A is denoted $A_{i,j}$, then we have

$$A_{i,j} = A_{i+1,j+1} = a_{i-j} \quad (6-10)$$

Here we use a third order Toeplitz matrix as an example to show how to use FFT algorithm to accelerate the calculation.

$$\begin{pmatrix} a_0 & a_{-1} & a_{-2} \\ a_1 & a_0 & a_{-1} \\ a_2 & a_1 & a_0 \end{pmatrix} \times \begin{pmatrix} x_0 \\ x_1 \\ x_2 \end{pmatrix} = \begin{pmatrix} y_0 \\ y_1 \\ y_2 \end{pmatrix} = \begin{pmatrix} a_0x_0 + a_{-1}x_1 + a_{-2}x_2 \\ a_1x_0 + a_0x_1 + a_{-1}x_2 \\ a_2x_0 + a_1x_1 + a_0x_2 \end{pmatrix} \quad (6-11)$$

in the equation (6-11), we obtained the result from the direct multiplication, also we can take the convolutional variation A^c of the original matrix A and take convolutional variation X^c of the original vectors X as follows,

$$A^c = \{a_{-2} \quad a_{-1} \quad a_0 \quad a_1 \quad a_2\} \quad (6-12)$$

$$X^c = \{x_0 \quad x_1 \quad x_2 \quad 0 \quad 0\} \quad (6-13)$$

By taking the convolution of A^c and X^c , we can find that the direct multiplication result of the original matrix A and the original vectors X which yields $y_0 \ y_1 \ y_2$, obtained in the convolution result,

$$A^c * X^c = \{a_{-2}x_0 \ a_{-2}x_1 + a_{-1}x_0 \ y_0 \ y_1 \ y_2 \ a_1x_2 + a_2x_1 \ a_2x_2\} \quad (6-14)$$

here, we use the question mark to represent the elements which we are not interested and θ represent a truncation operator which selects the elements we are interested in.

$$A^c * X^c = \{? \ y_0 \ y_1 \ y_2 \ ?\} \quad (6-15)$$

$$A^c * X^c = \theta\{? \ y_0 \ y_1 \ y_2 \ ?\} = \theta\{Y\} = \{y_0 \ y_1 \ y_2\} \quad (6-16)$$

According to the convolution theorem, the Fourier transform of a convolution of two signals is the pointwise product of their Fourier transforms, which means

$$A^c * X^c = F^{-1}\{F(A^c)F(X^c)\} \quad (6-17)$$

where F denotes the discrete Fourier Transform, F^{-1} denotes the inverse discrete Fourier Transform. Hence, we can use FFT to accelerate the calculation if the matrix has the Toeplitz structure.

6.4 Block Toeplitz Matrix

Back to our original problem, we want to accelerate the calculation of GP_i and G^*R_{i+1} which occurs in every iteration. These calculations can be very efficiently carried out under some specific conditions. If the dimension and discretization of the source plane and the measurement plane are chosen to be the same, the resultant G matrix is Block Toeplitz matrix. The structure of the matrix can be exploited by noting that a Fourier Transform may be utilized to evaluate the terms in the following CGM, which is called Conjugate Gradient Method and Fast Fourier Transform (CGFFT)[21]-[23].

Our G matrix is a function of R which is the distance between the k^{th} field point (\bar{r}_k) and l^{th} source point (\bar{r}_l'). Here we choose a very basic and simple case to illustrate the problem as shown in Fig. 6.1.

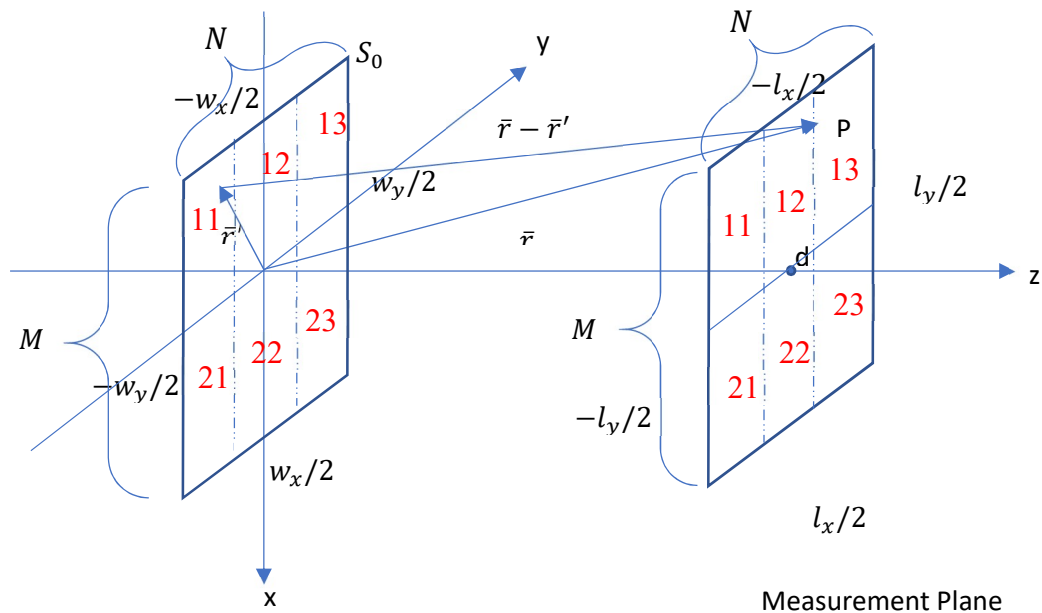


Fig. 6.1. Example of Block Toeplitz Matrix.

We make $l_x = w_x$ and $l_y = w_y$, $M = 2$ and $N = 3$ for both source plane and measurement plane, which means the dimension and discretization of the source plane and the measurement plane are chosen to be the same.

The G Matrix generated in this example is

$$\begin{pmatrix} G(1_1,1_1) & G(1_1,1_2) & G(1_1,1_3) & G(1_1,2_1) & G(1_1,2_2) & G(1_1,2_3) \\ G(1_2,1_1) & G(1_2,1_2) & G(1_2,1_3) & G(1_2,2_1) & G(1_2,2_2) & G(1_2,2_3) \\ G(1_3,1_1) & G(1_3,1_2) & G(1_3,1_3) & G(1_3,2_1) & G(1_3,2_2) & G(1_3,2_3) \\ G(2_1,1_1) & G(2_1,1_2) & G(2_1,1_3) & G(2_1,2_1) & G(2_1,2_2) & G(2_1,2_3) \\ G(2_2,1_1) & G(2_2,1_2) & G(2_2,1_3) & G(2_2,2_1) & G(2_2,2_2) & G(2_2,2_3) \\ G(2_3,1_1) & G(2_3,1_2) & G(2_3,1_3) & G(2_3,2_1) & G(2_3,2_2) & G(2_3,2_3) \end{pmatrix} \quad (6-18)$$

we can easily find that

$$G(1_1,1_2) = G(1_2,1_3) \neq G(1_3,2_1) \neq G(2_1,2_2) = G(2_2,2_3) \quad (6-19)$$

which indicates that G matrix is not a Toeplitz matrix, but it there's still some special structure of this matrix, we can treat this $M \cdot N$ by $M \cdot N$ matrix as a M by M matrix and each element in this matrix is a N by N matrix.

In this example is G is a 2 by 2 Matrix with 4 elements A, B, C, D

$$G = \begin{pmatrix} A & B \\ C & D \end{pmatrix} \quad (6-20)$$

where

$$A = \begin{pmatrix} G(1_1,1_1) & G(1_1,1_2) & G(1_1,1_3) \\ G(1_2,1_1) & G(1_2,1_2) & G(1_2,1_3) \\ G(1_3,1_1) & G(1_3,1_2) & G(1_3,1_3) \end{pmatrix} \quad (6-21)$$

$$B = \begin{pmatrix} G(1_1,2_1) & G(1_1,2_2) & G(1_1,2_3) \\ G(1_2,2_1) & G(1_2,2_2) & G(1_2,2_3) \\ G(1_3,2_1) & G(1_3,2_2) & G(1_3,2_3) \end{pmatrix} \quad (6-22)$$

$$C = \begin{pmatrix} G(2_1,1_1) & G(2_1,1_2) & G(2_1,1_3) \\ G(2_2,1_1) & G(2_2,1_2) & G(2_2,1_3) \\ G(2_3,1_1) & G(2_3,1_2) & G(2_3,1_3) \end{pmatrix} \quad (6-23)$$

$$D = \begin{pmatrix} G(2_1,2_1) & G(2_1,2_2) & G(2_1,2_3) \\ G(2_2,2_1) & G(2_2,2_2) & G(2_2,2_3) \\ G(2_3,2_1) & G(2_3,2_2) & G(2_3,2_3) \end{pmatrix} \quad (6-24)$$

$A = D$, if we treat the N by N matrices A , B , C , D as the elements in the G matrix, G does have the Toeplitz structure, and every single element A , B , C , D does have the Toeplitz structure, we call this kind of matrix Block Toeplitz Matrix.

Similarly, we can exploit the block Toeplitz structure of the matrix G , and the two terms can be computed using FFT. This would have a tremendous saving in computational time.

$$GP_i = F^{-1}\{F(G^c)F(P_i^c)\} \quad (6-25)$$

$$G'R_{i+1} = f_c F^{-1}\{F(G^c)F(R_{i+1}^{c'})\}' \quad (6-26)$$

where F denotes the two-dimensional discrete Fourier Transform, F^{-1} denotes the two-dimensional inverse discrete Fourier Transform, G^c is the convolutional variation of the original matrix G , P_i^c and R_{i+1}^c are the convolutional variations of the original vectors P_i and R_{i+1} , respectively, and $'$ denotes complex transpose.

7 ANALYSIS OF SINGLE PROBE AND PROBE ARRAY MEASUREMENTS

7.1 Objective and Unique Features

The objective of this analysis is to illustrate that by moving a single probe over the measurement plane to generate enhanced accuracy in planar near field to far field transformation[6] than over the classical Fourier based modal expansion methods. It is also illustrated that this method provides reliable results for cases when the conventional method fails. The case when the actual source plane and the measurement plane are approximately equal in size. Also, in this approach there is no need to incorporate probe correction, unlike in the existing approaches. In addition, a methodology can be designed where one can use an array of probes[7][8] instead of moving a single probe over the measurement plane, thus improving the accuracy and efficiency of the measurements. In the use of the probe array there is also no need to perform probe correction. For this proposed methodology even though there is no need to satisfy the Nyquist sampling criteria in the measurement plane, a super resolution can be achieved in the solution of the equivalent magnetic current. Also, the presence of evanescent fields in the measurements do not make this methodology unstable unlike in the conventional Fourier based techniques. The advantage of choosing a probe array for measurement is that it can eliminate the inaccuracy of mechanical movement of the probe antenna over a large planar surface and can make the measurement methodology very efficient. This is more important particularly for measurements carried out in the high frequencies, say at M, V and W-

bands. Also, one can obtain all the near field measurement information at once, thus making the entire measurement procedure very time-efficient and simple.

7.2 Implementation of the Single Probe and Probe Array Measurements

To compare the influence of the single probe and probe array measurements, there are two groups of measurements. The near-field measurements are performed over a square surface which is parallel with the source plane as shown in Fig. 7.1. The source plane (S_0) is assumed to be a square surface in the x-y plane with the dimensions $w \times w$. The distance between the source plane and the measurement plane is d .

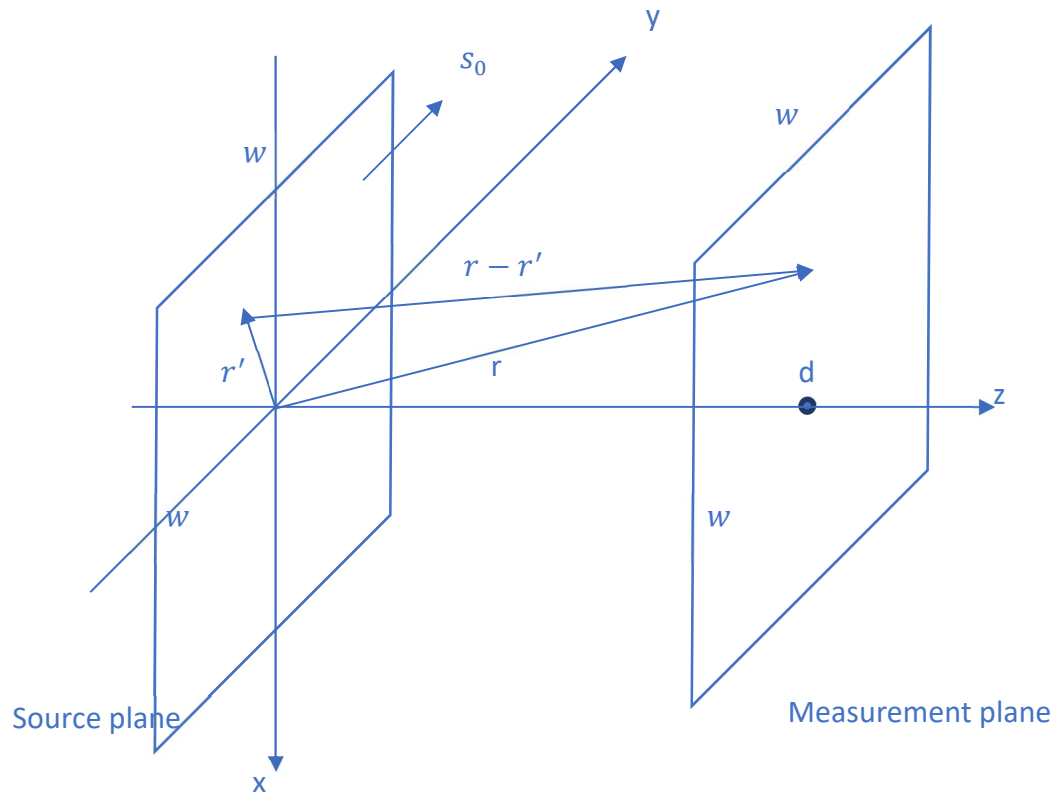


Fig. 7.1. Near field Measurement Structure.

For the first case, we use a 0.1λ length Hertzian Dipole to estimate the sampled electric fields at 0.2λ separation on the planar surface. The dipole is terminated in a 50Ω load and the voltage across the load is measured. We consider the dipole x-directed and obtain the values of the voltage (V_x) at the center point of the dipole at each measurement point P. Then the dipole is rotated to be y-directed and obtain the values of the voltage (V_y) at the center of the dipole at each measurement point P.

For the second case, we replace the single probe antenna by an array of 0.1λ dipoles all terminated in 50Ω loads and separated from each other by 0.2λ . First, the array dipoles are all x-directed to obtain the center voltage matrix $[V_x]$. Then they are rotated to be y-directed to obtain the center voltage matrix $[V_y]$.

Because the voltage V at the center of the dipole is proportional to the electric field \bar{E} at that point. We can use the voltages induced at the center points of the dipoles to estimate the near field data. From that estimated near field data, the equivalent magnetic currents (M_x, M_y) on the source plane can be calculated. By using that equivalent magnetic currents, we calculate the far field. In the end, we compare the final far field results obtained from using the two methods with the results from an electromagnetic analysis code called HOBBIES[27].

7.3 Example 7.1: Numerical results of choosing Horn antenna to be the AUT.

A 2λ by 2λ pyramidal horn antenna is used as the antenna under test. A fictitious planar surface in the x-y plane of dimensions 3λ by 3λ is used to form a planar magnetic current sheet. On the surface of the equivalent magnetic currents M_x and M_y are placed into 15×15 current patches. The near fields are sampled on a planar surface with same dimension and same discretization to enable the use of CGFFT. The distance between the source plane and the scanning plane is 3λ .

Fig. 7.2 shows the x-directed single probe measurement system. Fig. 7.3 shows the side view of the structure by using x-directed single probe as an example. Fig. 7.4 shows the x-directed probe array measurement structure. Fig. 7.5 shows the side view of the structure by using the x-directed probe array as an example. The red lines show the size of S_0 coincides with the size of measurement plane.

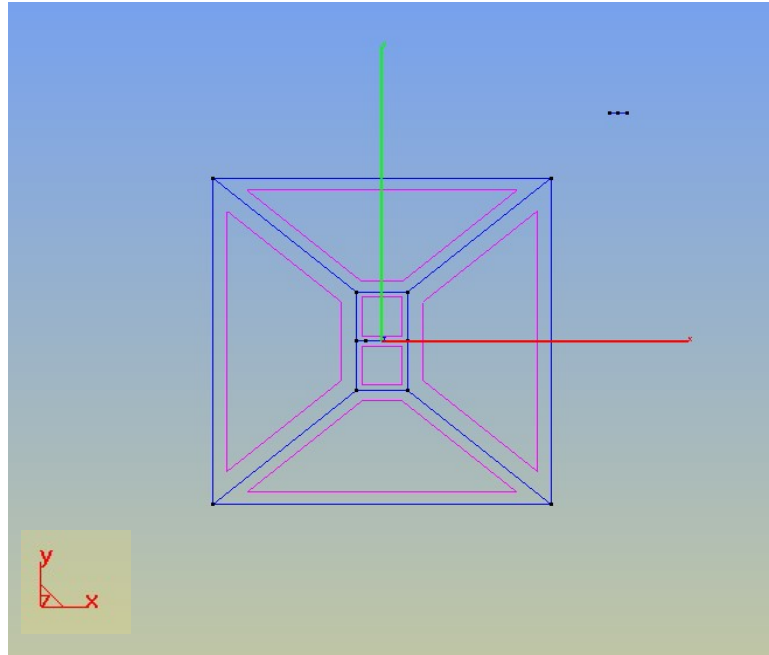


Fig. 7.2. x-directed single probe.

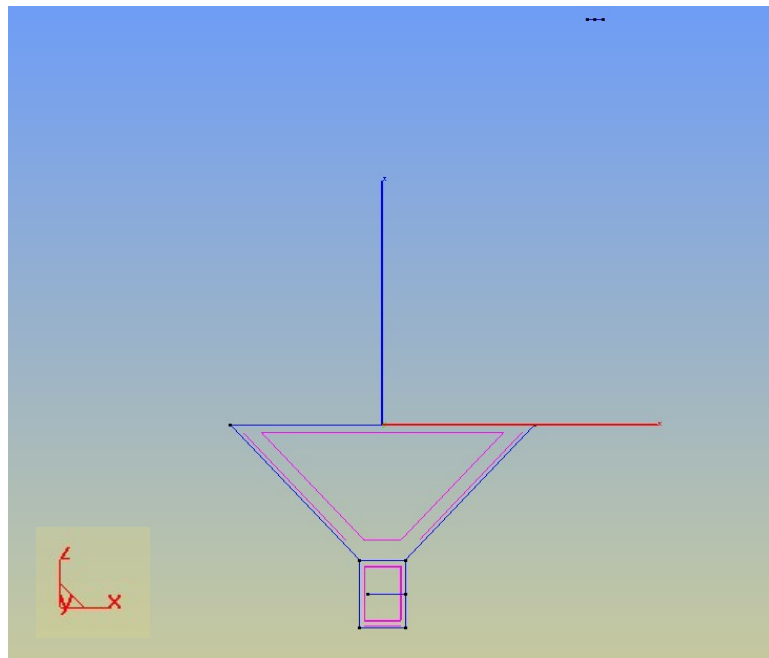


Fig. 7.3. x-directed single probe (side view).

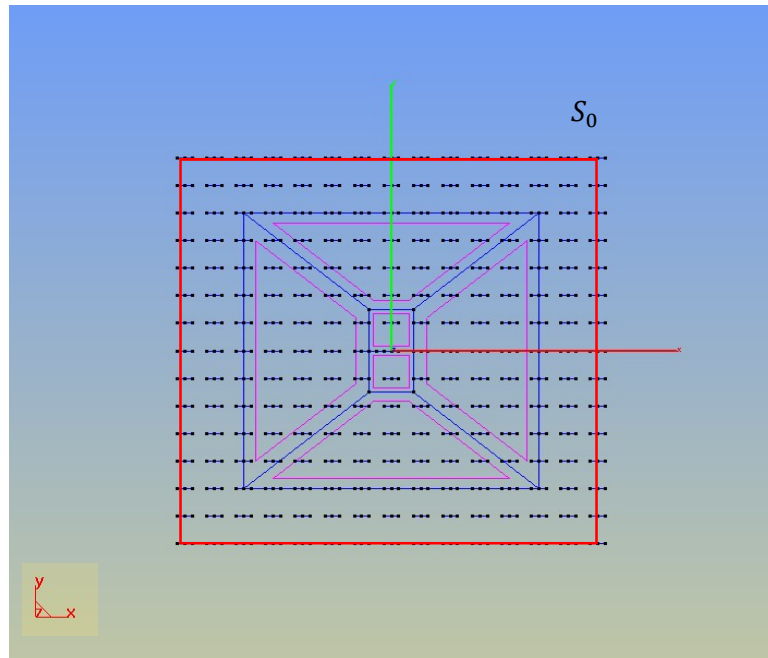


Fig. 7.4. *x*-directed probe array.

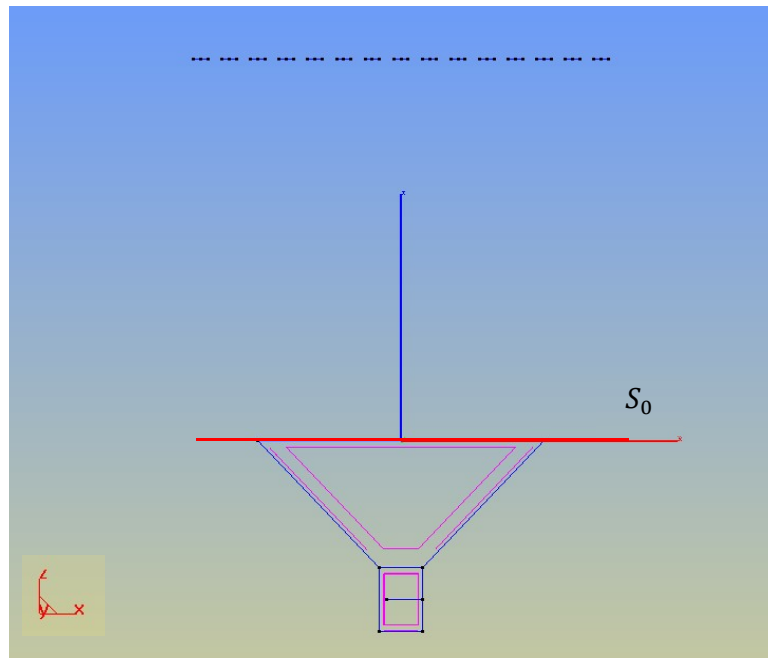


Fig. 7.5. *x*-directed probe array (side view).

The simulated results for the two methods we mentioned, and the analytic results are shown in Fig. 7.6 and Fig. 7.7. Fig. 7.6 shows the normalized absolute value of the electric far field for $\varphi = 0^\circ$ in the dB scale. Fig. 7.7 shows the normalized absolute value of the electric far field for $\varphi = 90^\circ$ in dB scale.

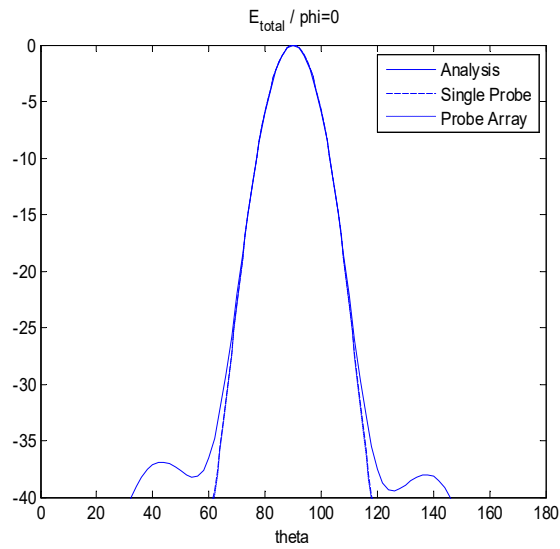


Fig. 7.6. E total when $\phi=0$ (dB Scale).

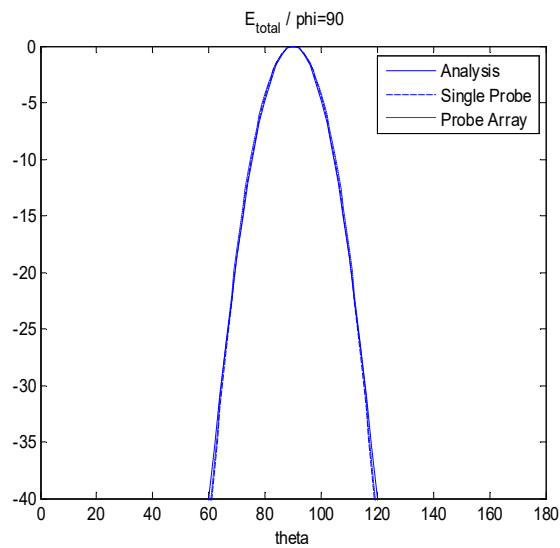


Fig. 7.7. E total when $\phi=90$ (dB Scale).

Theta here is defined as the angle from x axis to z axis and phi is the angle from the x axis to the y axis. This implies, phi equals 0° cut is the x-z plane and phi equals 90° is the y-z plane. Theta equals 0° means +x direction and theta equals 180° means -x direction. The solid lines show the analytic results obtained using HOBBIES, dashed lines show the single probe measurement results and dotted lines show the probe array measurement results.

We can see both methods we discussed above provide acceptable results. These results indicate that not incorporating probe correction into the measurement has little effect on the accuracy of the final result. Hence this methodology is much simpler and more accurate than the classical modal based planar near-field to far-field transformation.

7.4 Example 7.2: Numerical results of choosing Horn array to be the AUT

For the next example, the antenna under test is made more complicated. We choose 16, 1.5λ by 2λ pyramidal horn antennas to form a 4 by 4 horn antenna array as the antenna under test. Each horn is separated from each other by 3λ . A fictitious planar surface in the x-y plane of dimensions 10λ by 10λ is used to form a planar magnetic current sheet. On the surface of the equivalent magnetic currents M_x and M_y divided into 50×50 current patches, are assumed. The near fields are sampled on a planar surface of the same dimensions and discretized to enable use of CGFFT. The distance between the source plane and the scanning plane is 3λ .

Fig. 7.8 shows the x-directed single probe measurement system. Fig. 7.9 shows the side view of the structure by using a x-directed single probe as an example. Fig. 7.10 shows the side view of the x-directed probe array measurement structure. Fig. 7.11 shows the side view of the structure by using x-directed probe array as an example. The red lines show the size of S_0 coincides with the size of measurement plane.

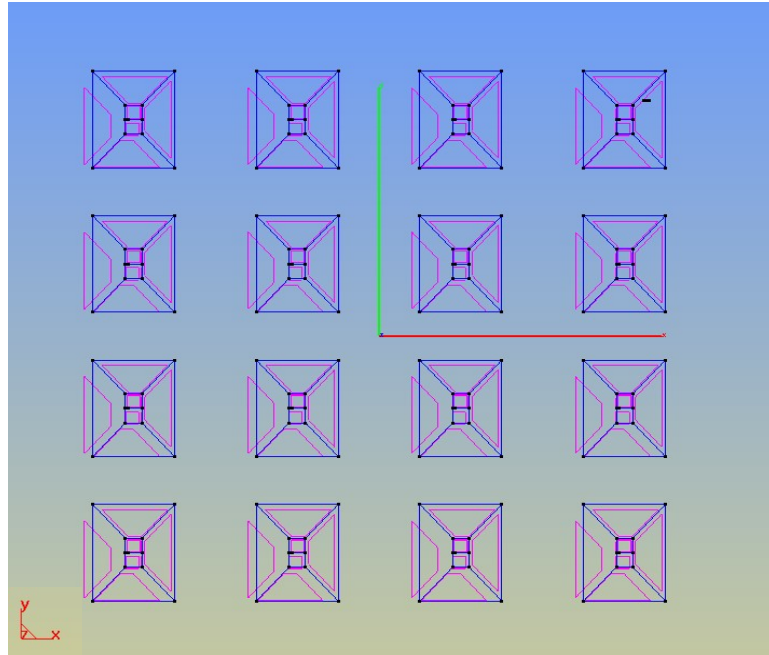


Fig. 7.8. A x-directed single probe.

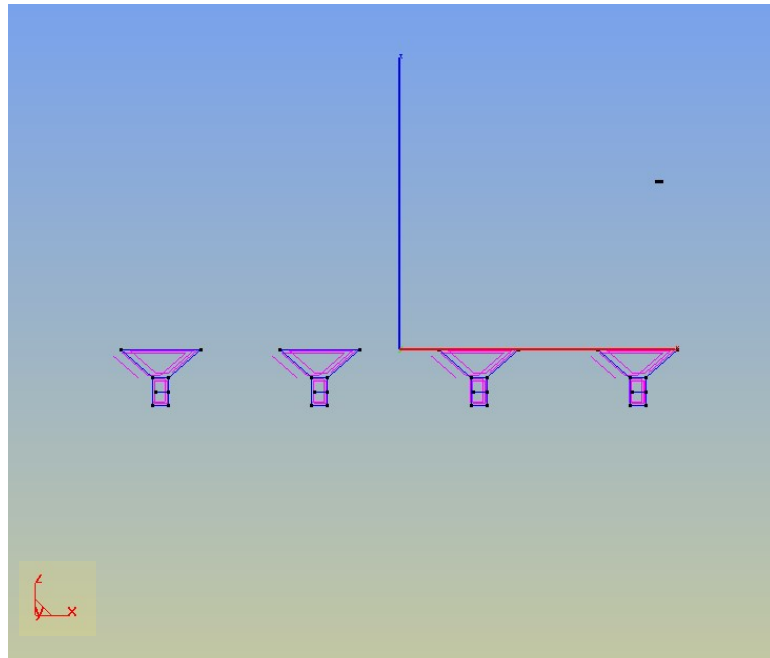


Fig. 7.9. A x-directed single probe (side view).

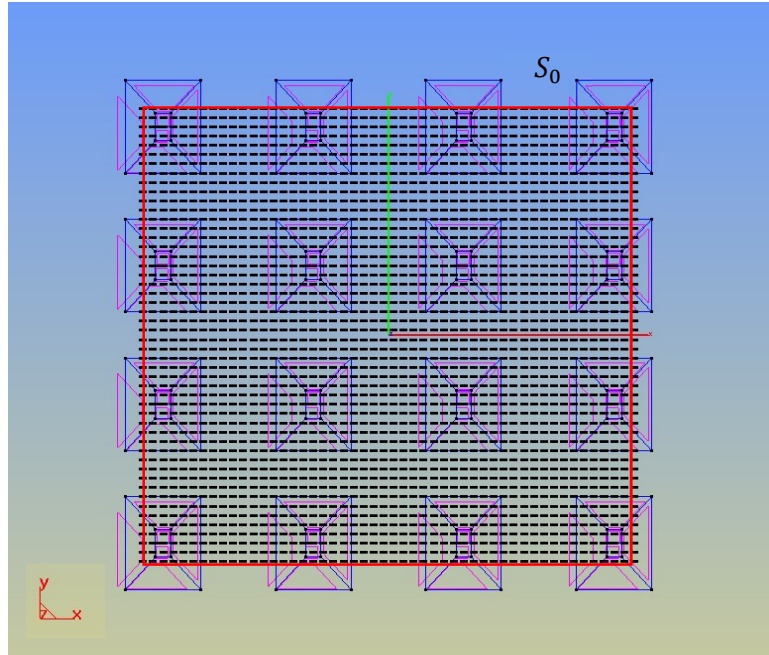


Fig. 7.10. A *x*-directed probe array.

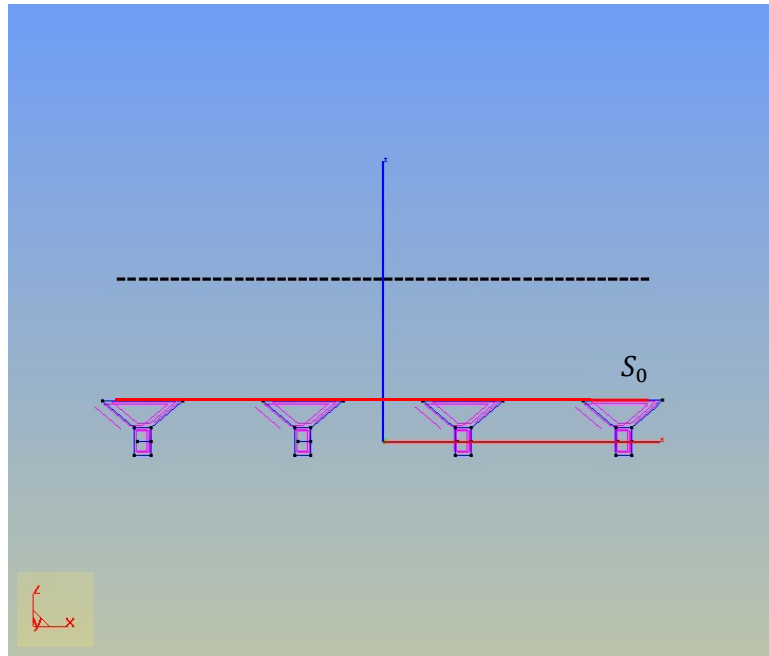


Fig. 7.11. A *x*-directed probe array (side view).

Calculated results provided by the two methods from the measured data and the analytical far field results are shown in Fig. 7.12 and Fig. 7.13. Fig. 7.12 shows the normalized absolute value of the electric far field for $\varphi = 0^\circ$ in dB scale. Fig. 7.13 shows the normalized absolute value of the electric far field for $\varphi = 90^\circ$ in dB scale.

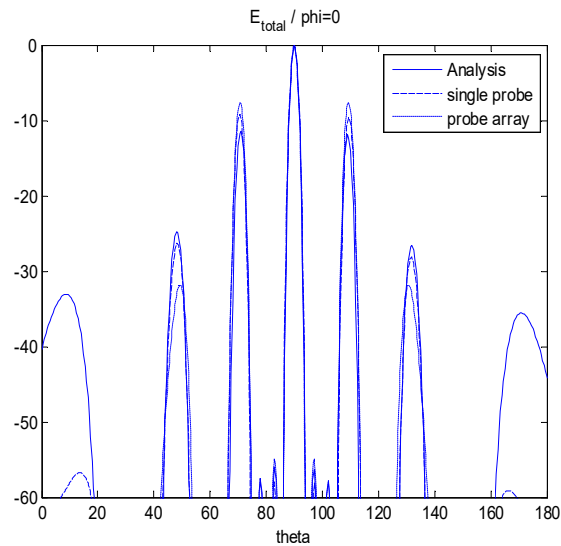


Fig. 7.12. E_{total} when $\phi = 0^\circ$ (dB Scale).

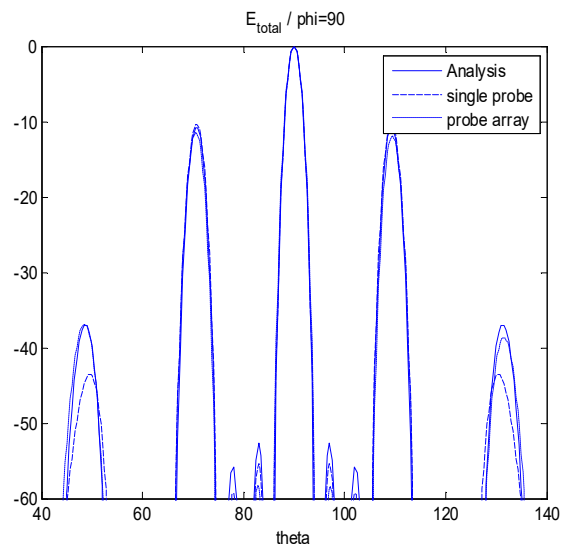


Fig. 7.13. E_{total} when $\phi = 90^\circ$ (dB Scale).

Theta here is defined as the angle from the x axis to the z axis and phi is the angle from the x axis to the y axis. The solid lines show the analytic results obtained using HOBBIES, dashed lines show the single probe measurement results and dotted lines show the probe array measurement results.

For both methods, namely use of a single probe or an array of probes in the measurement provide acceptable results. There are several observations that can be made from the results. First, the effect of mutual coupling between the probe and the array under test has little effect on the final result. Even when a probe array is used it looks like the effect of mutual coupling is still not a big problem. The other strength of this approach is that even though the size of the measurement plane barely covers the actual physical size of the antenna array, one can still obtain reliable results from 30° to 150° . Also, this computational methodology is quite fast and accurate. Finally, using this methodology the measurement plane can be deformed to any arbitrary shape and the Nyquist sampling criteria is not relevant for the measurement plane unlike in the Fourier transform based classical planar near-field to far-field transformation.

7.5 Example 7.3: Numerical results of choosing Yagi antenna to be the AUT.

For the third example a single three element Yagi-Uda antenna is selected as the antenna under test to illustrate the accuracy of this methodology. This antenna has a wide beam. Both the single probe method and the use of a probe array is used as samplers of the near field without any probe correction. The three-element Yagi-Uda antenna as shown is Fig. 7.14 consist of a driven element of length $L = 0.47 \lambda$, a reflector of length 0.482λ , and a director of length 0.442λ . They are all spaced 0.2λ apart. The radius of the wire structure for all cases is 0.00425λ .

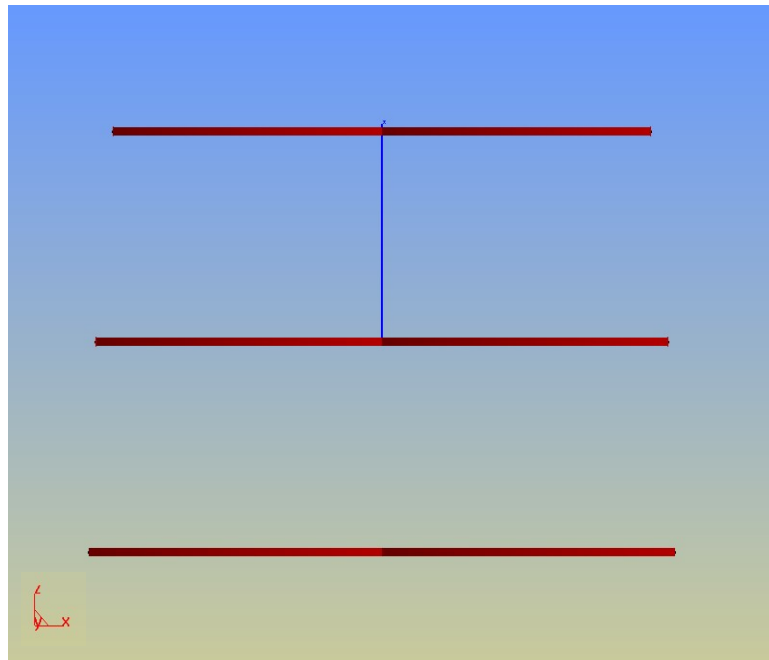


Fig. 7.14. A three-element Yagi-Uda antenna.

A fictitious planar surface in the x-y plane of dimensions 5λ by 5λ is used to approximate the equivalent source which is going to radiate the same fields in the desired region as the original antenna. On this surface equivalent magnetic currents M_x and M_y are applied. These two current components are discretized into 25×25 current patches. The two planar components of the near fields are measured on a planar surface of the same dimensions and are discretized to an equivalent value as of the same size as the equivalent current sources so as to make possible to use the CGFFT method to solve these large systems of equations using modest computational resources and using minimal CPU time. The distance between the source plane and the measurement plane is assumed to be 3λ .

The measurement methodology for this Yagi-Uda antenna is quite similar to the measurement system used for the horn antenna as described in Example 7.1.

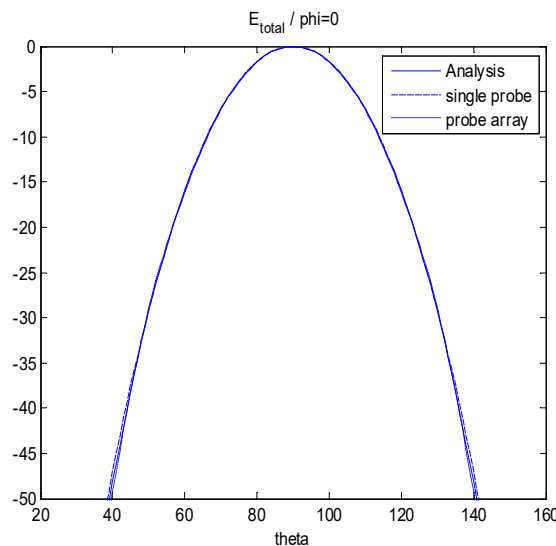


Fig. 7.15. E_{total} when $phi = 0^\circ$ (dB Scale).

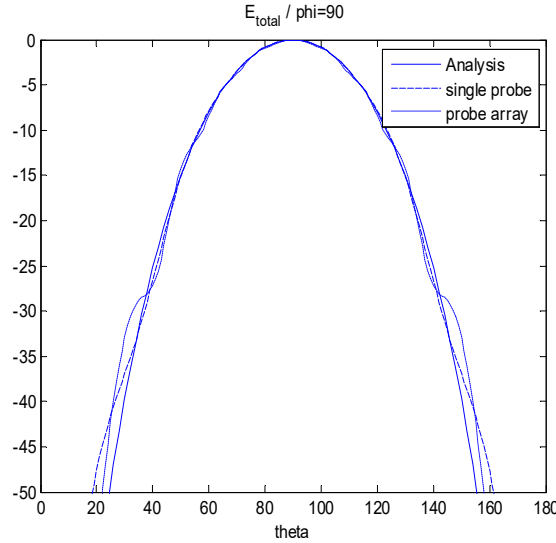


Fig. 7.16. E_{total} when $\phi = 90^\circ$ (dB Scale).

The calculated results of the two methods described earlier are used to generate the far field along with the use of an accurate numerical electromagnetic analysis tool called HOBBIES so as to assess the accuracy for the computed results obtained by the proposed methods. All the three results are presented in Fig. 7.15 and Fig. 7.16. Fig. 7.15 shows the normalized absolute value of the electric far field for $\varphi = 0^\circ$ in a dB scale. Fig. 7.16 shows the normalized absolute value of the electric far field for $\varphi = 90^\circ$ in the dB scale. Theta here is defined as the angle from x axis to z axis and phi is the angle from the x axis to the y axis, which implies phi equals 0° cut is the x-z plane and phi equals 90° cut is the y-z plane. Theta equals 0° means +x direction and theta equals 180° means -x direction. The solid lines show the analytic results obtained using HOBBIES, dashed lines show the single probe measurement results and the dotted lines show the probe array measurement results. We can see both methods we discussed above provides acceptable results further emphasizing that probe correction has little impact on this novel measurement procedure.

7.6 Example 7.4: Numerical results of choosing Yagi array to be the AUT.

For the final example, we deal with an antenna array under test. The array consists of 9 Yagi-Uda antennas to form a 3 by 3 antenna array as the antenna under test. Each element of the Yagi-Uda array has been described in example 7.3 and they are separated from each other by 2λ . A fictitious planar surface in the x - y plane of dimensions 5λ by 5λ is used to form a planar magnetic current sheet to approximate the fields that will be generated by the actual array in the desired region. On this surface, the applied equivalent magnetic currents M_x and M_y are divided into 25×25 current patches to approximate the measured electric fields on the measurement plane. The measurement plane is assumed to have the same size as that of the equivalent planar surface on which the magnetic currents are applied so as to be able to use the CGFFT method to solve the matrix equations containing the complex amplitudes of the unknown currents. The distance between the source plane and the measurement plane is 3λ .

Fig. 7.17 shows the x -directed single probe measurement system. Fig. 7.18 shows the side view of the structure by using a x -directed single probe as an example. Fig. 7.19 shows the x -directed probe array measurement set up. Fig. 7.20 shows the side view of the structure by using a x -directed probe array as an example. The red lines show the size of S_0 coincides with the size of measurement plane.

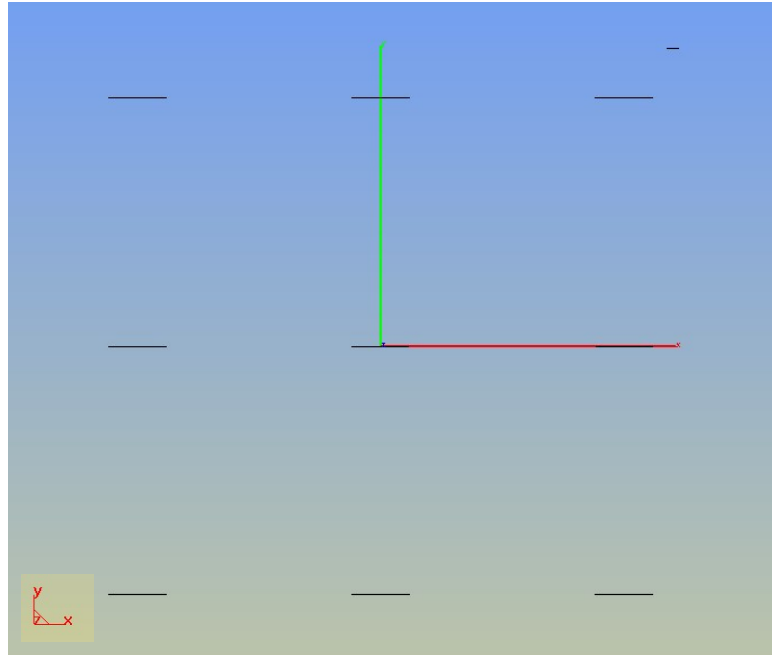


Fig. 7.17. A x-directed single probe.

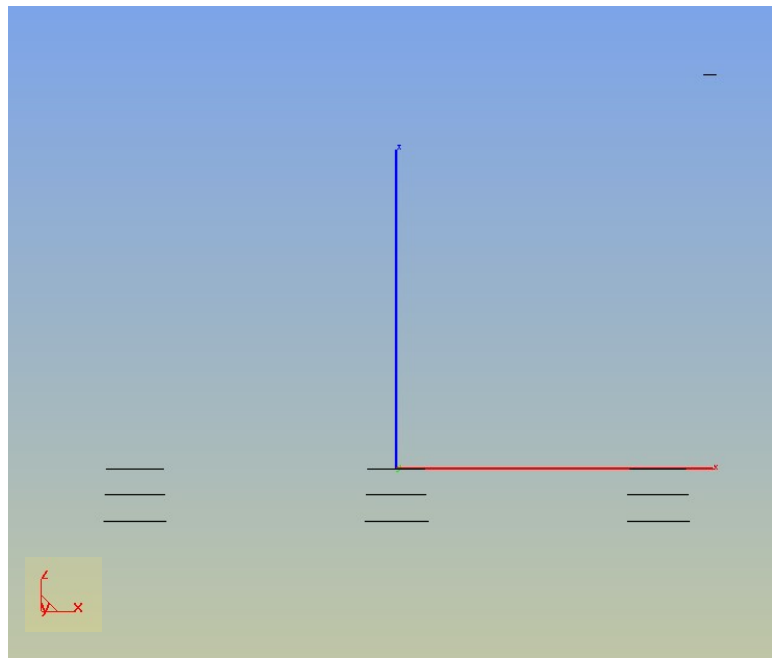


Fig. 7.18. A x-directed single probe (side view).

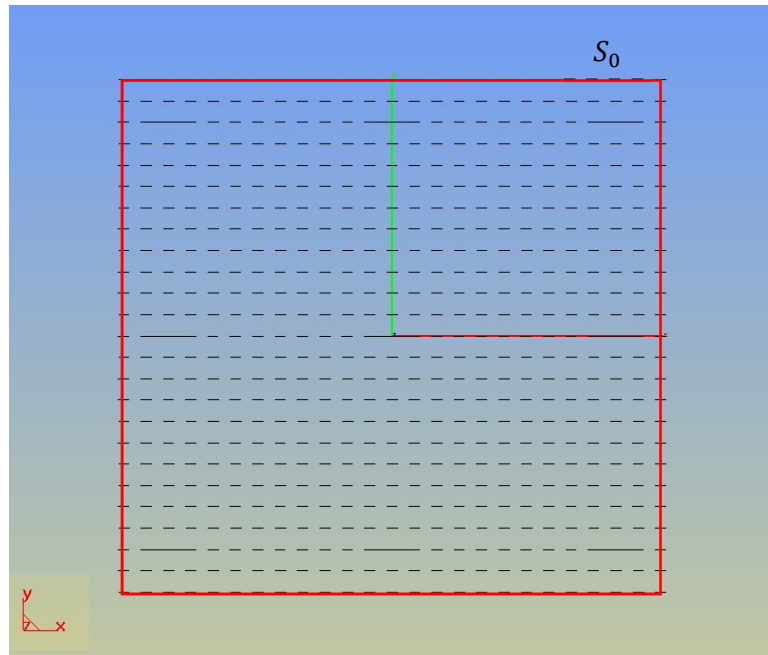


Fig. 7.19. A x-directed probe array.

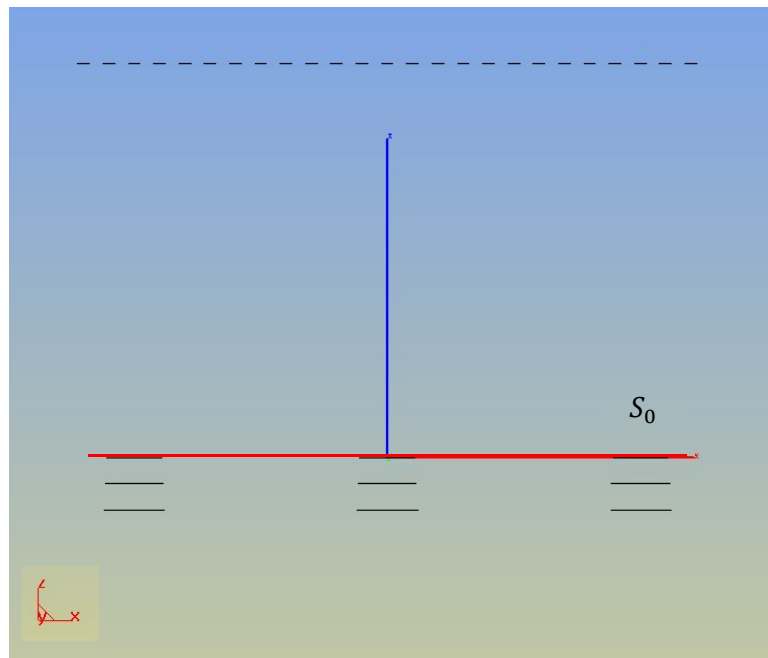


Fig. 7.20. A x-directed probe array (side view).

The calculated results for the far field obtained by the two methods described in this paper, namely sliding a single probe and using a probe array along with the results computed by a numerical electromagnetics code HOBBIIES invoking the electric field integral equation in Fig. 7.21 and Fig. 7.22. Fig. 7.21 shows the normalized absolute value of the electric far field for $\varphi = 0^\circ$ in a dB scale. Fig. 7.22 shows the normalized absolute value of the electric far field for $\varphi = 90^\circ$ in a dB scale.

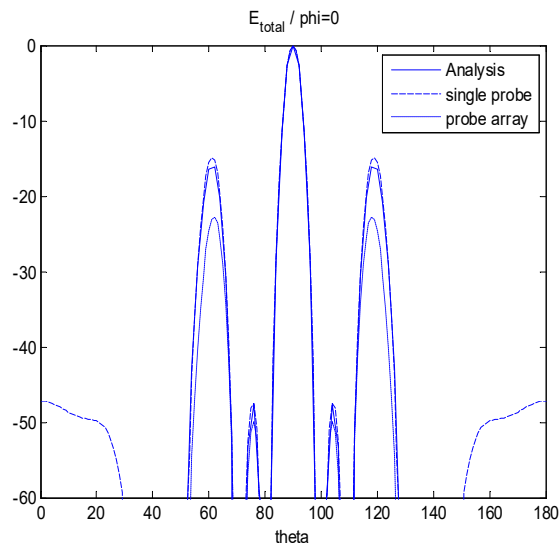


Fig. 7.21. E_{total} when $\phi = 0^\circ$ (dB Scale).

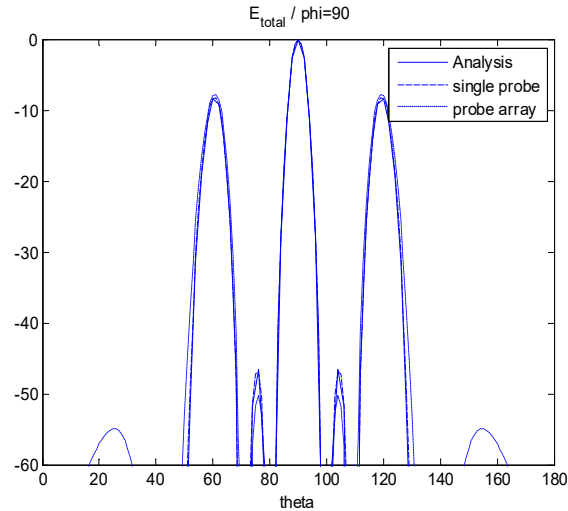


Fig. 7.22. E_{total} when $\phi = 90^\circ$ (dB Scale).

Theta here is defined as the angle from the x axis to the z axis and phi is the angle from the x axis to the y axis. This implies that phi equals 0 cut is the x-z plane and phi equals 90 is the y-z plane. Theta equals 0 implies +x direction and theta equals 180 implies -x direction. The solid lines show the analytic results obtained using HOBBIES, dashed lines show the single probe measurement result and the dotted lines show the results from the probe array measurement.

We can see both methods we discussed above provides acceptable results and that probe correction is not at all a requirement for this methodology. In this case, acceptable results are obtained from 40° to 140° . For the classical approach of planar modal expansion, it will not have been possible to solve this problem for the given data as in this case the source and the measurement planes are of the same size!

8 THE INFLUENCE OF THE SIZE OF SQUARE DIPOLE PROBE ARRAY MEASUREMENT ON THE ACCURACY OF NF-FF PATTERN

8.1 Objective and Necessity of the Analysis

In the previous chapters, we already showed that both single probe and probe array methods can provide acceptable results and that probe correction is not at all a requirement for the methodology. We also pointed out that compared to the single probe method, the probe array method is much more time-efficient and simple. The objective of this chapter is to illustrate the influence of the size of the measurement plane on the accuracy of the far field pattern result using the near field square dipole probe array measurement to far field transformation approach[9]. Compared to the classical Fourier based modal expansion methods, square dipole probe array method provides reliable results for cases when the conventional method fails for the case when the actual source plane and the measurement plane are approximately equal in size. Also, in this approach there is no need to incorporate probe correction unlike in the existing approaches. In addition, the methodology of using probe array instead of moving a single probe over the measurement plane improved the accuracy and efficiency of the whole process. We expect that the larger the size of the measurement plane, the more accurate the result. The question is what the relation between the accuracy and the size of the measurement plane is so we can make a smart choice to get accurate results efficiently. Sample numerical results are presented to illustrate how

accurate it can be and what the relation between the size of the near field measurement plane and the accuracy of the final result is.

8.2 Implementation Procedure

The near-field measurements are performed over a square surface which is parallel with the source plane as shown in Fig. 8.1. The source plane (S_0) is assumed to be a square surface in the x-y plane with the dimensions from $w_S \times w_S$ to $w_L \times w_L$. The distance between the source plane and the measurement plane is d .

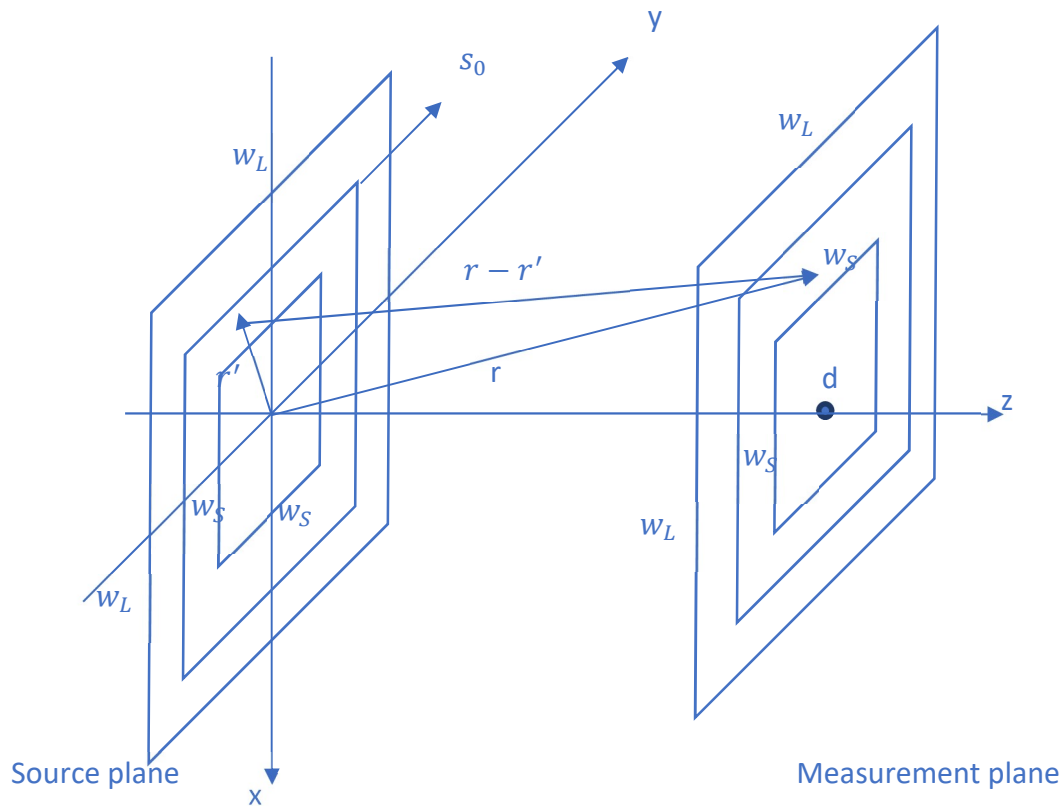


Fig. 8.1. Near field measurement structure of different sizes.

As we mentioned, we use 0.1λ length Hertzian Dipole array of different sizes to estimate the sampled electric fields at certain separations on the measurement planar surfaces (for those antennas under test with complicated structures, we are going to show the results with different separations as shown in Example 8.2 and Example 8.4). The dipole probes are all terminated in 50Ω loads and the voltages across the loads are measured.

First the array of dipoles are all x -directed to obtain the value of the voltage matrix $[V_x]$ across the loads. Then they are rotated to be y -directed to obtain the voltage matrix $[V_y]$. It is estimated that the voltage V at the center of the dipole is proportional to the electric field \bar{E} at that point. We can normalize the voltages induced at the center points of the dipoles and use that information to estimate the values for the sampled near field data. From that estimated near field data, the equivalent magnetic currents (M_x, M_y) on the source plane can be calculated and used to calculate the far field. In the end, we compare the final far field results obtained from using different sizes of measurement planes with the results from an electromagnetic analysis code called HOBBIES [27] and analyze the relation between the size and the accuracy. Here we define a relative error as follows,

$$e = \sum_{\theta=0^{\circ}}^{\theta=180^{\circ}} (E_{theory} - E_{Cal})^2 \quad (8-1)$$

where, e is the relative error, E_{theory} is the theoretical far field result simulated by HOBBIES at one cut, and E_{Cal} is the result obtained from the NF-FF approach we mentioned above at the same cut.

8.3 Example 8.1: Numerical results of choosing Horn antenna to be the AUT.

A 2λ by 2λ pyramidal horn antenna is used as the antenna under test. The distance between the source plane and the scanning plane is 3λ . In this case the size of the actual source plane of the antenna under test is 2λ by 2λ .

The number of the measurement dipoles starts from 4 by 4 and end up with 100 by 100. In order to keep the symmetry, we increase the number of dipoles on each side by a factor of 2 at a time, and we chose the separation between dipoles in both directions to be 0.2λ . Which means the measurement plane start from the dimensions of 0.8λ by 0.8λ to 20λ by 20λ . On the surface of the equivalent magnetic currents M_x and M_y are placed into same dimensions and discretized to enable the use of CGFFT.

Fig. 8.2. shows the 10 by 10 x-directed probe array with 0.2λ separations in both directions structure as an example. Fig. 8.3 shows the side view of the structure by using the 10 by 10 x-directed probe array with 0.2λ separations in both directions as an example.

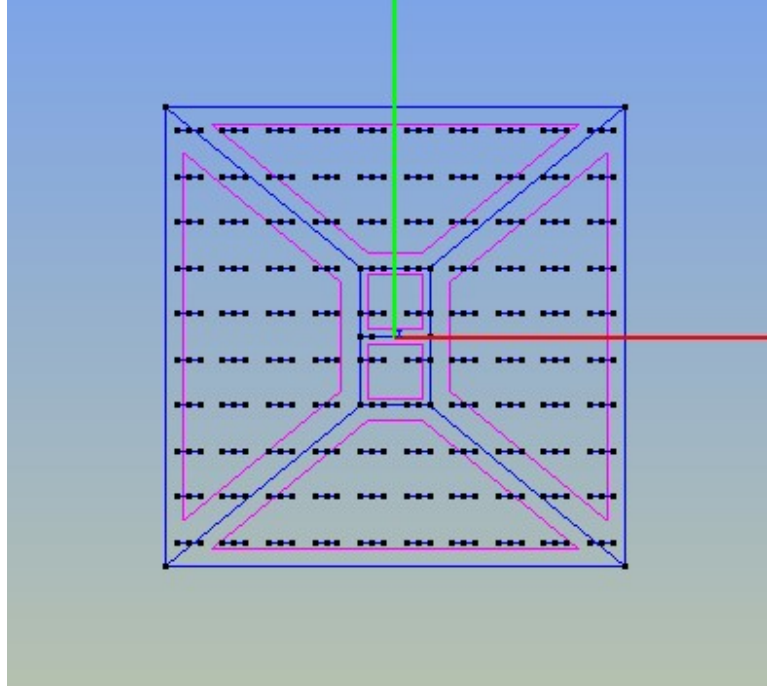


Fig. 8.2. 10 by 10 x-directed probe array with 0.2λ separations in both directions.

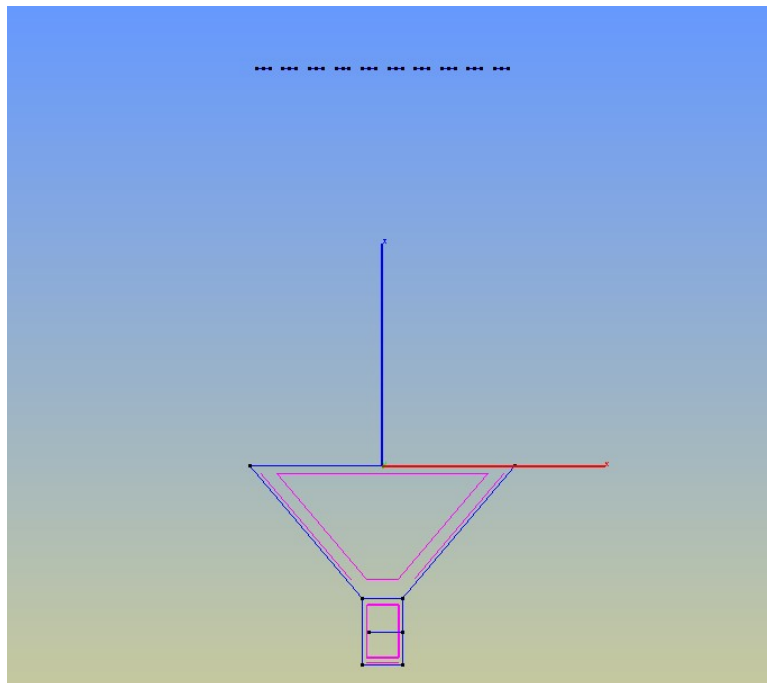


Fig. 8.3. 10 by 10 x-directed probe array with 0.2λ separations in both directions (side view).

The simulated results for all the sizes of the measurement planes from 0.8λ by 0.8λ to 20λ by 20λ mentioned above and the analytic results for the far fields are shown in Fig. 8.4 and Fig. 8.5.

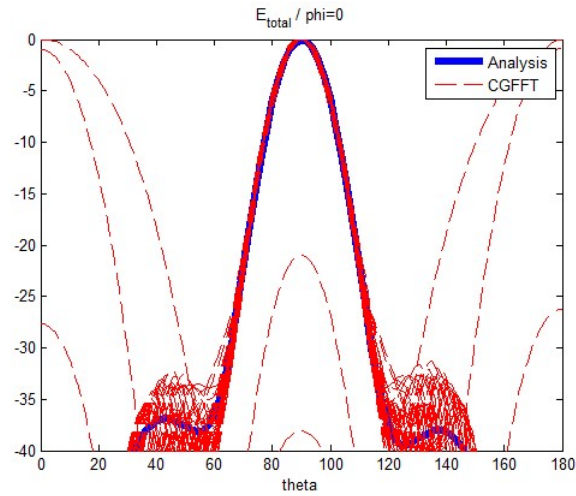


Fig. 8.4. E_{total} when $\phi = 0^\circ$ (dB Scale) for all sizes of the measurement planes from 0.8λ by 0.8λ to 20λ by 20λ with 0.2λ separations in both directions.

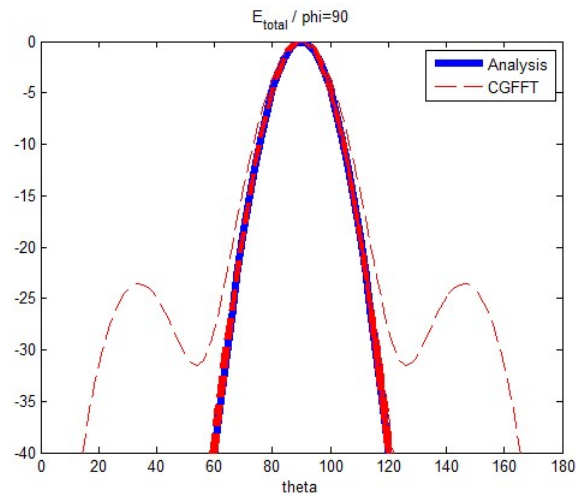


Fig. 8.5. E_{total} when $\phi = 90^\circ$ (dB Scale) for all sizes of the measurement planes from 0.8λ by 0.8λ to 20λ by 20λ with 0.2λ separations in both directions.

Theta here is defined as the angle from x axis to z axis and phi is the angle from the x axis to the y axis. This implies, phi equals 0° cut is the x-z plane and phi equals 90° is the y-z plane. The solid blue lines show the analytic results obtained using HOBBIES, dashed red lines show the results obtained using different sizes of square dipole probe array measurement.

As we can see from Fig. 8.4 and Fig. 8.5 that most of the dashed red lines are acute respect to the solid blue line, and a little portion of the dashed red lines are inaccurate. It's necessary for us the analyze the relation between the relative error we mentioned above and the size of the measurement plane. The relations are shown in Fig. 8.6 and Fig. 8.7. Fig. 8.6 shows the relative error at different sizes of measurement planes with 0.2λ separations in both directions for $\phi = 0^\circ$ and Fig. 8.7 shows the relative error at different sizes of measurement planes with 0.2λ separations in both directions for $\phi = 90^\circ$.

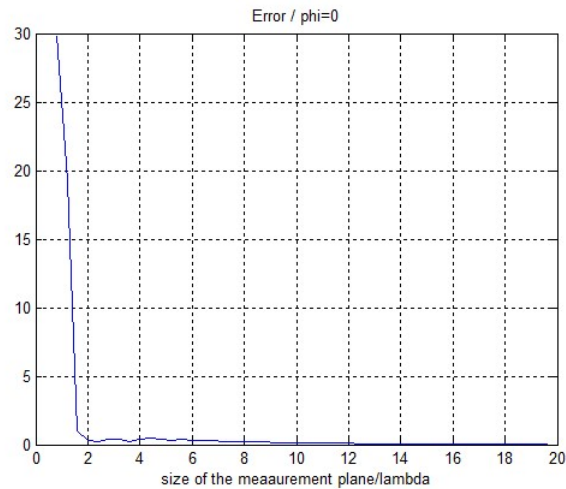


Fig. 8.6. Relative error at different sizes of measurement planes with 0.2λ separations in both directions ($\phi = 0^\circ$).

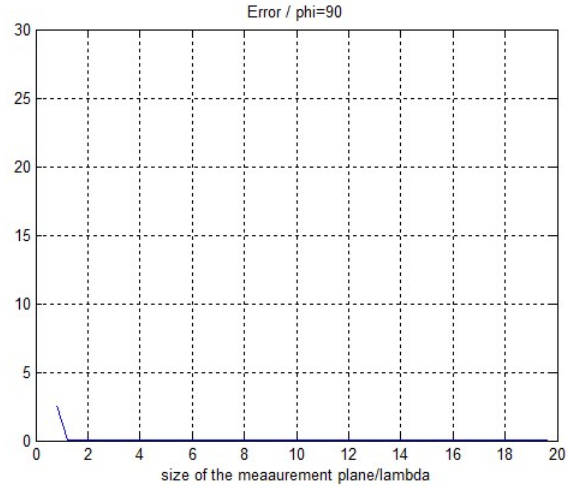


Fig. 8.7. Relative error at different sizes of measurement planes with 0.2λ separations in both directions ($\phi = 90^\circ$).

After we observe the relative error plots of both cuts, we can easily find that it goes down close to zero after the size of the measurement larger than 2λ .

Notice that 2λ is also the size of the actual source plane of the antenna under test. Also, the far field results obtained from the sizes of measurement planes which are larger than 2λ are as shown in Fig. 8.8 and Fig. 8.9. Fig. 8.8 shows the normalized absolute value of the electric far field for $\phi = 0^\circ$ in a dB scale for all sizes of the measurement planes from 2λ by 2λ to 20λ by 20λ with 0.2λ separations in both directions. Fig. 8.9 shows the normalized absolute value of the electric far field for $\phi = 0^\circ$ in a dB scale for all sizes of the measurement planes from 2λ by 2λ to 20λ by 20λ with 0.2λ separations in both directions. We can see that all the inaccurate red dashed lines disappear and only the accurate ones left. We can see that after the size of the measurement plane chosen to be larger than the size of the actual source plane of the antenna under test, our NF-FF approach provides acceptable results.

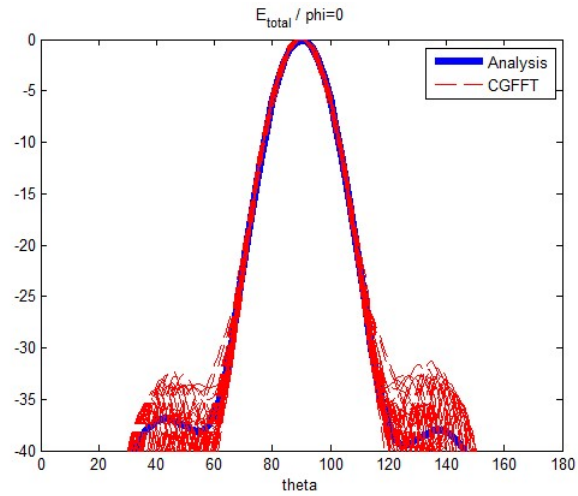


Fig. 8.8. E_{total} when $\phi = 0^\circ$ (dB Scale) for all sizes of the measurement planes from 2λ by 2λ to 20λ by 20λ with 0.2λ separations in both directions.

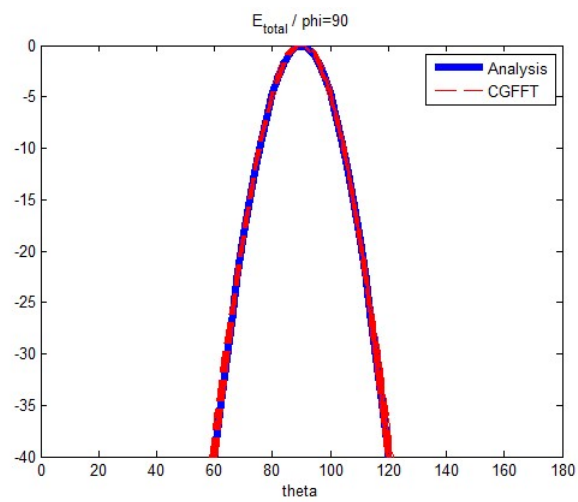


Fig. 8.9. E_{total} when $\phi = 90^\circ$ (dB Scale) for all sizes of the measurement planes from 2λ by 2λ to 20λ by 20λ with 0.2λ separations in both directions.

8.4 Example 8.2: Numerical results of choosing Horn array to be the AUT.

For the next example, the antenna under test is made more complicated. We choose 16, 1.5λ by 2λ pyramidal horn antennas to form a 4 by 4 horn antenna array as the antenna under test. Each horn is separated from each other by 3λ . The distance between the source plane and the scanning plane is 3λ . In this case the size of the actual source plane of the antenna under test is 10.5λ by 11λ .

We did 3 different groups of measurements:

Group 1: The number of the measurement dipoles starts from 4 by 4 and end up with 100 by 100. In order to keep the symmetry, we increase the number of dipoles on each side by a factor of 2 at a time, and we chose the separation between dipoles in both directions to be 0.2λ . Which means the measurement plane start from the dimensions of 0.8λ by 0.8λ to 20λ by 20λ . On the surface of the equivalent magnetic currents M_x and M_y are placed into same dimensions and discretized to enable the use of CGFFT.

Group 2: The number of the measurement dipoles starts from 4 by 4 and end up with 50 by 50. In order to keep the symmetry, we increase the number of dipoles on each side by a factor of 2 at a time, and we chose the separation between dipoles in both directions to be 0.4λ . Which means the measurement plane start from the dimensions of 1.6λ by 1.6λ to 20λ by 20λ . On the surface of the equivalent magnetic currents M_x and M_y are placed into same dimensions and discretized to enable the use of CGFFT.

Group 3: The number of the measurement dipoles starts from 4 by 4 and end up with 40 by 40. In order to keep the symmetry, we increase the number of dipoles on each side by a factor of 2 at a time, and we chose the separation between dipoles in both directions to be 0.5λ . Which means the measurement plane start from the dimensions of 2λ by 2λ to 20λ by 20λ . On the surface of the equivalent magnetic currents M_x and M_y are placed into same dimensions and discretized to enable the use of CGFFT.

Fig. 8.10. shows the 50 by 50 x-directed probe array with 0.2λ separations in both directions structure as an example. Fig. 8.11 shows the side view of the structure by using the 50 by 50 x-directed probe array with 0.2λ separations in both directions as an example.

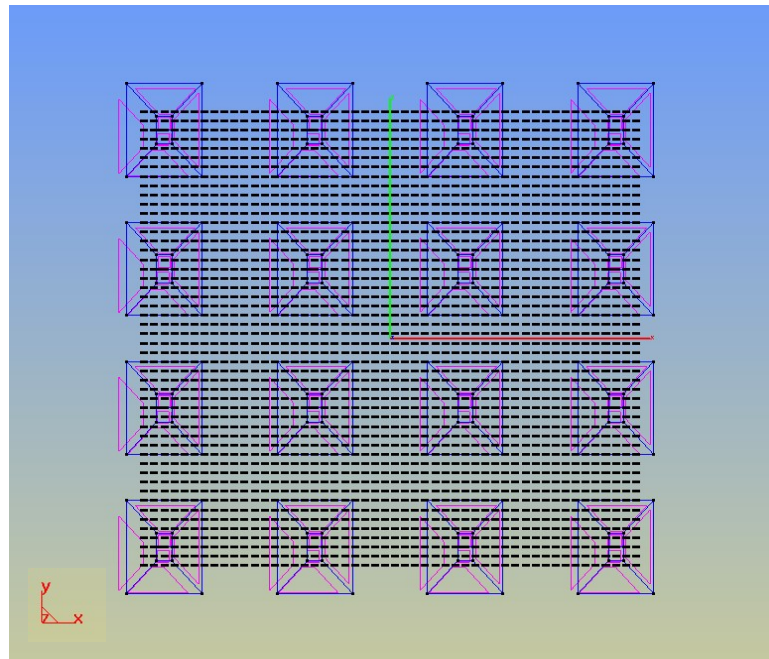


Fig. 8.10. 50 by 50 x-directed probe array with 0.2λ separations in both directions.

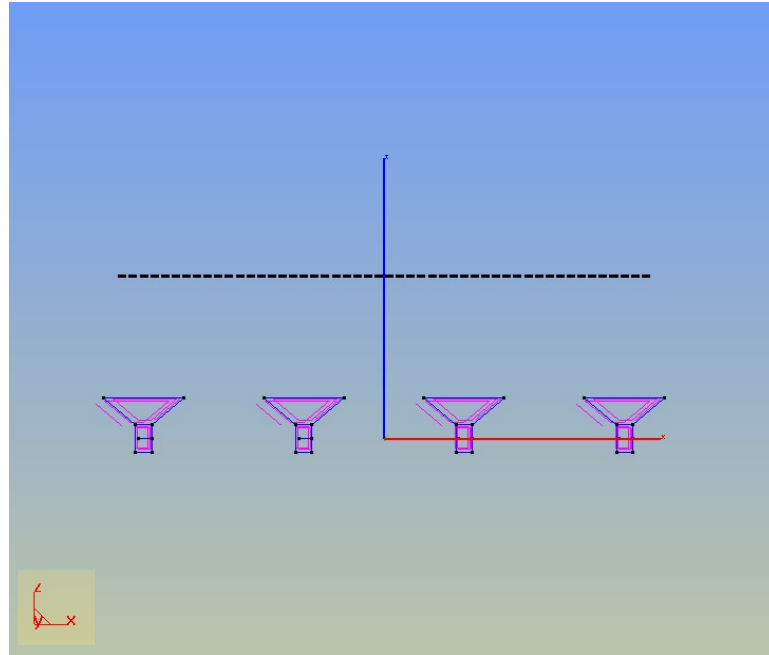


Fig. 8.11. 50 by 50 x-directed probe array with 0.2λ separations in both directions (side view).

The simulated results for measurement group 1 where all the sizes of the measurement planes are from 0.8λ by 0.8λ to 20λ by 20λ with 0.2λ separations in both directions which we mentioned above and the analytic results for the far fields are shown in Fig. 8.12 and Fig. 8.13 as an example. Where Fig. 8.12 shows the normalized absolute value of the electric far field for $\varphi = 0^\circ$ in the dB scale. Fig. 8.13 shows the normalized absolute value of the electric far field for $\varphi = 90^\circ$ in the dB scale. Theta here is defined as the angle from x axis to z axis and phi is the angle from the x axis to the y axis. This implies, phi equals 0° cut is the x-z plane and phi equals 90° is the y-z plane. The solid blue lines show the analytic results obtained using HOBBIES, dashed red lines show the results obtained using different sizes of square dipole probe array measurement.

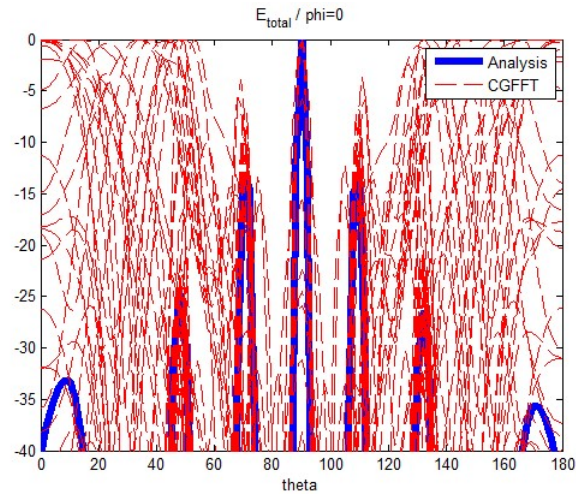


Fig. 8.12. E_{total} when $\phi = 0^\circ$ (dB Scale) for all sizes of the measurement planes from 0.8λ by 0.8λ to 20λ by 20λ with 0.2λ separations in both directions.

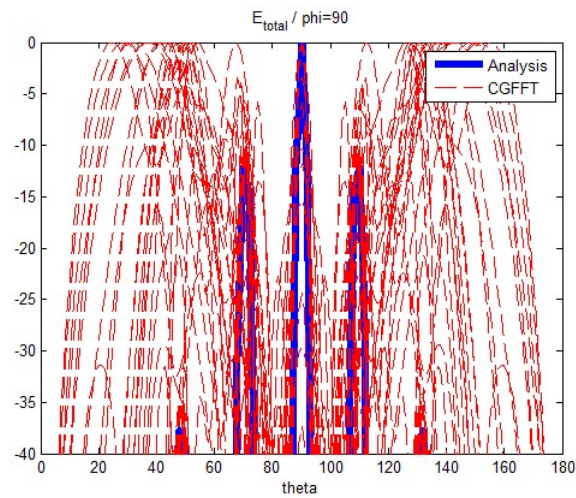


Fig. 8.13. E_{total} when $\phi = 90^\circ$ (dB Scale) for all sizes of the measurement planes from 0.8λ by 0.8λ to 20λ by 20λ with 0.2λ separations in both directions.

As we can see from Fig. 8.12 and Fig. 8.13 that most of the dashed red lines are acute respect to the solid blue line, and some portion of the dashed red lines are inaccurate. It's

necessary for us to analyze the relation between the relative error we mentioned above and the size of the measurement plane. The relations are shown in Fig. 8.14 and Fig. 8.15.

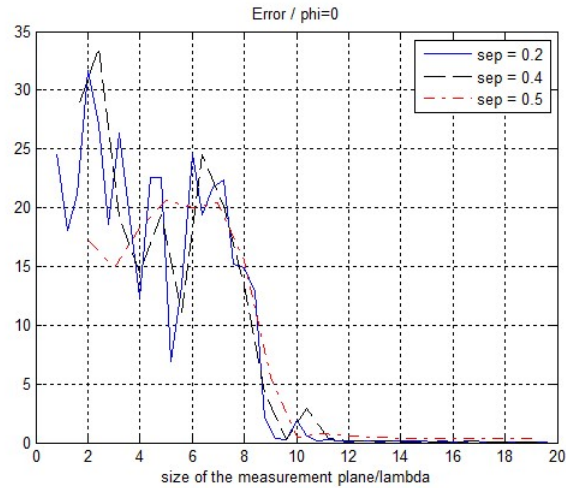


Fig. 8.14. Relative error at different sizes of measurement planes with 0.2λ , 0.4λ , 0.5λ separations in both directions ($\phi = 0^\circ$).

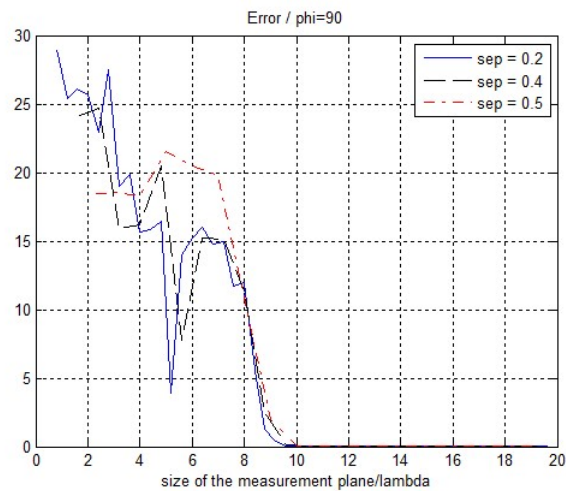


Fig. 8.15. Relative error at different sizes of measurement planes with 0.2λ , 0.4λ , 0.5λ separations in both directions ($\phi = 90^\circ$).

After we observe the relative error plots of both cuts, we can easily find that it goes down close to zero after the size of the measurement larger than 10λ . The remarkable point is that the relative error goes down close to zero for all the 3 groups of measurements with different separations (0.2λ , 0.4λ , 0.5λ) at about the same size of measurement plane. Notice that 11λ is about the size of the actual source plane of the antenna under test. Also, the far field results obtained from the sizes of measurement planes with 0.2λ separations in both directions which are larger than 10λ are as shown in Fig. 8.16 and Fig. 8.17. The far field results obtained from the sizes of measurement planes with 0.4λ separations in both directions which are larger than 10λ are as shown in Fig. 8.18 and Fig. 8.19. The far field results obtained from the sizes of measurement planes with 0.5λ separations in both directions which are larger than 10λ are as shown in Fig. 8.20 and Fig. 8.21. We can see that all the inaccurate red dashed lines disappear and only the accurate ones left.

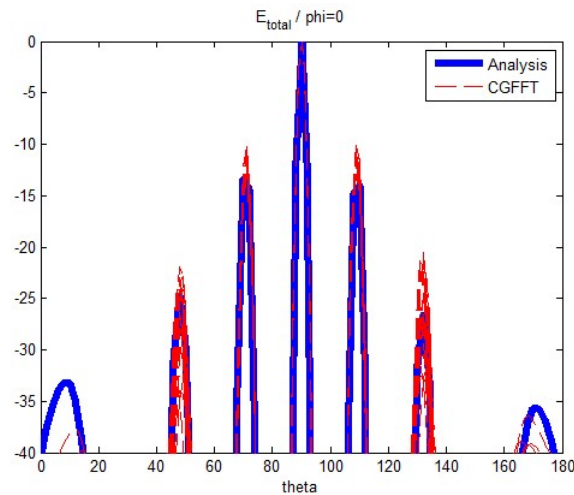


Fig. 8.16. E_{total} when $\phi = 0^\circ$ (dB Scale) for all sizes of the measurement planes from 10λ by 10λ to 20λ by 20λ with 0.2λ separations in both directions.

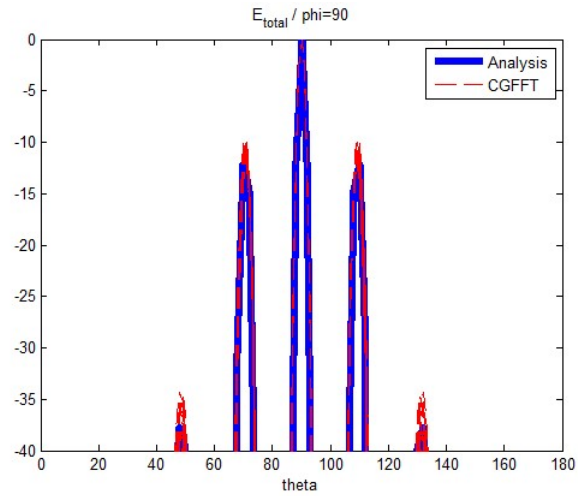


Fig. 8.17. E_{total} when $\phi = 90^\circ$ (dB Scale) for all sizes of the measurement planes from 10λ by 10λ to 20λ by 20λ with 0.2λ separations in both directions.

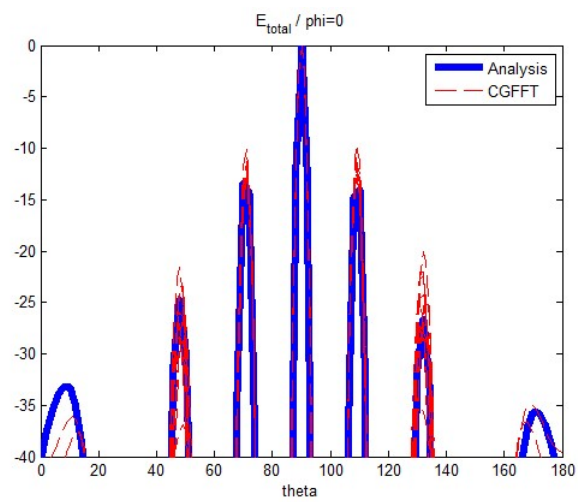


Fig. 8.18. E_{total} when $\phi = 0^\circ$ (dB Scale) for all sizes of the measurement planes from 10λ by 10λ to 20λ by 20λ with 0.4λ separations in both directions.

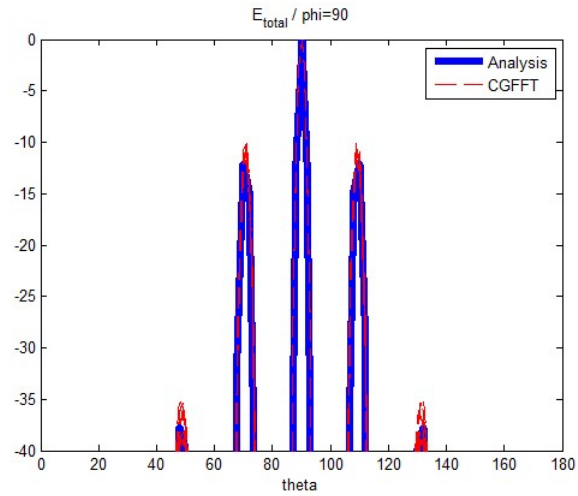


Fig. 8.19. E_{total} when $\phi = 90^\circ$ (dB Scale) for all sizes of the measurement planes from 10λ by 10λ to 20λ by 20λ with 0.4λ separations in both directions.

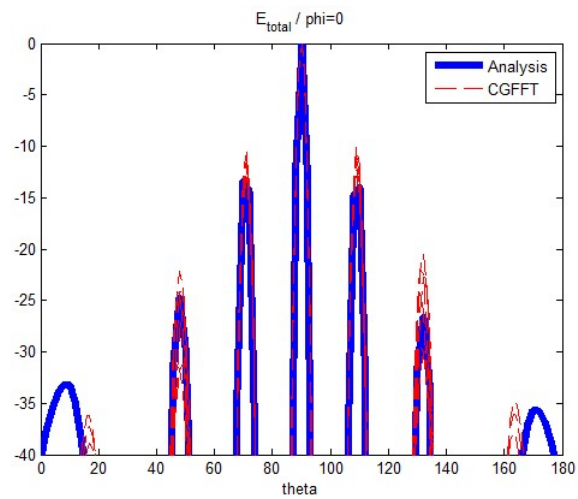


Fig. 8.20. E_{total} when $\phi = 0^\circ$ (dB Scale) for all sizes of the measurement planes from 10λ by 10λ to 20λ by 20λ with 0.5λ separations in both directions.

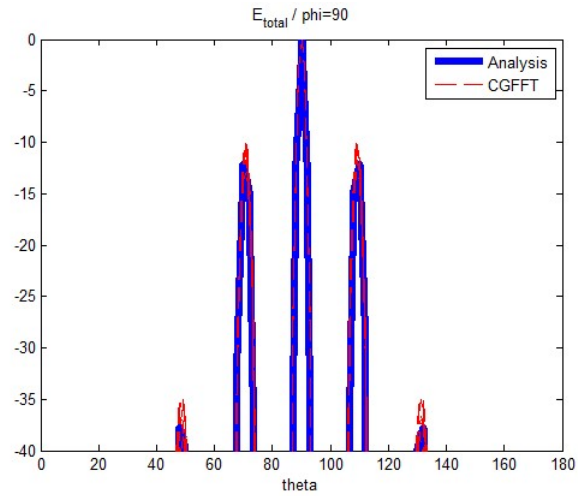


Fig. 8.21. E_{total} when $\phi = 90^\circ$ (dB Scale) for all sizes of the measurement planes from 10λ by 10λ to 20λ by 20λ with 0.5λ separations in both directions.

We can see that after the size of the measurement plane chosen to be close to or larger than the size of the actual source plane of the antenna under test, our NF-FF approach provides acceptable results.

8.5 Example 8.3: Numerical results of choosing Yagi antenna to be the AUT.

For the third example a single three element Yagi-Uda antenna is selected as the antenna under test to illustrate the accuracy of this methodology. This antenna has a wide beam. The three-element Yagi-Uda antenna as shown in Fig. 8.22 consist of a driven element of length $L = 0.47 \lambda$, a reflector of length 0.482λ , and a director of length 0.442λ . They are all spaced 0.2λ apart. The radius of the wire structure for all cases is 0.00425λ . The distance between the source plane and the measurement plane is assumed to be 3λ . In this case the size of the actual source plane of the antenna under test is around 0.5λ line source. The measurement methodology for this Yagi-Uda antenna is quite similar to the measurement system used for the horn antenna as described in Example 8.1.

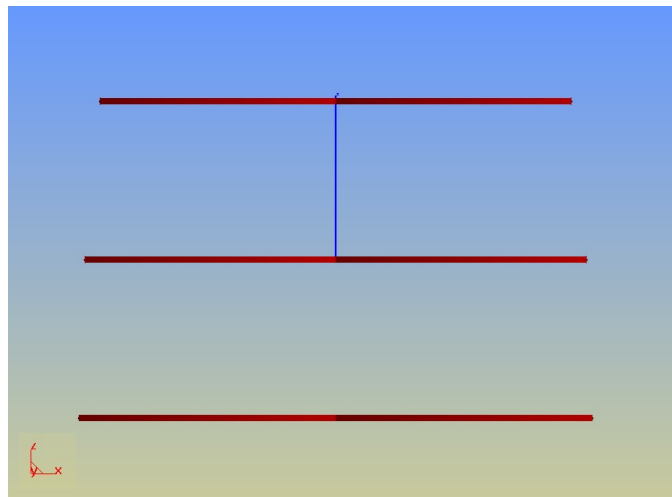


Fig. 8.22. A three-element Yagi-Uda antenna.

The number of the measurement dipoles starts from 4 by 4 and end up with 100 by 100. In order to keep the symmetry, we increase the number of dipoles on each side by a factor

of 2 at a time, and we chose the separation between dipoles in both directions to be 0.2λ . Which means the measurement plane start from the dimensions of 0.8λ by 0.8λ to 20λ by 20λ . On the surface of the equivalent magnetic currents M_x and M_y are placed into same dimensions and discretized to enable the use of CGFFT.

The simulated results for all the sizes of the measurement planes from 0.8λ by 0.8λ to 20λ by 20λ mentioned above and the analytic results for the far fields are shown in Fig. 8.23 and Fig. 8.24. Where Fig. 8.23 shows the normalized absolute value of the electric far field for $\varphi = 0^\circ$ in the dB scale. Fig. 8.24 shows the normalized absolute value of the electric far field for $\varphi = 90^\circ$ in the dB scale. Theta here is defined as the angle from x axis to z axis and phi is the angle from the x axis to the y axis. This implies, phi equals 0° cut is the x-z plane and phi equals 90° is the y-z plane. The solid blue lines show the analytic results obtained using HOBBIES, dashed red lines show the results obtained using different sizes of square dipole probe array measurement.

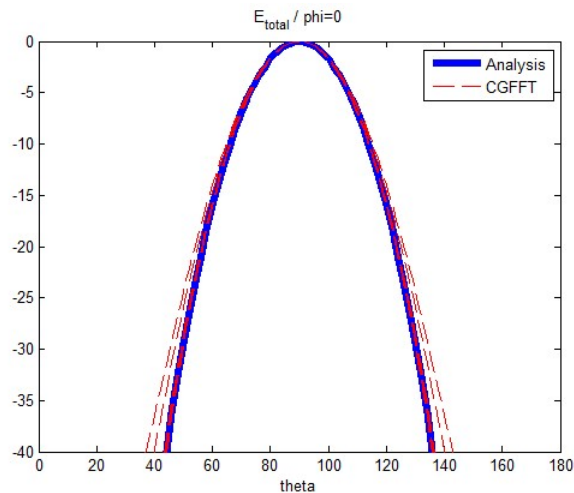


Fig. 8.23. E_{total} when $\phi = 0^\circ$ (dB Scale) for all sizes of the measurement planes from 0.8λ by 0.8λ to 20λ by 20λ with 0.2λ separations in both directions.

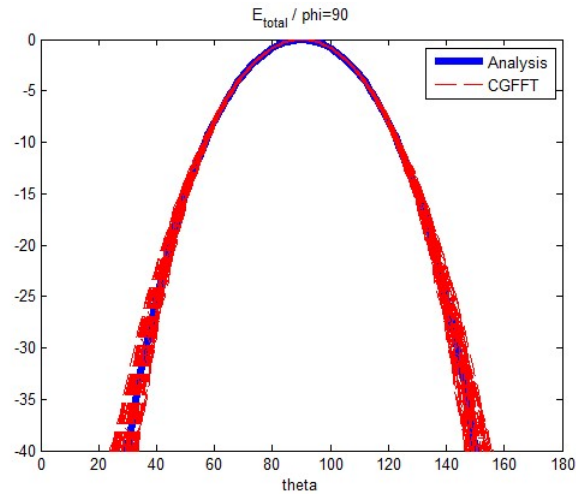


Fig. 8.24. E_{total} when $\phi = 90^\circ$ (dB Scale) for all sizes of the measurement planes from 0.8λ by 0.8λ to 20λ by 20λ with 0.2λ separations in both directions.

As we can see from Fig. 8.23 and Fig. 8.24 that all most all the dashed red lines are acute respect to the solid blue line. It's also necessary for us the analyze the relation between the relative error we mentioned above and the size of the measurement plane. The relations are shown in Fig. 8.25 and Fig. 8.26. After we observe the relative error plots of both cuts, all the errors are very small. We can easily find that they are all close to zero after the size of the measurement larger than or equal to 0.8λ . Notice that 0.5λ is also the size of the actual source plane of the antenna under test.

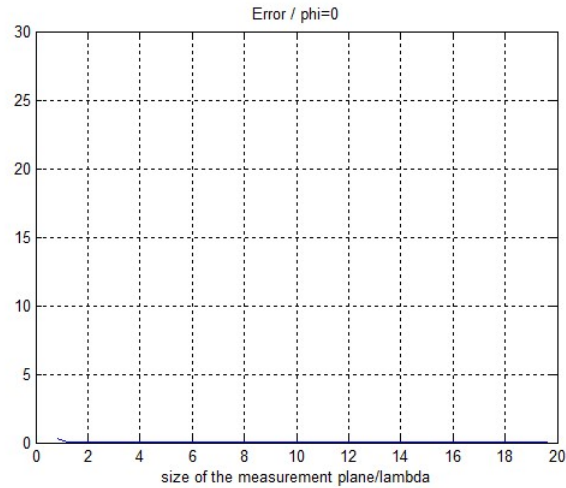


Fig. 8.25. Relative error at different sizes of measurement planes with 0.2λ separations in both directions ($\phi = 0^\circ$).

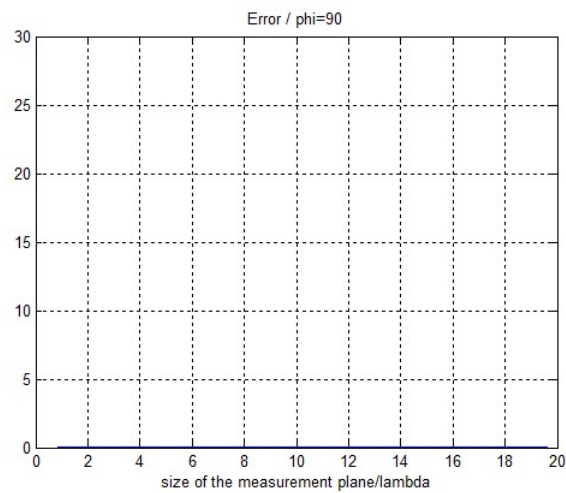


Fig. 8.26. Relative error at different sizes of measurement planes with 0.2λ separations in both directions ($\phi = 90^\circ$).

We can see that after the size of the measurement plane chosen to be larger than the size of the actual source plane of the antenna under test, our NF-FF approach provides acceptable results.

8.6 Example 8.4: Numerical results of choosing Yagi array to be the AUT.

For the final example, we deal with an antenna array under test. The array consists of 9 Yagi-Uda antennas to form a 3 by 3 antenna array as the antenna under test. Each element of the Yagi-Uda array has been described in example 8.3 and they are separated from each other by 2λ . The distance between the source plane and the measurement plane is 3λ . In this case the size of the actual source plane of the antenna under test is 4.5λ by 4λ .

We did 3 different groups of measurements:

Group 1: The number of the measurement dipoles starts from 4 by 4 and end up with 100 by 100. In order to keep the symmetry, we increase the number of dipoles on each side by a factor of 2 at a time, and we chose the separation between dipoles in both directions to be 0.2λ . Which means the measurement plane start from the dimensions of 0.8λ by 0.8λ to 20λ by 20λ . On the surface of the equivalent magnetic currents M_x and M_y are placed into same dimensions and discretized to enable the use of CGFFT.

Group 2: The number of the measurement dipoles starts from 4 by 4 and end up with 50 by 50. In order to keep the symmetry, we increase the number of dipoles on each side by a factor of 2 at a time, and we chose the separation between dipoles in both directions to be 0.4λ . Which means the measurement plane start from the dimensions of 1.6λ by 1.6λ to 20λ by 20λ . On the surface of the equivalent magnetic currents M_x and M_y are placed into same dimensions and discretized to enable the use of CGFFT.

Group 3: The number of the measurement dipoles starts from 4 by 4 and end up with 40 by 40. In order to keep the symmetry, we increase the number of dipoles on each side by a factor of 2 at a time, and we chose the separation between dipoles in both directions to be 0.5λ . Which means the measurement plane start from the dimensions of 2λ by 2λ to 20λ by 20λ . On the surface of the equivalent magnetic currents M_x and M_y are placed into same dimensions and discretized to enable the use of CGFFT.

Fig. 8.27. shows the 24 by 24 x-directed probe array with 0.2λ separations in both directions structure as an example. Fig. 8.28. shows the side view of the structure by using the 24 by 24 x-directed probe array with 0.2λ separations in both directions as an example.

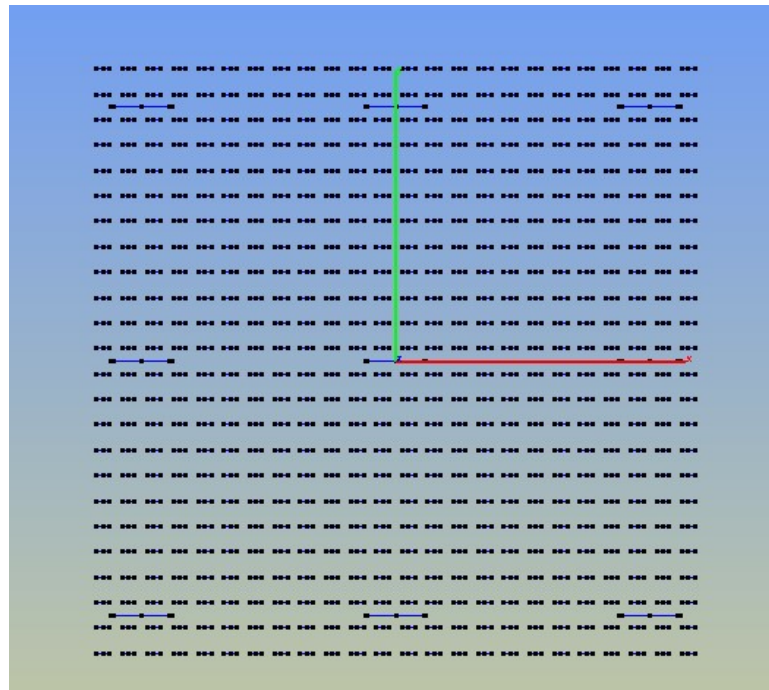


Fig. 8.27. 24 by 24 x-directed probe array with 0.2λ separations in both directions.

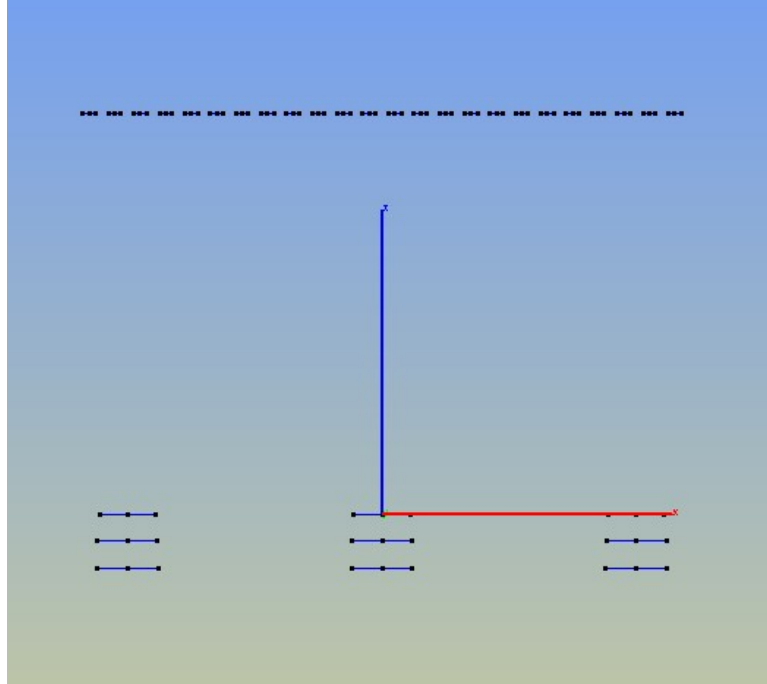


Fig. 8.28. 24 by 24 x-directed probe array with 0.2λ separations in both directions (side view).

The simulated results for measurement group 1 where all the sizes of the measurement planes are from 0.8λ by 0.8λ to 20λ by 20λ with 0.2λ separations in both directions which we mentioned above and the analytic results for the far fields are shown in Fig. 8.29 and Fig. 8.30 as an example. Where Fig. 8.29 shows the normalized absolute value of the electric far field for $\varphi = 0^\circ$ in the dB scale. Fig. 8.30 shows the normalized absolute value of the electric far field for $\varphi = 90^\circ$ in the dB scale. Theta here is defined as the angle from x axis to z axis and phi is the angle from the x axis to the y axis. This implies, phi equals 0° cut is the x-z plane and phi equals 90° is the y-z plane. The solid blue lines show the analytic results obtained using HOBBIES, dashed red lines show the results obtained using different sizes of square dipole probe array measurement.

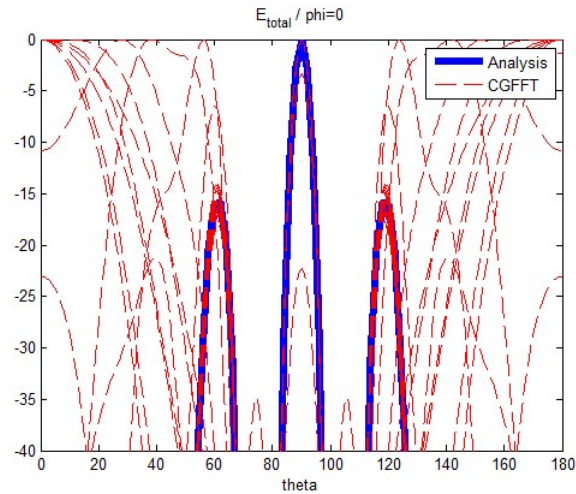


Fig. 8.29. E_{total} when $\phi = 0^\circ$ (dB Scale) for all sizes of the measurement planes from 0.8λ by 0.8λ to 20λ by 20λ with 0.2λ separations in both directions.

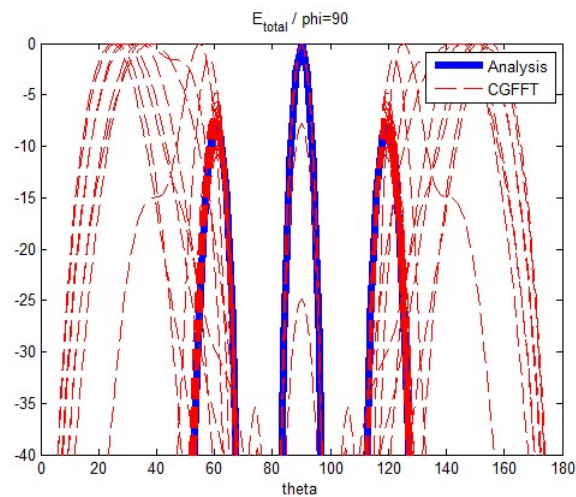


Fig. 8.30. E_{total} when $\phi = 90^\circ$ (dB Scale) for all sizes of the measurement planes from 0.8λ by 0.8λ to 20λ by 20λ with 0.2λ separations in both directions.

As we can see from Fig. 8.29 and Fig. 8.30 that most of the dashed red lines are acute respect to the solid blue line, and some portion of the dashed red lines are inaccurate. It's

necessary for us to analyze the relation between the relative error we mentioned above and the size of the measurement plane. The relations are shown in Fig. 8.31 and Fig. 8.32.

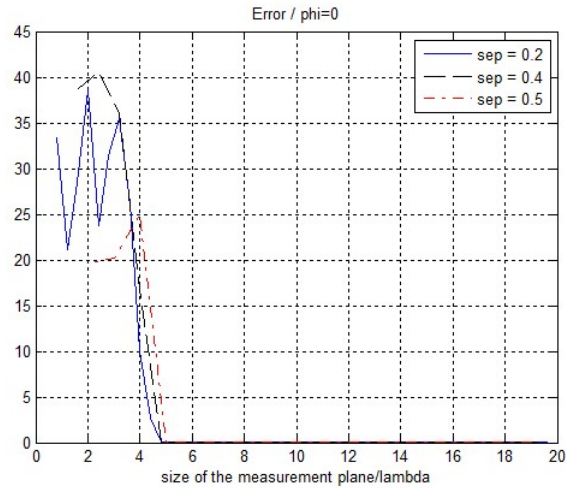


Fig. 8.31. Relative error at different sizes of measurement planes with 0.2λ , 0.4λ , 0.5λ separations in both directions ($\phi = 0^\circ$).

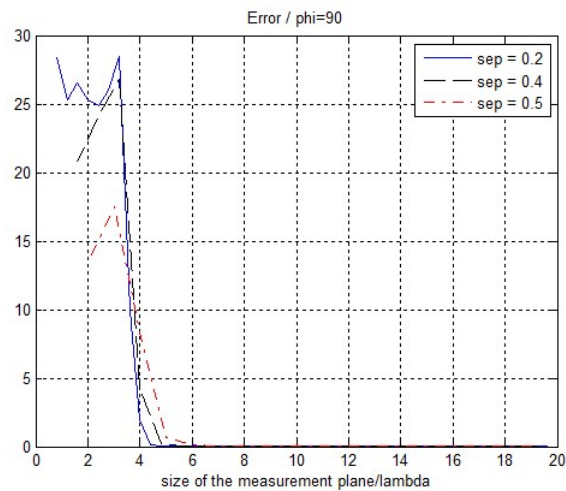


Fig. 8.32. Relative error at different sizes of measurement planes with 0.2λ , 0.4λ , 0.5λ separations in both directions ($\phi = 90^\circ$).

After we observe the relative error plots of both cuts, we can easily find that it goes down close to zero after the size of the measurement larger than 5λ . The remarkable point is that the relative error goes down close to zero for all the 3 groups of measurements with different separations (0.2λ , 0.4λ , 0.5λ) at about the same size of measurement plane. Notice that 5λ is also about the size of the actual source plane of the antenna under test. Also, the far field results obtained from the sizes of measurement planes with 0.2λ separations in both directions which are larger than 5λ are as shown in Fig. 8.33 and Fig. 8.34. The far field results obtained from the sizes of measurement planes with 0.4λ separations in both directions which are larger than 4.8λ are as shown in Fig. 8.35 and Fig. 8.36. The far field results obtained from the sizes of measurement planes with 0.5λ separations in both directions which are larger than 5λ are as shown in Fig. 8.37 and Fig. 8.38. We can see that all the inaccurate red dashed lines disappear and only the accurate ones left.

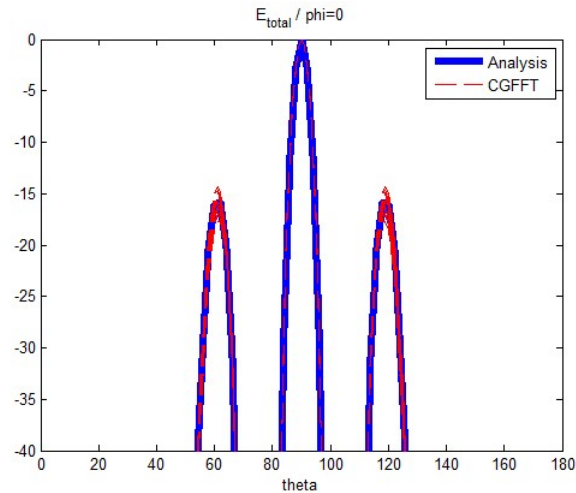


Fig. 8.33. E_{total} when $\phi = 0^\circ$ (dB Scale) for all sizes of the measurement planes from 5λ by 5λ to 20λ by 20λ with 0.2λ separations in both directions.

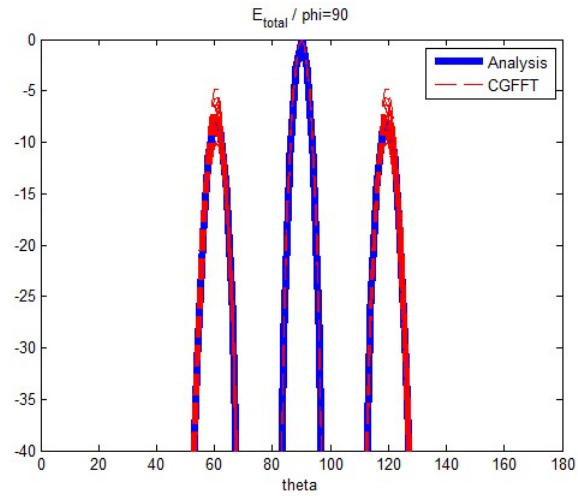


Fig. 8.34. E_{total} when $\phi = 90^\circ$ (dB Scale) for all sizes of the measurement planes from 5λ by 5λ to 20λ by 20λ with 0.2λ separations in both directions.

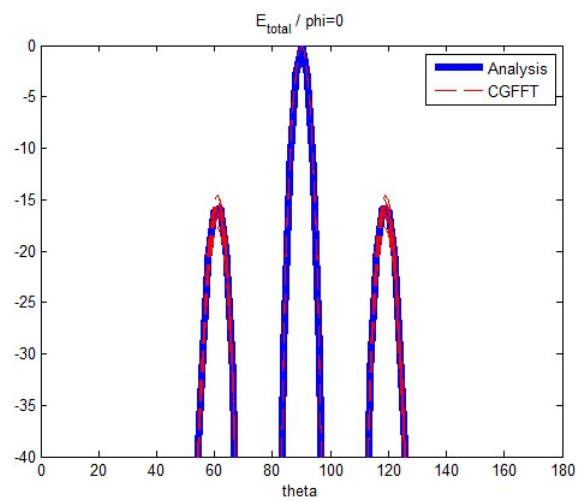


Fig. 8.35. E_{total} when $\phi = 0^\circ$ (dB Scale) for all sizes of the measurement planes from 4.8λ by 4.8λ to 20λ by 20λ with 0.4λ separations in both directions.

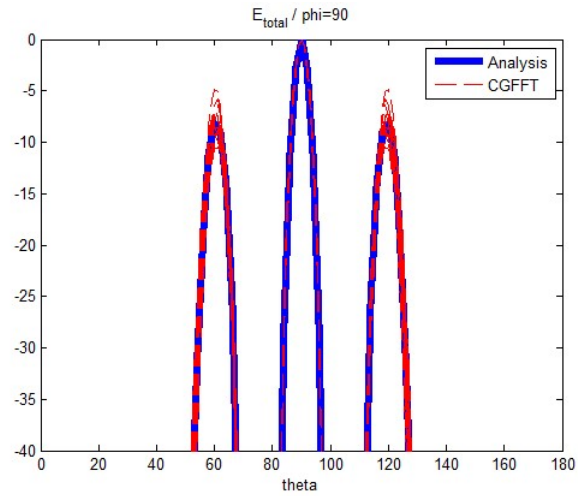


Fig. 8.36. E_{total} when $\phi = 90^\circ$ (dB Scale) for all sizes of the measurement planes from 4.8λ by 4.8λ to 20λ by 20λ with 0.4λ separations in both directions.

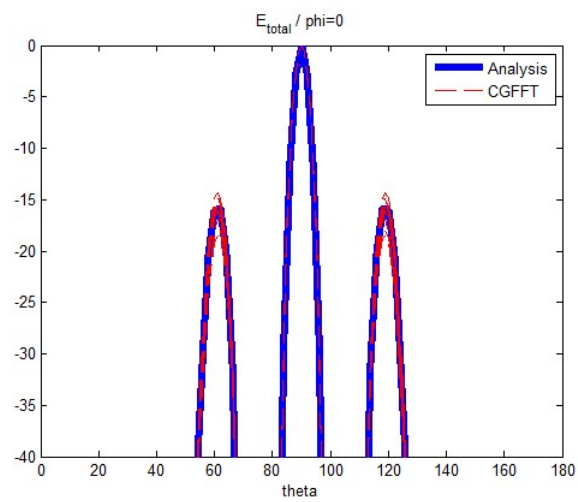


Fig. 8.37. E_{total} when $\phi = 0^\circ$ (dB Scale) for all sizes of the measurement planes from 5λ by 5λ to 20λ by 20λ with 0.5λ separations in both directions.

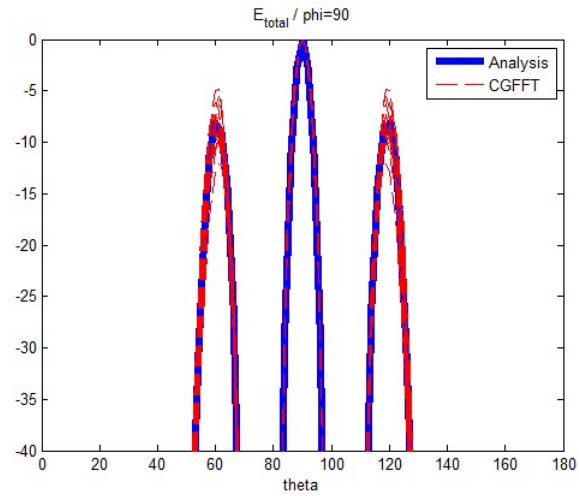


Fig. 8.38. E_{total} when $\phi = 90^\circ$ (dB Scale) for all sizes of the measurement planes from 5λ by 5λ to 20λ by 20λ with 0.5λ separations in both directions.

We can see that after the size of the measurement plane chosen to be larger than the size of the actual source plane of the antenna under test, our NF-FF approach provides acceptable results.

9 A FAST AND EFFICIENT METHODOLOGY FOR DETERMINING THE FAR FIELD PATTERNS OF AN ANTENNA ALONG PRINCIPAL PLANES USING A PROBE ARRAY

9.1 Objective and Unique Features

The objective of this chapter is to illustrate that using a rectangular planar dipole probe array to sample the near field of an AUT can be used to calculate the far field principal plane patterns efficiently. The solution methodology with measurement data over certain planar cuts not covering the entire equivalent planar surface as shown in Fig. 9.1 and Fig. 9.2. Performance of a linearly polarized antenna is often described in terms of its principal E-plane and H-plane patterns. If that is the goal, then we want to explore this possibility of measuring the near field over a sector and then using that to obtain the far field pattern along principal planes with engineering accuracy. As presented earlier we would like to use a dipole planar probe array to accomplish this goal and so precision mechanical measurement gadgets will not be required and thus minimizing the cost and speeding up the measurement process. The unique feature of this procedure is that it is not necessary to cover the entire frontal surface of the AUT. Also, compensation of mutual coupling is not required for the measurements between the elements of the dipole array. This provides a fast and efficient methodology to determine the E-plane and H-plane far field patterns of the antenna using partial data. Conventional classical Fourier based methods cannot

provide any meaningful results under the present conditions. The current methodology requires placing the probe array over two rectangular planes near the original antenna source individually and measuring the two components of the electric fields and employing the Method of Moments approach to solve for the equivalent magnetic currents on some fictitious planes located in front of the AUT. For this proposed methodology there is no need to satisfy the Nyquist sampling criteria in the measurement plane, and super resolution can be achieved in the solution of the equivalent magnetic current.

9.2 Implementation of the Methodology Over a Sector

A dipole array is used for the measurement plane which consist of 0.1λ length dipoles all terminated in 50Ω loads and separated from each other by 0.2λ to estimate the sampled electric fields at 0.2λ separation on the rectangular measurement planar surfaces. To carry out the measurements of the near field the following steps were conducted.

First, as shown in Fig. 9.1, we make all the dipoles in the array to be x-directed and obtain the value of $[V_{x1}]$ across the loads. Then, keep the size of the array to be the same and rotate each dipole by 90 degree to be y-directed and obtain the value of $[V_{y1}]$ across the loads. It is estimated that the voltages V obtained at the center of the dipoles is proportional to the electric field \bar{E} at that point. From that estimated near field data, the equivalent magnetic currents (M_{x1}, M_{y1}) on the source plane can be calculated. By using that partial information on the equivalent magnetic currents, we calculate the far field which is expected to provide the x-z cut.

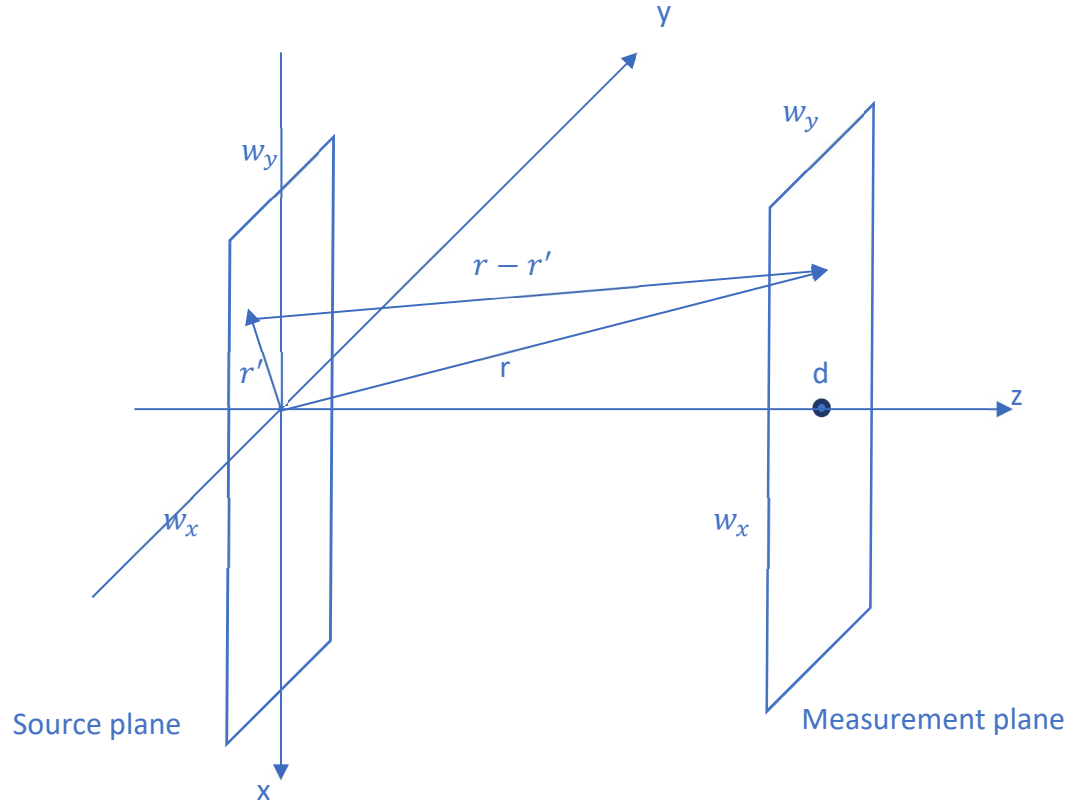


Fig. 9.1. Planar scanning for x-z plane.

Next, as shown in Fig. 9.2, we make all the dipoles in the array to be x-directed and obtain the value of $[V_{x2}]$ across the loads. Then, keep the size of the array to be the same and rotate each dipole by 90 degree to be y-directed and obtain the value of $[V_{y2}]$ across the loads. Again, it is estimated that the voltage V at the center of the dipole is proportional to the electric field \bar{E} at that point. The voltages induced at the center points of the dipoles provide an estimate for the sampled near field data. From that estimated near field data, the equivalent magnetic currents (M_{x2}, M_{y2}) on the source plane can be calculated. By using that equivalent magnetic currents, we calculate the far field which is expected to be accurate in the y-z cut.

These two sets of measurements are used to find the equivalent magnetic currents on the source plane. Using these limited number of observation points and a short region for the equivalent magnetic current the computed far field along some principal planes can be obtained as illustrated next.

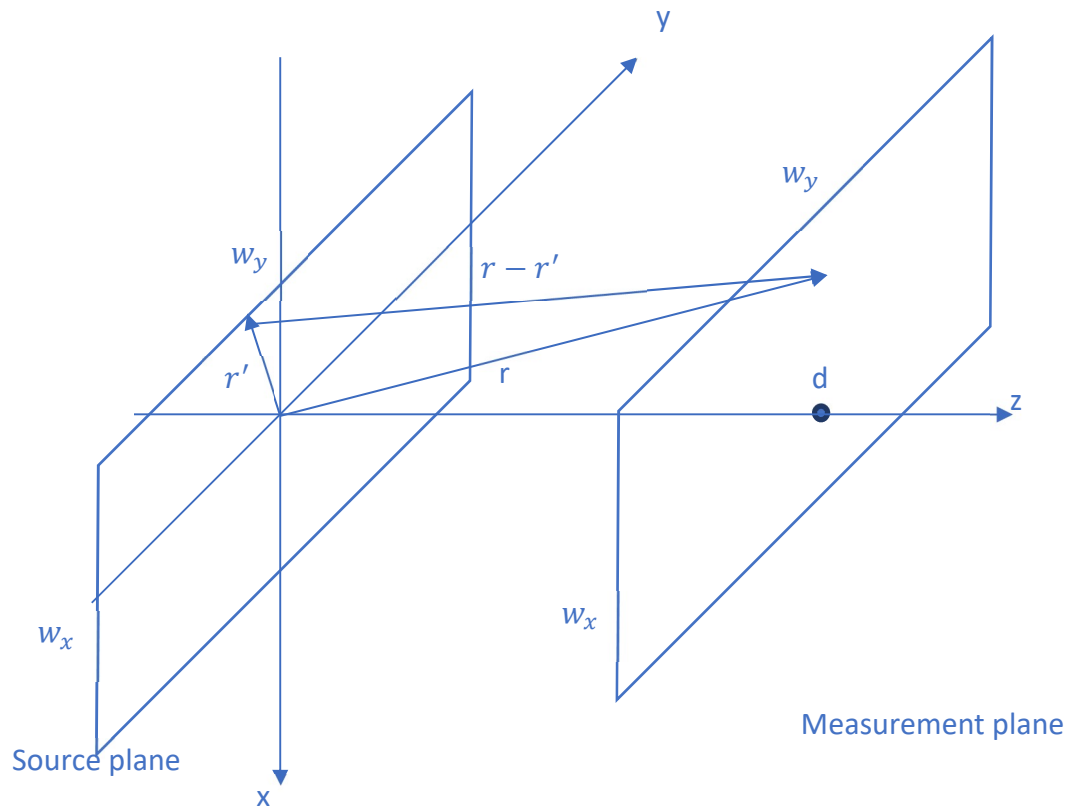


Fig. 9.2. Planar scanning for y-z plane.

The comparisons of the E-plane and the H-plane patterns are calculated using both the fictitious source and measurements over a planar slice of space covering a portion of the antenna under test. The assumed two principal source and the measurement planes are a slice of the planar space as described in the following examples.

9.3 Example 9.1: Numerical results of choosing Horn to be the AUT.

Consider a 2λ by 2λ pyramidal horn antenna under test whose principal plane patterns are desired in a quick way with engineering accuracy. To generate the patterns first measurements are made using a probe array and are illustrated by the following sequence of calculations.

Step 1: The probe array in this case consists of an array of Hertzian Dipoles of 0.1λ length and are all terminated by $50\ \Omega$ loads. The individual elements in the array are separated from center to center along x-direction by 0.2λ and also along the y-direction by the same amount. So, the spacing between the two linear probe arrays in the y-direction is 0.2λ . The induced voltages in the terminated loads are used to estimate the sampled electric fields on a planar slice of the principal measurement planes formed by the probe array.

First, we make all the dipoles to be x-directed and choose the dimensions of the measurement array to be 2.7λ by 0.2λ , which means 28 dipoles (14×2 dipoles) in total are considered as placed in Fig. 9.3. The voltages across the dipoles are now measured to obtain the Matrix $[V_{x1}]$. They are now used to estimate the unknown magnetic currents on the source plane. The source plane is of the size 2.8λ by 0.4λ . It consists of 28 square patches of size 0.2λ each.

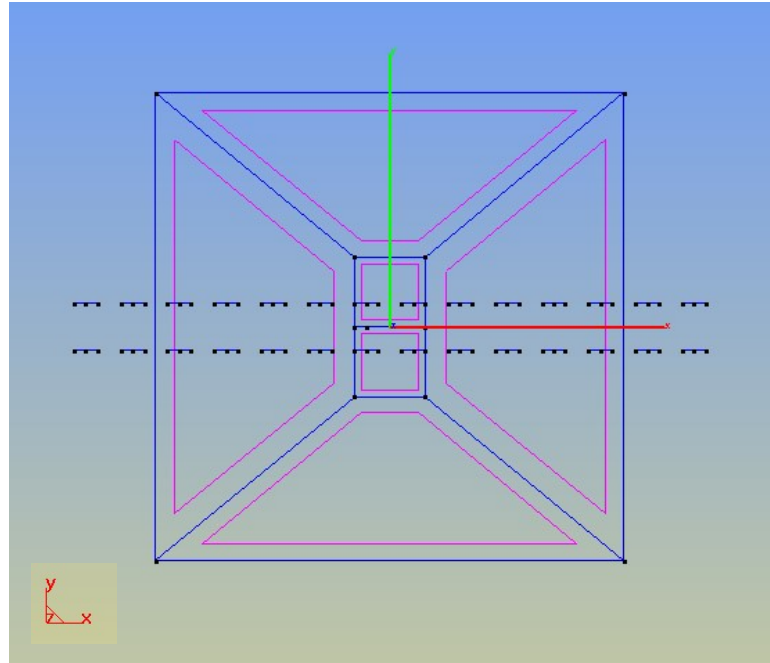


Fig. 9.3. x-directed rectangular probe array (step1).

Next, all the dipoles are considered to be y-directed. The measurement plane in this case is of size 2.6λ by 0.3λ to calculate the other component of the magnetic current placed on the same source plane as shown in Fig. 9.4, which implies that the measurements are carried out using 28 dipoles (14×2 dipoles) placed as shown in Fig. 9.4. The size of the source plane is the same as in the previous case. The measured voltages across the terminated loads of the dipoles are used to obtain the Matrix $[V_{y1}]$. The separation between the source plane and the measurement plane is 3λ as shown in Fig. 9.5.

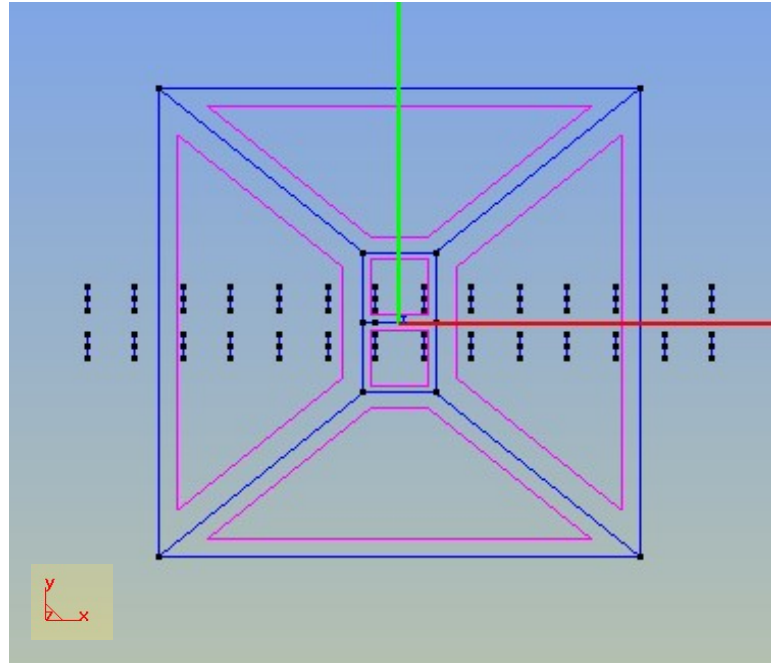


Fig. 9.4. *y*-directed rectangular probe array (step1).

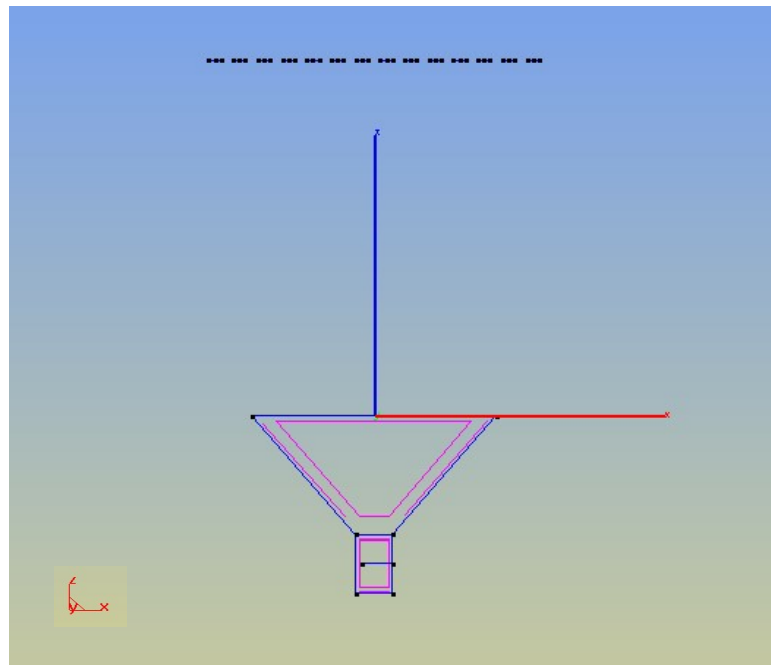


Fig. 9.5. *x*-directed probe array (side view of step1).

The CGFFT method is used to calculate the two components of the magnetic currents on the source plane of dimensions 2.8λ by 0.4λ . This yields two components of the magnetic currents M_{x1} and M_{y1} which consist of 14×2 current patches. The far field is now calculated in this principal plane using these two sets of magnetic currents. Fig. 9.6 provides the principal plane pattern for this case. The pattern is accurate from 60° to 120° . The classical near field to far field transformation will not provide any result for this set of measurements.

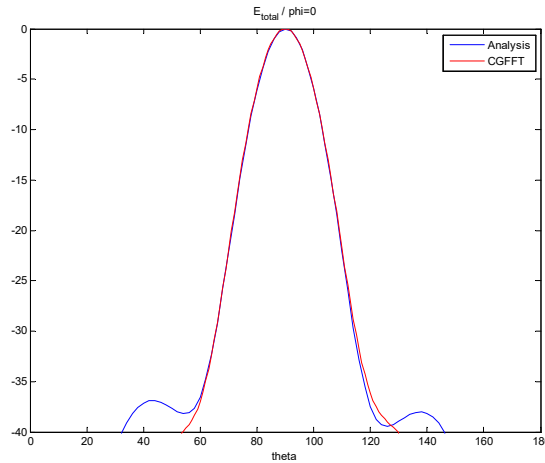


Fig. 9.6. E total when $\phi=0$ (dB Scale) as in step1.

Step 2: To obtain the pattern for the other cut, we place a rectangular dipole array with 0.1λ length Hertzian Dipole all terminated in 50Ω loads and separated from each other in both directions by 0.2λ to estimate the sampled electric fields on the measurement plane. So, the rectangular measurement plane is rotated by 90 degree when compared to that in Step 1, as shown in Fig. 9.7 and Fig. 9.8.

First, we make all the dipoles in the probe array to be x-directed and choose the dimensions of the array to be 0.3λ by 2.6λ , which means 28 dipoles (2×14 dipoles) in

total as shown in Fig. 9.7. The voltages across the dipoles are measured to obtain the Matrix $[V_{x2}]$.

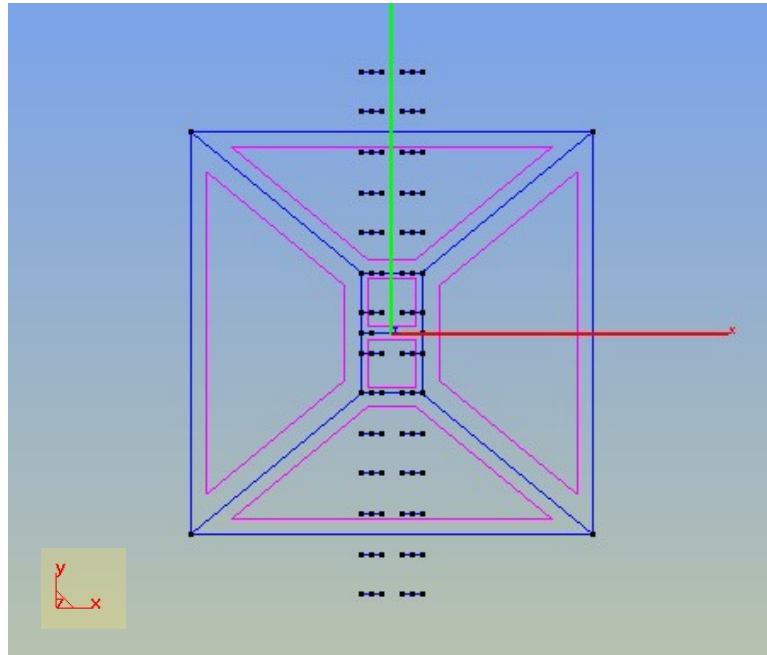


Fig. 9.7. x-directed rectangular probe array (step2).

Next, we make all the dipoles to be y-directed as shown in Fig. 9.8. The dipole array is now of size 0.2λ by 2.7λ as shown. The source plane in both cases are of the same size of 0.4λ by 2.8λ . Measure the voltages across the 28 dipoles to obtain the matrix $[V_{y2}]$ estimating the near fields from the antenna under test and projected on the probe array.

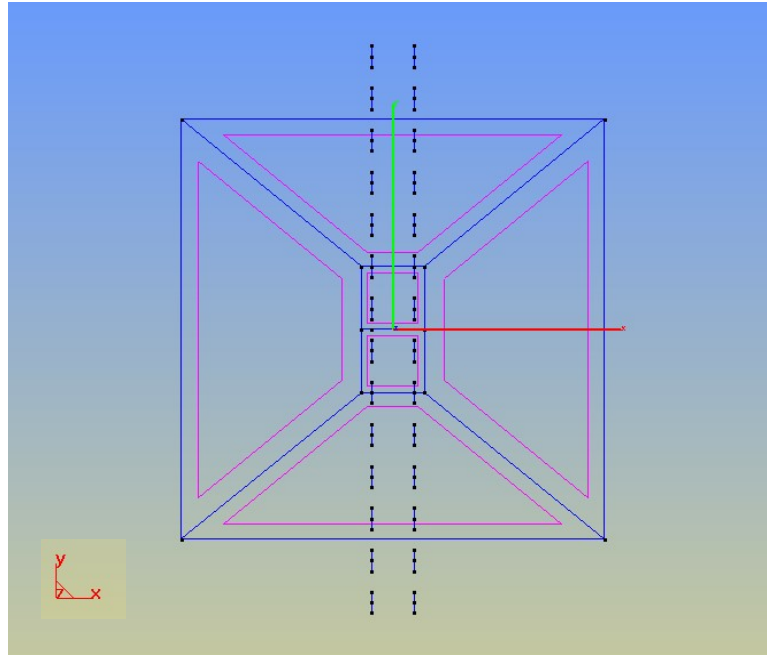


Fig. 9.8. y-directed rectangular probe array (step2).

The equivalent magnetic current plane is chosen to be of the same dimensions and discretized to enable the use of CGFFT. The equivalent magnetic currents M_{x2} and M_{y2} are first calculated and then they are used to obtain the far field pattern as shown in Fig 11. It is seen that by placing the equivalent magnetic current over a planar sector covering only a portion of the plane across which the far field pattern is to be computed can provide results of engineering accuracy. The other interesting point is that the mutual coupling between the measurement dipoles is not taken into account in the entire procedure and yet the predictions are quite accurate.

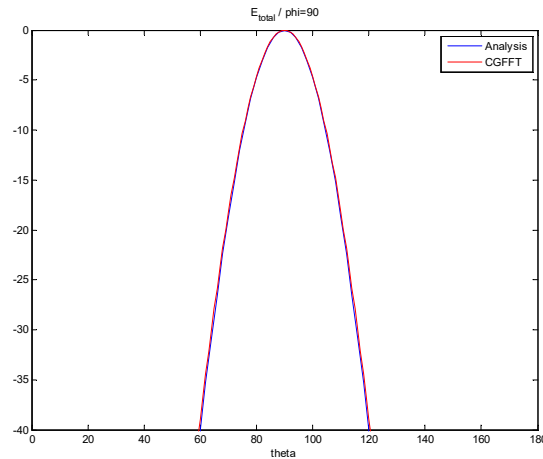


Fig. 9.9. E total when phi=90 (dB Scale) of step 2.

The simulated results for the two steps we mentioned above, and the analytic results are shown in Fig. 9.6 and Fig. 9.9 for the two principal plane cuts. Fig. 9.6 shows the normalized absolute value of the electric far field for $\varphi = 0^\circ$ in the dB scale for step 1. Fig. 9.9 shows the normalized absolute value of the electric far field for $\varphi = 90^\circ$ in dB scale of step 2. Theta is defined as the angle from x axis to z axis and phi is the angle from the x axis to the y axis. This implies, phi equals 0° cut is the x-z plane (E-plane) and phi equals 90° is the y-z plane (H-plane). Theta equals 0° means +x direction and theta equals 180° means -x direction. The blue lines show the analytic results obtained by using HOBBIES, red lines show the rectangular probe array simulated results using the probe array data as the starting point over a sector. This presents a possibility of obtaining a quick solution of engineering accuracy in a short time for the two principal planes of the antenna under test.

9.4 Example 9.2: Numerical results of choosing Horn array to be the AUT.

For the next example, the antenna under test is made more complicated. We choose 16, 1.5λ by 2λ pyramidal horn antennas to form a 4 by 4 array as the antenna under test. Each horn antenna is separated from each other by 3λ .

We follow the two steps as outlined before.

Step 1: Put a rectangular dipole array of 0.1λ length Hertzian dipoles all terminated in $50\ \Omega$ loads and separated from each other in both directions by 0.2λ to estimate the sampled electric fields at 0.2λ separation on the rectangular measurement plane.

First, make all the measurement dipoles in the probe array to be x-directed and choose the dimensions of the array to be 9.9λ by 1.4λ , which means 400 dipoles (50×8 dipoles) in total are considered as shown in Fig. 9.10. Measure the voltages across the dipoles to obtain the Matrix $[V_{x1}]$.

Secondly, make all the dipoles to be y-directed and chose the dimensions of the array to be 9.8λ by 1.5λ , which means 400 dipoles (50×8 dipoles) in total as shown in Fig. 9.11. Measure the voltages across the dipoles to obtain the Matrix $[V_{y1}]$. The distance between the source plane and the measurement plane is shown in Fig. 9.12.

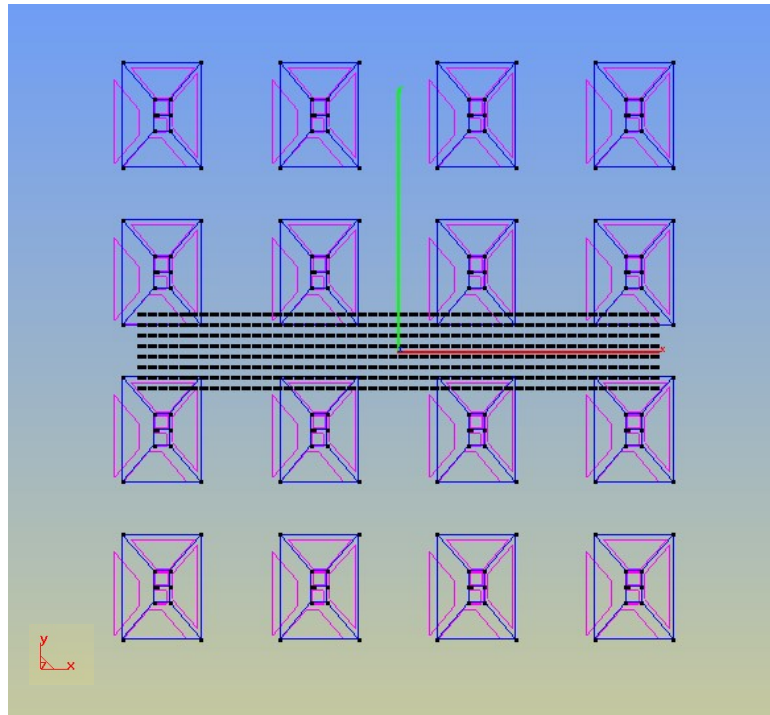


Fig. 9.10. x-directed rectangular probe array (step1).

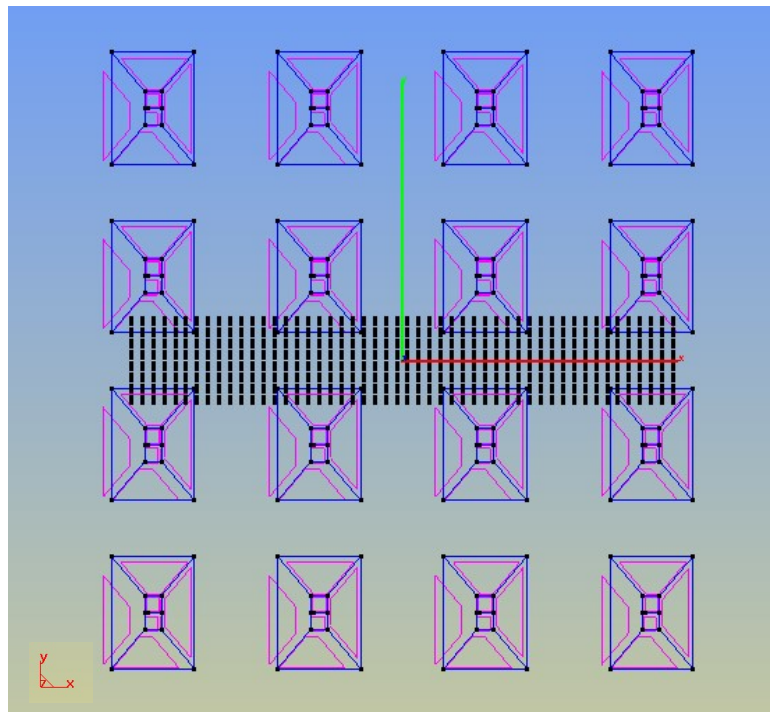


Fig. 9.11. y-directed rectangular probe array (step1).

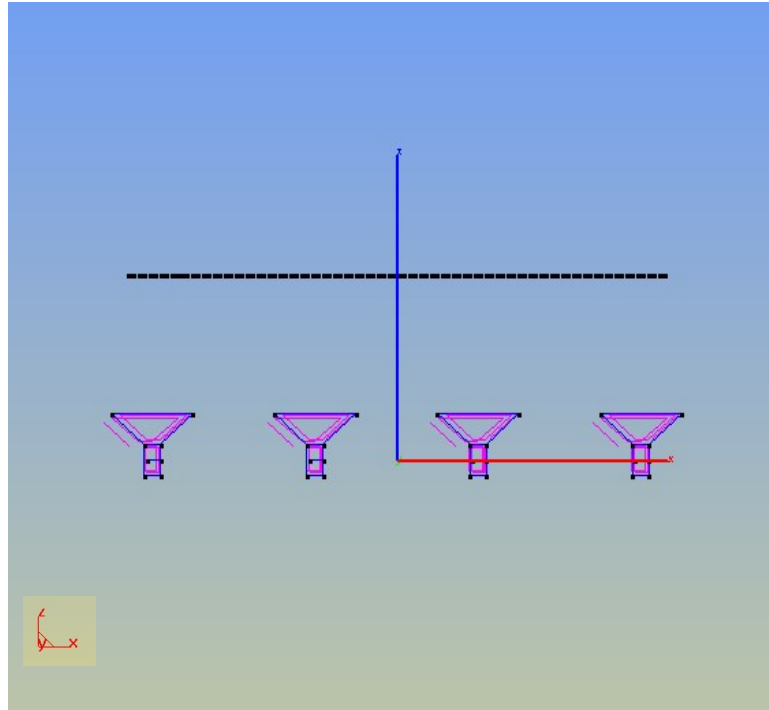


Fig. 9.12. x-directed probe array (side view of step1).

The equivalent magnetic current plane is chosen to be 10λ by 1.6λ and use the CGFFT described earlier to find the magnetic currents on the source plane for this set of measurement data in an efficient and accurate way. This implies that the equivalent magnetic currents M_{x1} and M_{y1} are placed into 50×8 current patches. From the computed equivalent magnetic currents M_{x1} and M_{y1} the far field pattern for the principal plane is shown in Fig. 9.13. Even though all the peaks are located at the same position the peak value is off.

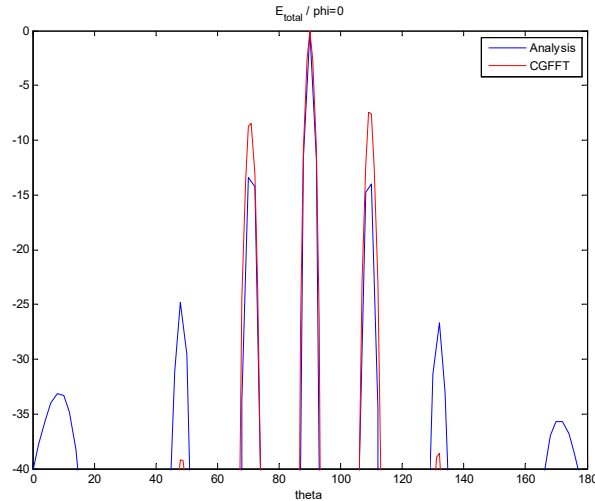


Fig. 9.13. E_{total} when $\phi=0$ (dB Scale) of step1.

Step 2: Next, put a rectangular dipole array with 0.1λ length Hertzian Dipole all terminated in 50Ω loads and separated from each other in both directions by 0.2λ to estimate the sampled electric fields at 0.2λ separation on the rectangular measurement plane. This time, the rectangular measurement plane is rotated by 90 degree compared to that in Step 1, as shown in Fig. 9.14 and Fig. 9.15. The distance between the source plane and the measurement plane are all chosen to be 3λ , as shown in Fig. 9.12.

First, make all the dipoles to be x-directed and choose the dimensions of the array to be 1.5λ by 9.8λ , which means 400 dipoles (8×50 dipoles) in total as shown in Fig. 9.14. Measure the voltages across the dipoles to obtain the Matrix $[V_{x2}]$.

Secondly, make all the dipoles to be y-directed and choose the same dimensions of the array to be 1.4λ by 9.9λ , which means 400 dipoles (8×50 dipoles) in total as shown in Fig. 9.15. Measure the voltages across the dipoles to obtain the Matrix $[V_{y2}]$.

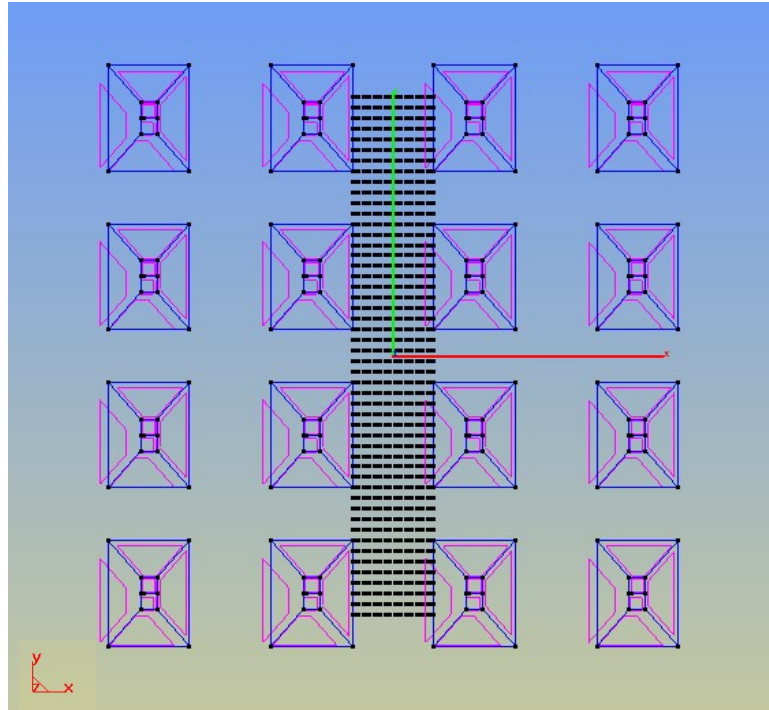


Fig. 9.14. *x*-directed rectangular probe array (step2).

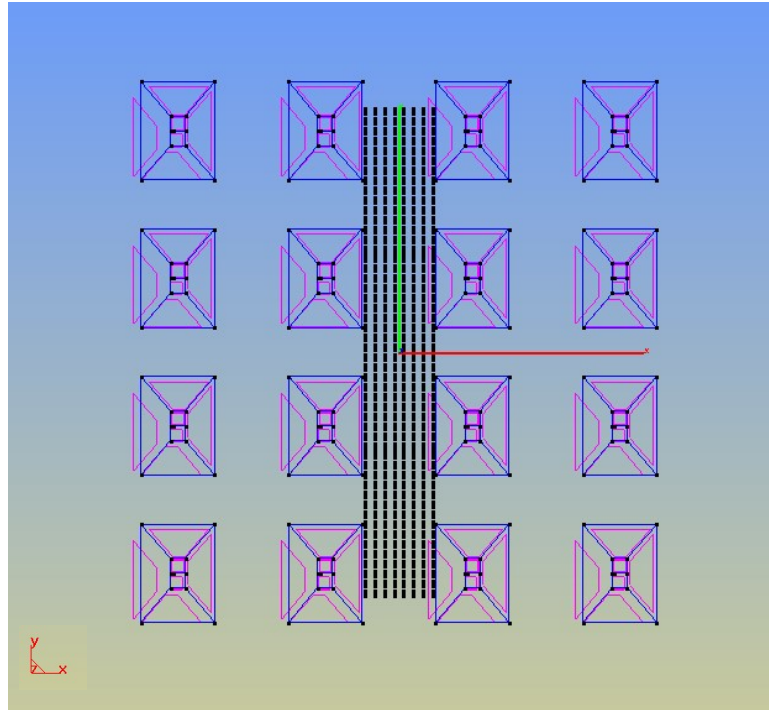


Fig. 9.15. *y*-directed rectangular probe array (step2).

The equivalent magnetic current plane is chosen to be 1.6λ by 10λ consisting of 400 square patches of dimensions 0.2λ . The CGFFT method is now used to compute the equivalent magnetic currents M_{x2} and M_{y2} that are placed into 8×50 current patches. From the equivalent magnetic currents M_{x2} and M_{y2} the far field pattern in the other principal plane is calculated as shown in Fig. 9.16.

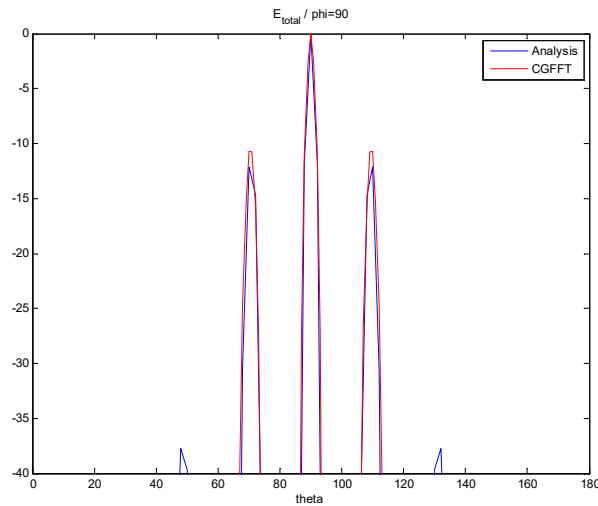


Fig. 9.16. E total when $\phi=90$ (dB Scale) of step2.

The simulated results for the two steps we mentioned above, and the analytic results are shown in Fig. 9.13 and Fig. 9.16. Fig. 9.13 shows the normalized absolute value of the electric far field for $\phi = 0^\circ$ in the dB scale of step1. Fig. 9.16 shows the normalized absolute value of the electric far field for $\phi = 90^\circ$ in dB scale of step2. The blue lines show the analytic results obtained by using HOBBIES, red lines show the rectangular probe array measurement results.

9.5 Example 9.3: Numerical results of choosing Yagi antenna to be the AUT.

For the third example a single three element Yagi-Uda antenna is selected as the antenna under test to illustrate the results obtained using this methodology. The three-element Yagi-Uda antenna is shown in Fig. 9.17 which consist of a driven element of length $L = 0.47 \lambda$, a reflector of length of 0.482λ , and a director of length 0.442λ . They are all spaced 0.2λ apart. The radius of the wire structure for all cases is 0.00425λ .

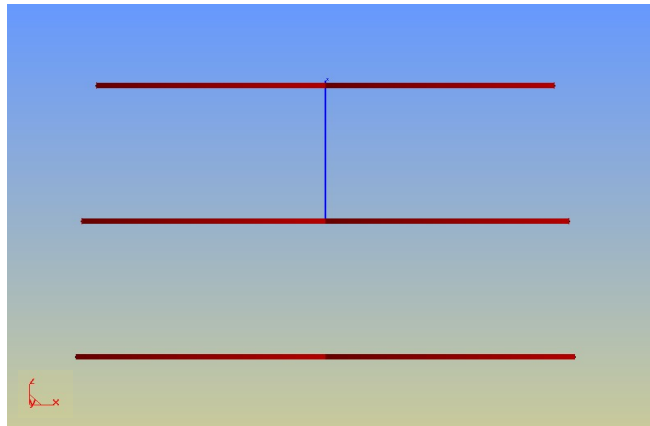


Fig. 9.17. A three-element Yagi-Uda antenna.

The measurement methodology for this Yagi-Uda antenna is quite similar to the measurement system used for the horn antenna as described in Example 9.1.

Step 1: Put a rectangular dipole array with 0.1λ length Hertzian Dipole all terminated in 50Ω loads and separated from each other in both directions by 0.2λ to estimate the sampled electric fields at 0.2λ separation on the rectangular measurement plane.

First, make all the dipoles to be x-directed and chose the dimensions of the array to be 1.7λ by 0.4λ , which translates to 27 dipoles (9×3 dipoles) in total. Measure the voltages across the dipoles to obtain the Matrix $[V_{x1}]$.

Secondly, make all the dipoles to be y-directed and chose the same dimensions of the array to be 1.6λ by 0.5λ , which means 27 dipoles (9×3 dipoles) in total. Measure the voltages across the dipoles to obtain the Matrix $[V_{y1}]$.

The source plane over which the magnetic current is employed is of size 1.8λ by 0.6λ implying that it contains 27 square patches over which the magnetic current is applied resulting in M_{x1} and M_{y1} of size 9×3 current patches. The equivalent magnetic current is now solved for using CGFFT. The equivalent magnetic currents M_{x1} and M_{y1} are used to obtain the far field pattern as shown in Fig. 9.18.

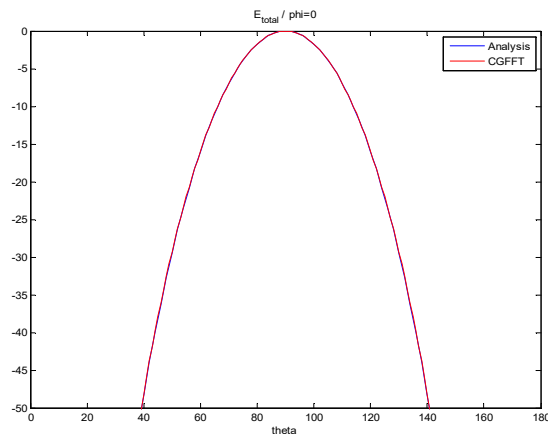


Fig. 9.18. E total when phi=0 (dB Scale) of step1.

Step 2: Now, orient the rectangular dipole array with 0.1λ length Hertzian Dipole all terminated in 50Ω loads and separated from each other in both directions by 0.2λ to

estimate the sampled electric fields at 0.2λ separation on the rectangular measurement plane. This time, the rectangular measurement plane is rotated by 90 degree compared to that in Step 1.

First, make all the dipoles to be x-directed and chose the dimensions of the array to be 0.5λ by 1.6λ , which means 27 dipoles (3 x 9 dipoles) in total. Measure the voltages across the dipoles to obtain the Matrix $[V_{x2}]$.

Secondly, make all the dipoles to be y-directed and chose the same dimensions of the array to be 0.4λ by 1.7λ , which means 27 dipoles (3 x 9 dipoles) in total. Measure the voltages across the dipoles to obtain the Matrix $[V_{y2}]$.

The equivalent magnetic current plane on the source plane of 0.6λ by 1.8λ containing 27 square current patches are used and the magnetic current on them is solved using the CGFFT method for M_{x2} and M_{y2} . Using the equivalent magnetic currents M_{x2} and M_{y2} the far field pattern is shown in Fig. 9.19.

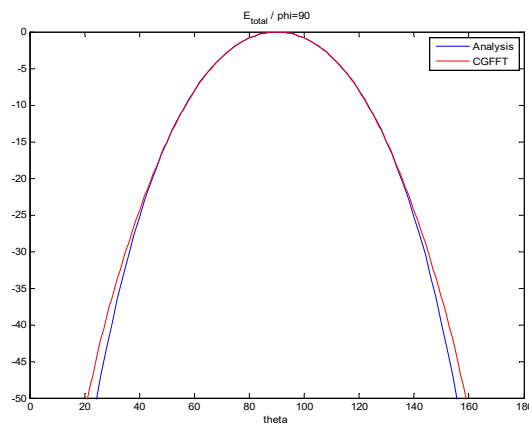


Fig. 9.19. E total when $\phi=90$ (dB Scale) of step 2.

The simulated results for the two steps we mentioned above, and the analytic results are shown in Fig. 9.18 and Fig. 9.19. Fig. 9.18 shows the normalized absolute value of the electric far field for $\varphi = 0^\circ$ in the dB scale of step 1. Fig. 9.19 shows the normalized absolute value of the electric far field for $\varphi = 90^\circ$ in dB scale of step 2. The blue lines show the analytic results obtained by using HOBBIES, red lines show the rectangular probe array measurement results.

9.6 Example 9.4: Numerical results of choosing Yagi Array to be the AUT.

For the final example, we deal with a 3 by 3 array of Yagi-Uda antennas. Each element of the Yagi-Uda array has been described in example 9.3 and they are separated from each other by 2λ .

Step 1: Put a rectangular dipole array with 0.1λ length Hertzian Dipole all terminated in $50\ \Omega$ loads and separated from each other in both directions by 0.2λ to estimate the sampled electric fields at 0.2λ separation on the rectangular measurement plane.

First, make all the dipoles to be x-directed and chose the dimensions of the array to be 4.9λ by 0.4λ , which means 75 dipoles (25 x 3 dipoles) in total as shown in Fig. 9.20. Measure the voltages across the dipoles to obtain the Matrix $[V_{x1}]$.

Secondly, make all the dipoles to be y-directed and chose the probe array to be of size 4.8λ by 0.5λ , which means 75 dipoles (25 x 3 dipoles) in total as shown in Fig. 9.21. Measure the voltages across the dipoles to obtain the Matrix $[V_{y1}]$. The measurement plane is 3λ away from the source plan as shown in Fig. 9.22.

The equivalent magnetic current on the selected source plane is of size 5λ by 0.6λ consisting of 75 square patches. The CGFFT method is then used to solve for the currents M_{x1} and M_{y1} of size 25×3 current patches. These equivalent magnetic currents M_{x1} and M_{y1} are used to compute the far field pattern as shown in Fig. 9.23.

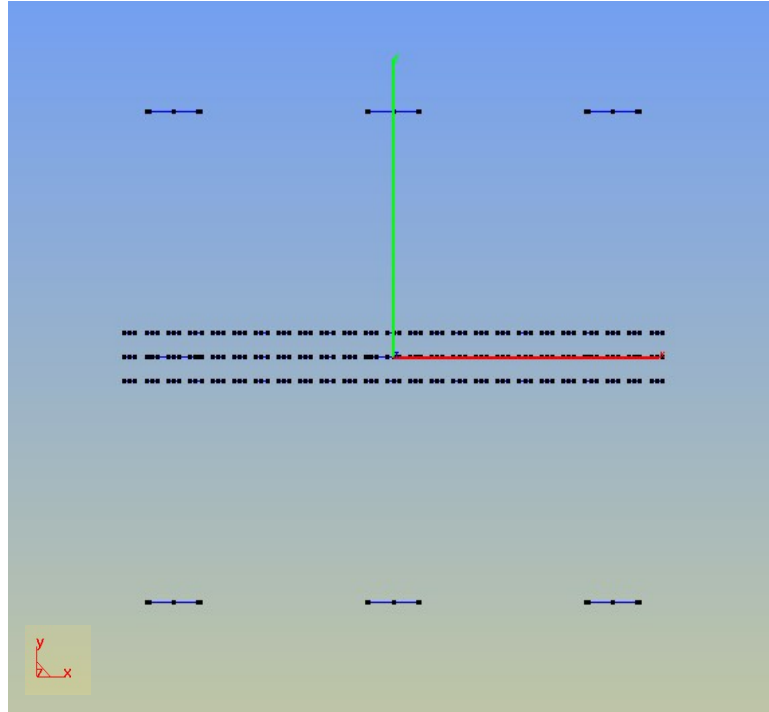


Fig. 9.20. x-directed rectangular probe array (step1).

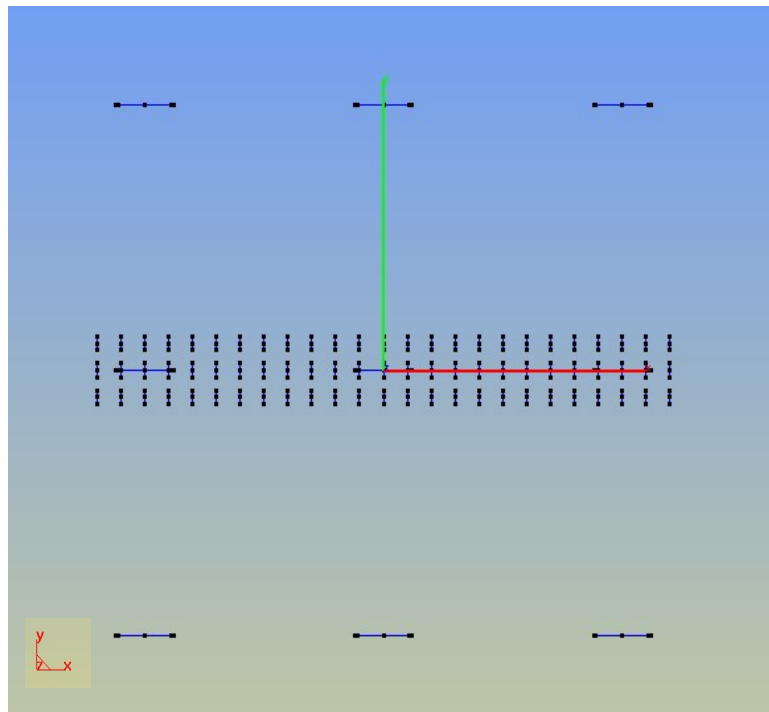


Fig. 9.21. y-directed rectangular probe array (step1).

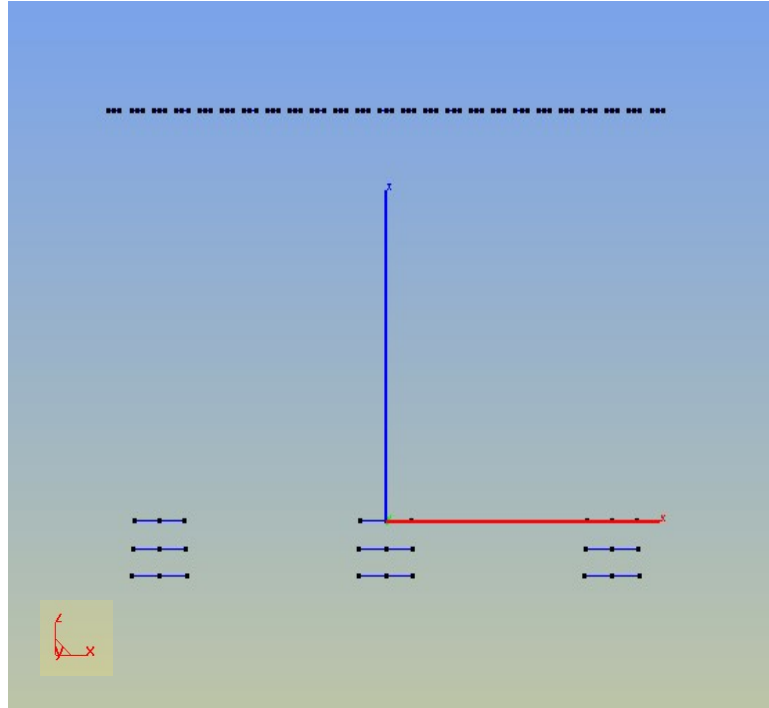


Fig. 9.22. *x*-directed probe array (side view of step1).

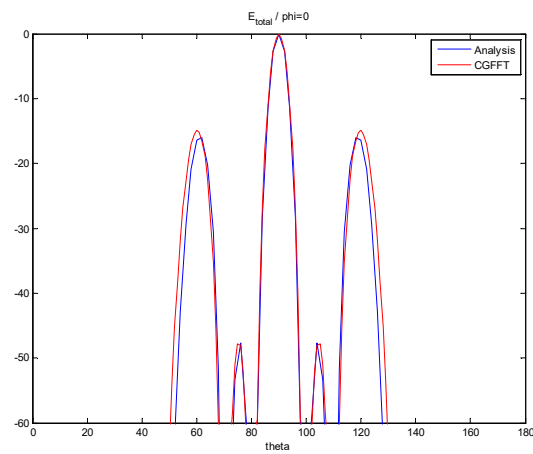


Fig. 9.23. *E* total when $\phi=0$ (dB Scale) of step 1.

Step 2: Now place a rectangular dipole array with 0.1λ length Hertzian Dipole all terminated in 50Ω loads and separated from each other in both directions by 0.2λ to estimate the sampled electric fields. This time, the rectangular measurement plane is rotated by 90 degree compared to that in Step 1, as shown in Fig. 9.24 and Fig. 9.25.

First, make all the dipoles to be x-directed and chose the dimensions of the array to be 0.5λ by 4.8λ , which means 75 dipoles (3×25 dipoles) in total as shown in Fig. 9.24. Measure the voltages across the dipoles to obtain the Matrix $[V_{x2}]$.

Secondly, make all the dipoles to be y-directed and chose the same dimensions of the array to be 0.4λ by 4.9λ , which means 75 dipoles (3×25 dipoles) in total as shown in Fig. 9.25. Measure the voltages across the dipoles to obtain the Matrix $[V_{y2}]$.

The equivalent magnetic current plane is chosen to be to be 0.6λ by 5λ . The CGFFT method is now used to calculate the equivalent magnetic currents M_{x2} and M_{y2} of size 3×25 current patches. The equivalent magnetic currents M_{x2} and M_{y2} are now used to calculate the far fields as shown in Fig. 9.26.

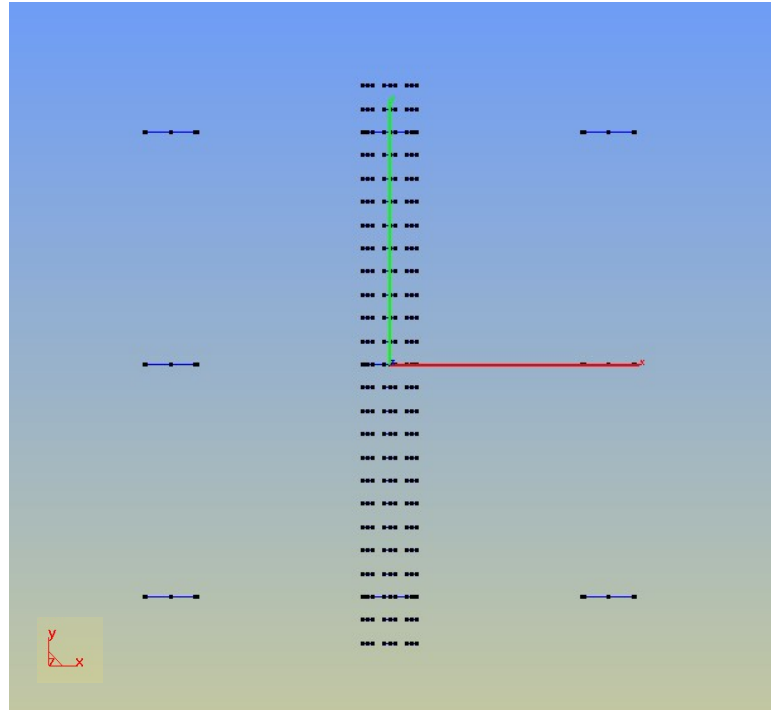


Fig. 9.24. *x-directed rectangular probe array (step2).*

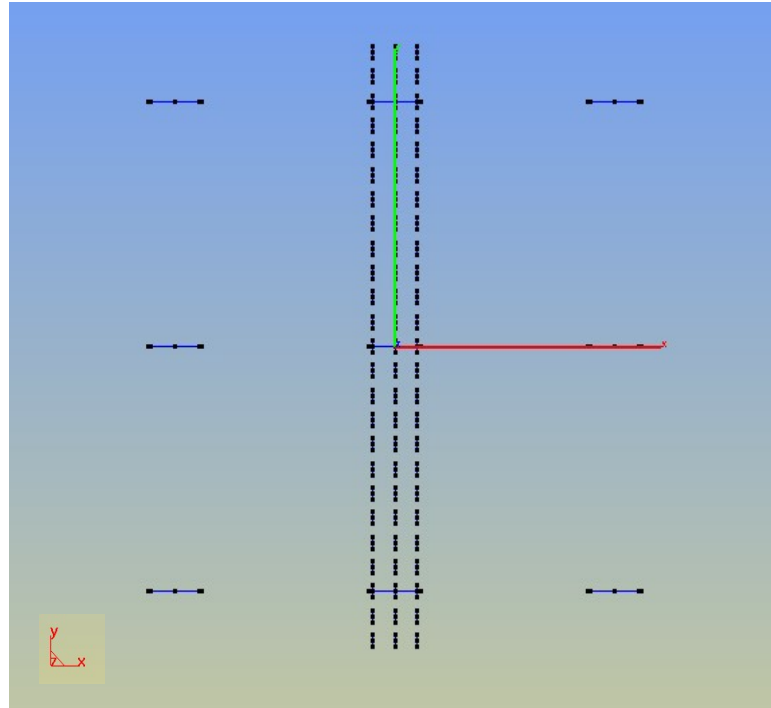


Fig. 9.25. *y-directed rectangular probe array (step2).*

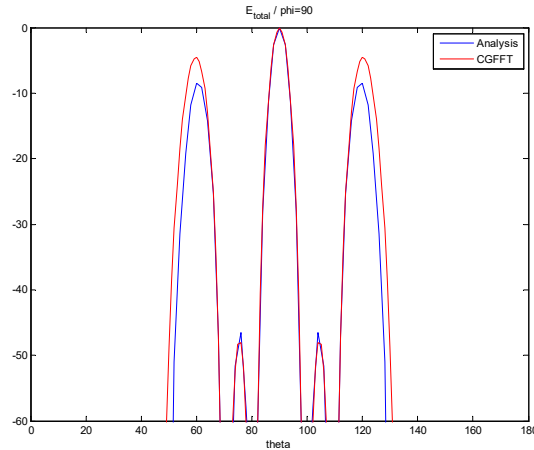


Fig. 9.26. E total when $\phi=90$ (dB Scale) of step 2.

The simulated results for the two steps we mentioned above, and the analytic results are shown in Fig. 9.23 and Fig. 9.26. For the two principal plane patterns. Fig. 9.23 shows the normalized absolute value of the electric far field for $\varphi = 0^\circ$ in the dB scale of step 1. Fig. 9.26 shows the normalized absolute value of the electric far field for $\varphi = 90^\circ$ in dB scale of step 2. The blue lines show the analytic results obtained by using HOBBIES, red lines show the rectangular probe array measurement results.

10 USE AMPLITUDE ONLY DATA TO ENHANCE THE EFFICIENCY OF NF-FF METHOD

10.1 Objective and Necessity

In previous approaches, the near fields data are always complex numbers, it's very difficult to measure the complex data, especially in the high frequency cases, say at M, V and W-bands. The objective of this chapter is to show that we can still obtain acceptable far field results by using the amplitude only data of the near field measurements[28]-[33]. The square dipole array is an efficient option for near field amplitude measurement. This measurement is accomplished by putting the square dipole array at two different distances to the AUT and measure the amplitudes of the voltages of the dipoles of the array at these two measurement planes. Start with an initial guess of the phase information and after enough iterations to get the correct phases, we can obtain the final far field result. In every iteration, we need to solve the equivalent magnetic current over a plane near the original source antenna under test and then employ the Method of Moments approach to solve for the equivalent magnetic currents on this fictitious surface. Unlike in existing methods, the use of the probe array does not require probe correction. For this proposed methodology even though there is no need to satisfy the Nyquist sampling criteria in the measurement plane, a super resolution can be achieved in the solution of the equivalent magnetic current. Sample numerical results are presented to illustrate the accurate transformed far field result calculated from the near field measurement of amplitude data only.

10.2 Implementation of the Methodology

In this approach, instead of measuring the complex voltages $[V_x]$ & $[V_y]$, the near-field amplitude only measurements are performed over two planar surfaces which are both parallel with the source plane as shown in Fig. 10.1. The source plane (S_0), the measurement plane 1 (P_1) and the measurement plane 2 (P_2) are all assumed to be rectangular surfaces in the x-y plane with the same dimensions w by w .

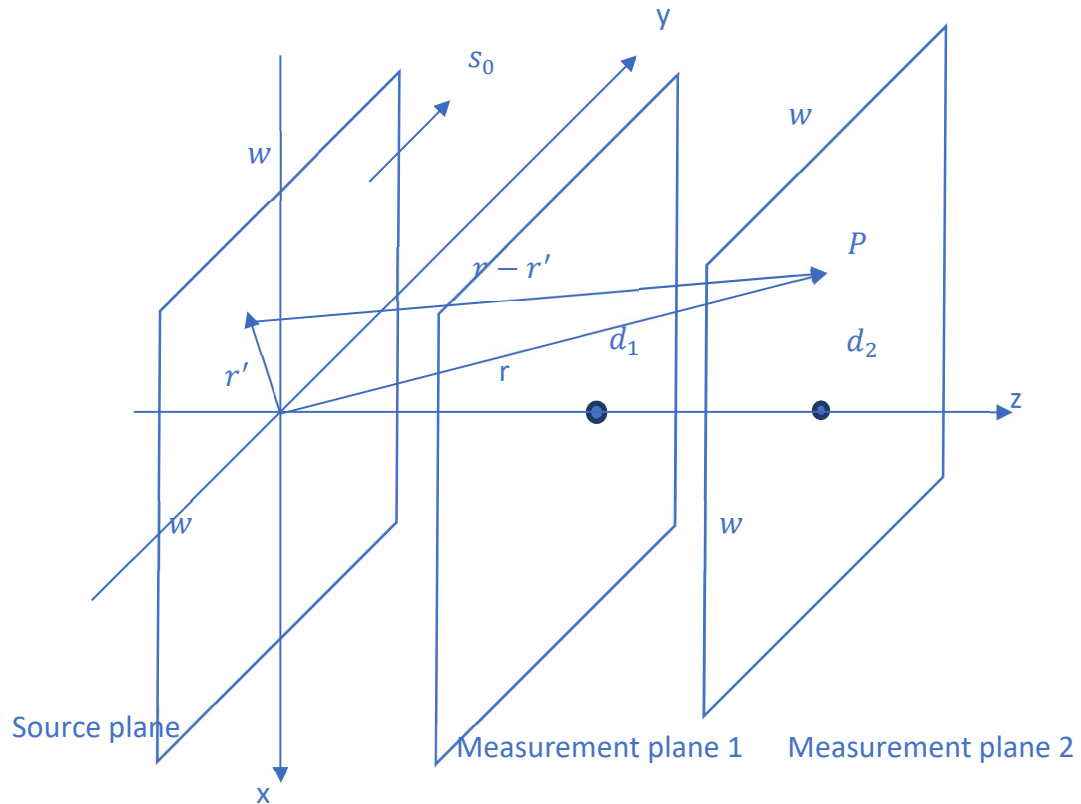


Fig. 10.1. Two planes measurement.

The amplitude of voltages measured on P_1 are called $[A_{1x}]$ & $[A_{1y}]$ (where we did the similar things to the general methods, we first make the dipoles in the array to be all x-directed and then also rotated the dipoles of the array to be all y-directed), the distance between S_0 and P_1 is called d_1 . The amplitude of voltages measured on P_2 are called $[A_{2x}]$ & $[A_{2y}]$, the distance between S_0 and P_2 is called d_2 . And then we made an initial guess of the phases on P_1 to be 0, so the voltages $[V_{1x}]$ & $[V_{1y}]$ on P_1 are assumed to be

$$[V_{1x}] = [A_{1x} * e^{j0}] \quad (10-1)$$

$$[V_{1y}] = [A_{1y} * e^{j0}] \quad (10-2)$$

according to these guessing voltages $[V_{1x}]$ & $[V_{1y}]$, we can further calculate M_x^1 & M_y^1 (where the number on the right corner represent the number of iterations) on the equivalent source plane, of course this equivalent magnetic currents are not accurate enough to represent the source, but we can use this M_x^1 & M_y^1 to calculate the complex voltages on P_2 , again, this is also not the accurate solution, but we had already measured the correct amplitudes of the voltages on P_2 ($[A_{2x}]$ & $[A_{2y}]$) and calculated the phases ($[\varphi_{2x}]$ & $[\varphi_{2y}]$) which are much closer to the real values than the initial guess. So, we combine the measured amplitudes ($[A_{2x}]$ & $[A_{2y}]$) and the calculated phases ($[\varphi_{2x}]$ & $[\varphi_{2y}]$) to represent the voltages on the P_2 , which is as follows,

$$[V_{2x}] = [A_{2x} * e^{j\varphi_{2x}}] \quad (10-3)$$

$$[V_{2y}] = [A_{2y} * e^{j\varphi_{2y}}] \quad (10-4)$$

by using this $[V_{2x}]$ & $[V_{2y}]$, we can obtain new equivalent magnetic currents M_x^2 & M_y^2 on S_0 , which are more accurate to represent the source. Then, we can keep doing this to update

the phases of the voltages on P_1 by combining the measured amplitudes ($[A_{1x}]$ & $[A_{1y}]$) and the calculated phases ($[\varphi_{1x}]$ & $[\varphi_{1y}]$) to get the new voltages $[V_{1x}]$ & $[V_{1y}]$ on P_1 , keep following this procedure and iterate enough times, we can obtain the accurate enough equivalent magnetic current on the source plane to calculate the far field. In the end, we compare the final far field results obtained from using the presented method with the results from an electromagnetic analysis code HOBBIES.

10.3 Example 10.1: Numerical results of choosing Horn antenna to be the AUT.

A 2λ by 2λ pyramidal horn antenna is used as the antenna under test.

The near-field amplitude only measurements are first performed over the measurement plane 1 (P_1) and then performed over the measurement plane 2 (P_2) by using an array of 15 by 15 0.1λ dipoles all terminated in $50\ \Omega$ loads and separated from each other by 0.2λ in both directions. The two planar surfaces P_1 and P_2 are both parallel with the source plane (S_0), as shown in Fig. 10.2 and Fig. 10.3. Fig. 10.2 shows the x-directed probe array measurement structure. Fig. 10.3 shows the side view of the structure by using the x-directed probe array as an example.

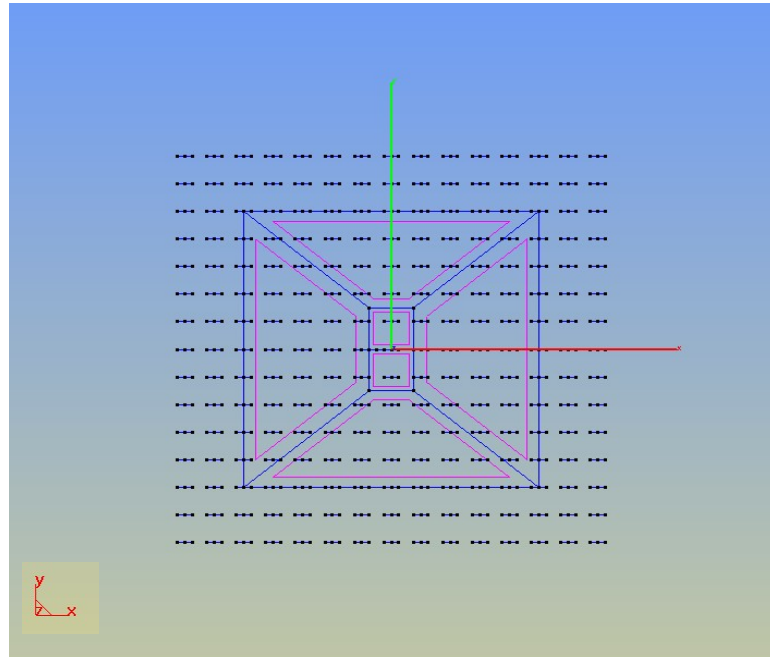


Fig. 10.2. x-directed probe array.

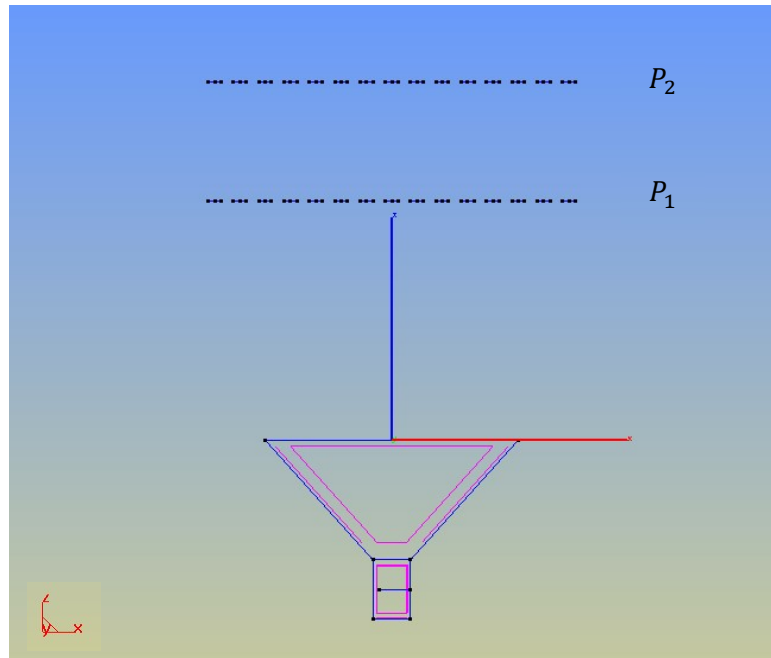


Fig. 10.3. x-directed probe array(side view).

In this case, S_0 , P_1 and P_2 are all rectangular surfaces in the x-y plane with the same dimensions 3λ by 3λ . On S_0 , the equivalent magnetic currents M_x and M_y are placed into 15×15 current patches and P_1 & P_2 are same discretized to enable the use of CGFFT. The distance between S_0 and P_1 is 2λ , and the distance between S_0 and P_2 is 3λ . Then we can obtain the far field results by using the method mentioned above from the amplitude only data measured on P_1 and P_2 .

The simulated results for the method mentioned above and the analytic results for the far fields are shown in Fig. 10.4 and Fig. 10.5. Fig. 10.4 shows the normalized absolute value of the electric far field for $\varphi = 0^\circ$ in the dB scale. Fig. 10.5 shows the normalized absolute value of the electric far field for $\varphi = 90^\circ$ in the dB scale.

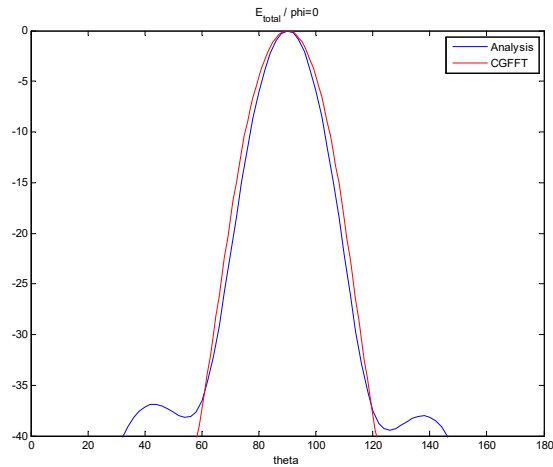


Fig. 10.4. E_{total} when $\phi = 0^\circ$ (dB Scale).

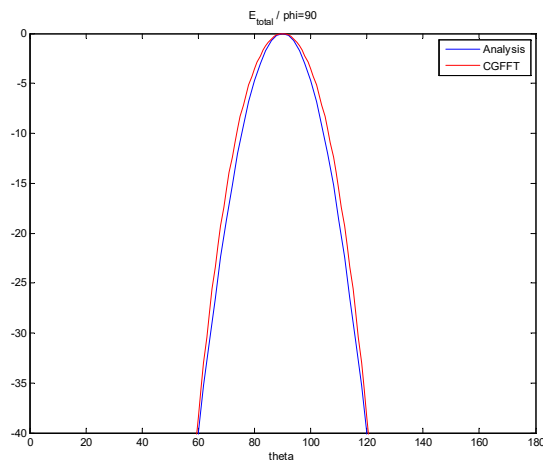


Fig. 10.5. E_{total} when $\phi = 90^\circ$ (dB Scale).

The blue lines show the analytic results obtained using HOBBIES, the red lines show the amplitude only data of probe array measurement results. We can see the method discussed above provides acceptable results. These results indicate that by utilizing only the amplitude of the complex data and not incorporating probe correction into the measurement have little effect on the accuracy of the final result.

10.4 Example 10.2: Numerical results of choosing Horn Array to be the AUT.

For the next example, the antenna under test is made more complicated. We choose 16, 1.5λ by 2λ pyramidal horn antennas to form a 4 by 4 horn antenna array as the antenna under test. Each horn is separated from each other by 3λ .

The near-field amplitude only measurements are first performed over the measurement plane 1 (P_1) and then performed the measurement plane 2 (P_2) by using an array of 40 by 40 0.1λ dipoles all terminated in 50Ω loads and separated from each other by 0.5λ in both directions. The two planar surfaces P_1 and P_2 are both parallel with the source plane (S_0), as shown in Fig. 10.6 and Fig. 10.7. Fig. 10.6 shows the x-directed probe array measurement structure and Fig. 10.7 shows the side view as an example.

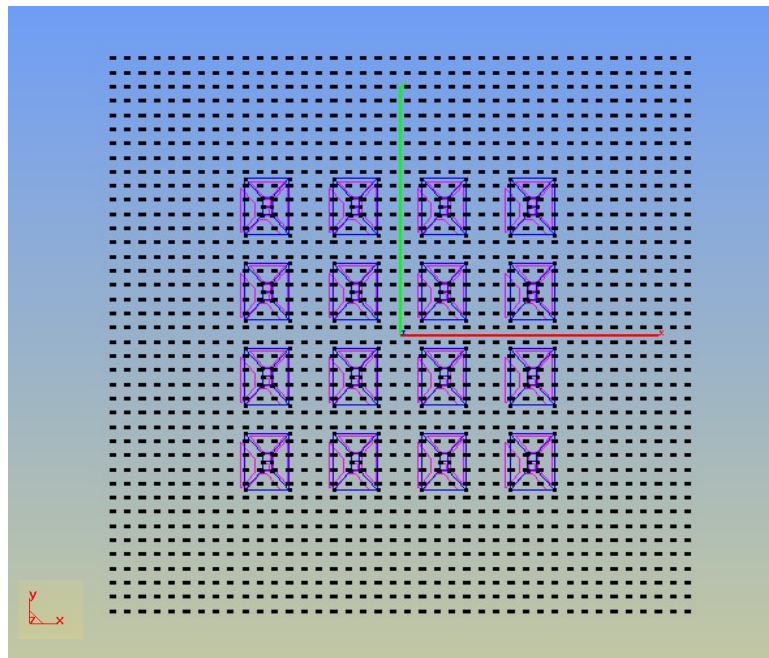


Fig. 10.6. x-directed probe array.

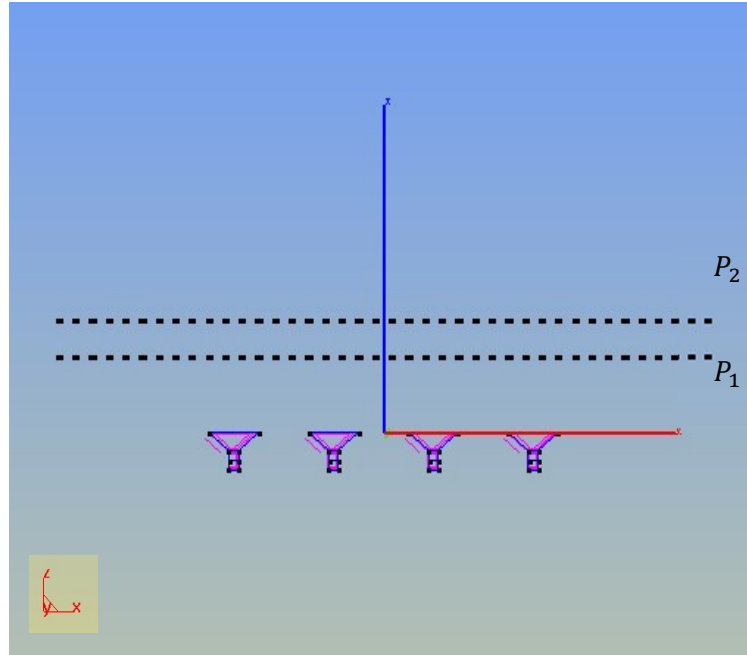


Fig. 10.7. x-directed probe array(side view).

In this case, S_0 , P_1 and P_2 are all rectangular surfaces in the x-y plane with the same dimensions 20λ by 20λ . On S_0 , the equivalent magnetic currents M_x and M_y are placed into 40×40 current patches and P_1 & P_2 are same discretized to enable the use of CGFFT. The distance between S_0 and P_1 is 2λ , and the distance between S_0 and P_2 is 3λ . Then we can obtain the far field results by using the method mentioned above from the amplitude only data measured on P_1 and P_2 .

The simulated results for the method mentioned above and the analytic results for the far fields are shown in Fig. 10.8 and Fig. 10.9. Fig. 10.8 shows the normalized absolute value of the electric far field for $\varphi = 0^\circ$ in the dB scale. Fig. 10.9 shows the normalized absolute value of the electric far field for $\varphi = 90^\circ$ in the dB scale.

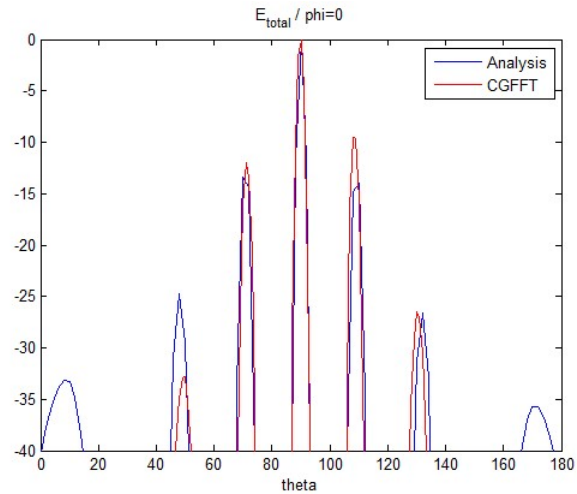


Fig. 10.8. E_{total} when $\phi = 0^\circ$ (dB Scale).

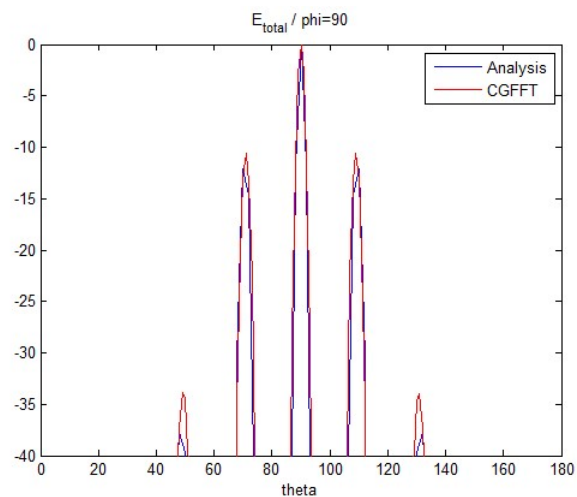


Fig. 10.9. E_{total} when $\phi = 90^\circ$ (dB Scale).

The blue lines show the analytic results obtained using HOBBIES, the red lines show the amplitude only data of probe array measurement results. We can see the method discussed above provides acceptable results. These results indicate that only by utilizing the amplitude of the complex data and not incorporating probe correction into the measurement have little effect on the accuracy of the final result.

10.5 Example 10.3: Numerical results of choosing Yagi antenna to be the AUT.

For the third example a single three element Yagi-Uda antenna is selected as the antenna under test to illustrate the accuracy of this methodology. This antenna has a wide beam. The three-element Yagi-Uda antenna as shown in Fig. 10.10 consist of a driven element of length $L = 0.47 \lambda$, a reflector of length 0.482λ , and a director of length 0.442λ . They are all spaced 0.2λ apart. The radius of the wire structure for all cases is 0.00425λ .

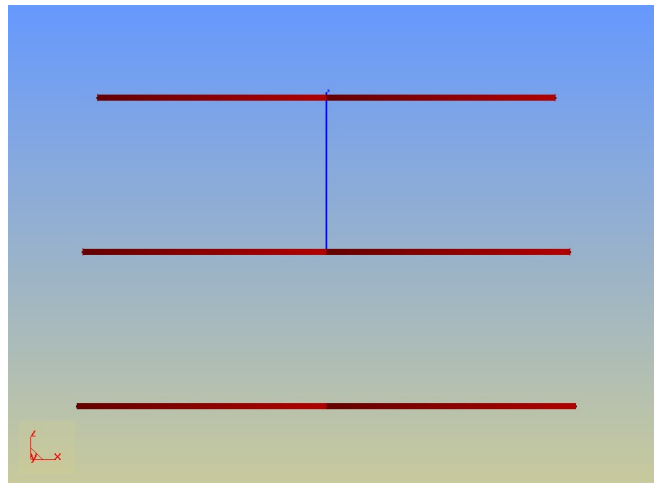


Fig. 10.10. A three-element Yagi-Uda antenna.

The measurement methodology for this Yagi-Uda antenna is quite similar to the measurement system used for the horn antenna as described in Example 10.1. The near-field amplitude only measurements are first performed over the measurement plane 1 (P_1) and then performed the measurement plane 2 (P_2) by using an array of 25 by 25 0.1λ dipoles all terminated in 50Ω loads and separated from each other by 0.2λ in both directions. The two planar surfaces P_1 and P_2 are both parallel with the source plane (S_0).

In this case, S_0 , P_1 and P_2 are all rectangular surfaces in the x-y plane with the same dimensions 5λ by 5λ . On S_0 , the equivalent magnetic currents M_x and M_y are placed into 25×25 current patches and P_1 & P_2 are same discretized to enable the use of CGFFT. The distance between S_0 and P_1 is 2λ , and the distance between S_0 and P_2 is 3λ . Then we can obtain the far field results by using the method mentioned above from the amplitude only data measured on P_1 and P_2 .

The simulated results for the method mentioned above and the analytic results for the far fields are shown in Fig. 10.11 and Fig. 10.12. Fig. 10.11 shows the normalized absolute value of the electric far field for $\varphi = 0^\circ$ in the dB scale. Fig. 10.12 shows the normalized absolute value of the electric far field for $\varphi = 90^\circ$ in the dB scale.

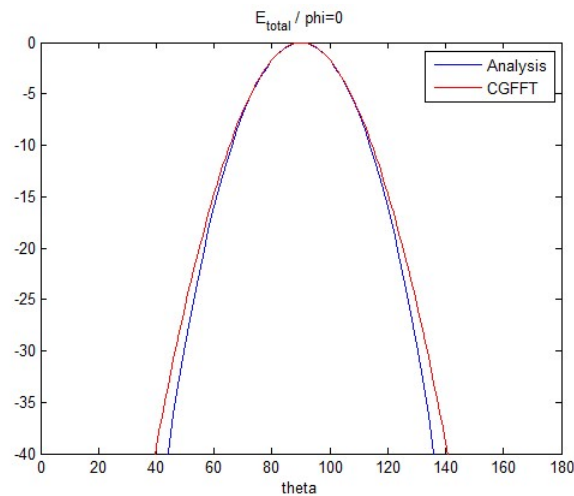


Fig. 10.11. E_{total} when $\phi = 0^\circ$ (dB Scale).

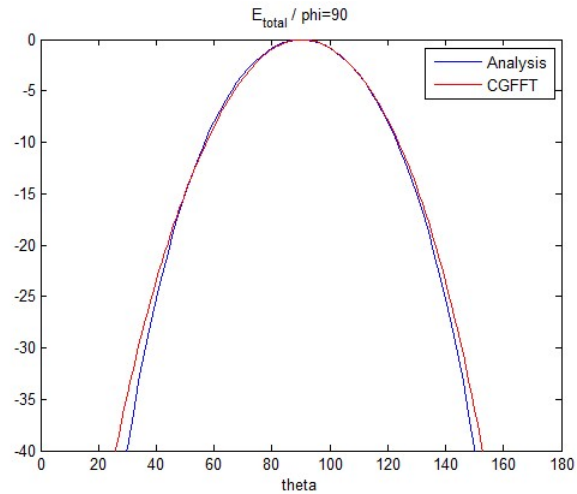


Fig. 10.12. E_{total} when $\phi = 90^\circ$ (dB Scale).

Theta here is defined as the angle from x axis to z axis and phi is the angle from the x axis to the y axis. This implies, phi equals 0° cut is the x-z plane and phi equals 90° is the y-z plane. The blue lines show the analytic results obtained using HOBBIES, the red lines show the amplitude only data of probe array measurement results.

We can see the method discussed above provides acceptable results. These results indicate that only by utilizing the amplitude of the complex data and not incorporating probe correction into the measurement have little effect on the accuracy of the final result.

10.6 Example 10.4: Numerical results of choosing Yagi Array to be the AUT.

For the final example, we deal with an array consists of 9 Yagi-Uda antennas to form a 3 by 3 antenna array as the antenna under test. Each element of the Yagi-Uda array has been described in example 10.3 and they are separated from each other by 2λ .

The near-field amplitude only measurements are first performed over the measurement plane 1 (P_1) and then performed the measurement plane 2 (P_2) by using an array of 40 by 40 0.1λ dipoles all terminated in 50Ω loads and separated from each other by 0.5λ in both directions. The two planar surfaces P_1 and P_2 are both parallel with the source plane (S_0), as shown in Fig. 10.13 and Fig. 10.14. Fig. 10.13 shows the x-directed probe array measurement structure and Fig. 10.14 shows the side view as an example.

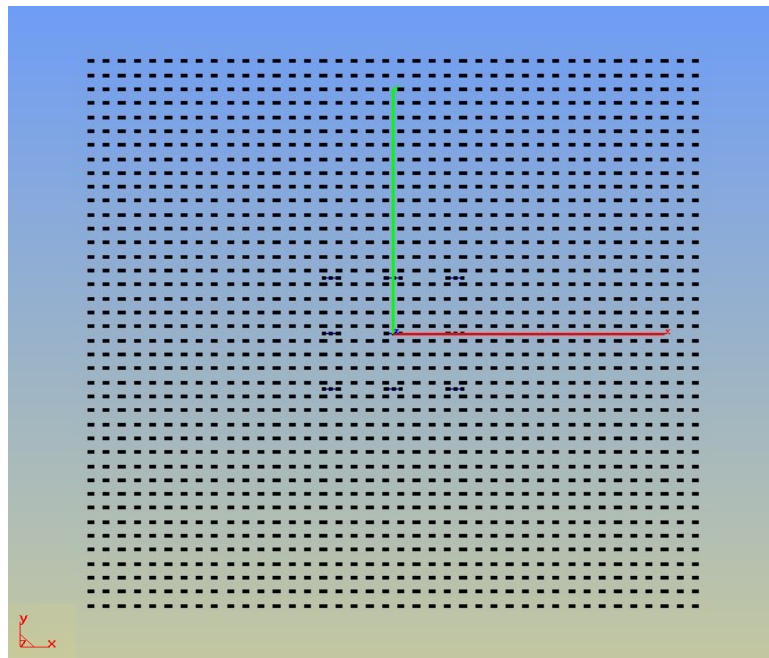


Fig. 10.13. x-directed probe array.

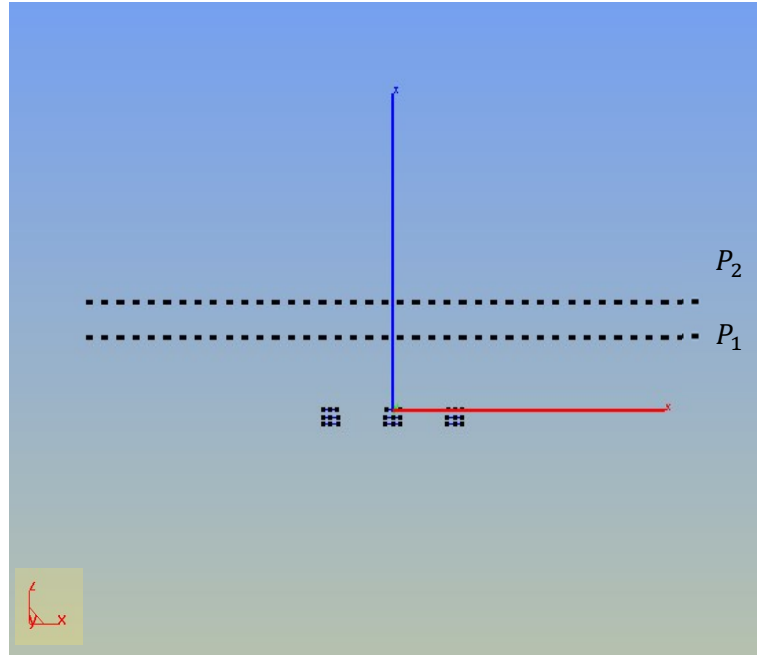


Fig. 10.14. A x -directed probe array (side view).

In this case, S_0 , P_1 and P_2 are all rectangular surfaces in the x - y plane with the same dimensions 20λ by 20λ . On S_0 , the equivalent magnetic currents M_x and M_y are placed into 40×40 current patches and P_1 & P_2 are same discretized to enable the use of CGFFT. The distance between S_0 and P_1 is 2λ , and the distance between S_0 and P_2 is 3λ . Then we can obtain the far field results by using the method mentioned above from the amplitude only data measured on P_1 and P_2 .

The simulated results for the method mentioned above and the analytic results for the far fields are shown in Fig. 10.15 and Fig. 10.16. Fig. 10.15 shows the normalized absolute value of the electric far field for $\varphi = 0^\circ$ in the dB scale. Fig. 10.16 shows the normalized absolute value of the electric far field for $\varphi = 90^\circ$ in the dB scale.

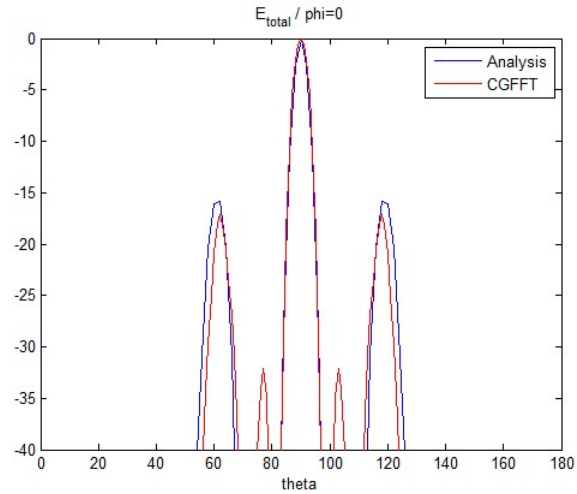


Fig. 10.15. E_{total} when $\phi = 0^\circ$ (dB Scale).

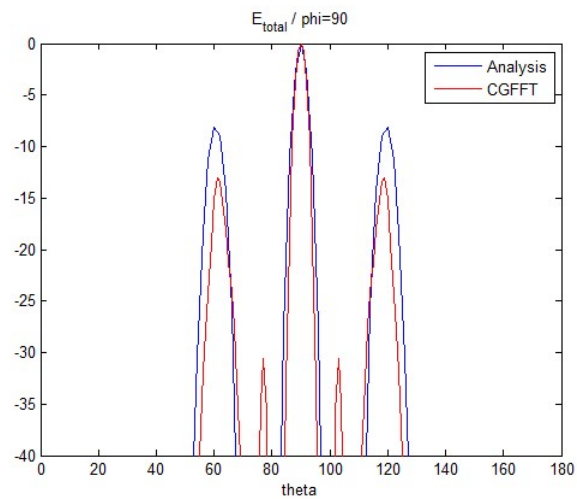


Fig. 10.16. E_{total} when $\phi = 90^\circ$ (dB Scale).

The blue lines show the analytic results obtained using HOBBIES, the red lines show the amplitude only data of probe array measurement results. We can see the method discussed above provides acceptable results. These results indicate that only by utilizing the amplitude of the complex data and not incorporating probe correction into the measurement have little effect on the accuracy of the final result.

11 CONCLUSIONS AND FUTURE WORK

A comparison was made between the calculated antenna patterns of two measurement systems by moving a single probe across the entire measurement plane as opposed to using a probe array to equivalently scan the entire surface of the measurement plane just once. For the results presented, both systems can obtain accurate results for the far field.

And if we take accuracy of mechanical movement of the probe antenna over a large planar surface into account, probe array measurement system would be more accurate. Also, probe array measurement can obtain all the information at once makes it to be more efficient than the single probe system. Hence, probe array measurement system is an accurate and efficient option to do the NF-FF transformation. The relation between the size of the square dipole probe array and the accuracy of the NF-FF pattern was analyzed, we found that as long as the sizes of the measurement planes are chosen to be approximately equal to or larger than the size of the actual source plane of the AUT, the accurate results can be obtained.

Also, for the efficiency consideration, two efficient approaches were introduced. The first approach of using a dipole planar probe array to measure the near field over a sector to obtain the far field pattern along principal planes was shown to increase the efficiency without sacrificing much accuracy. And another approach of making use of the amplitude only data of the near field measurements to predict the far field within engineering accuracy was also shown to speed up the measurements under high frequency environments. The remarkable point to note is that in this novel methodology probe correction is not deemed necessary according to all the results presented.

For the future work, as the rapid development of science and technology, I could apply new algorithm of solving the equations or try some other measurement systems to further increase the accuracy and efficiency of antenna pattern measurements.

REFERENCE

- [1] J. Brown and D.Sc., “The prediction of aerial radiation patterns from near-field measurements,” *Proceedings of the IEE - Part B: Electronic and Communication Engineering*, vol. 108, no. 42, pp. 635-644, Nov. 1961.
- [2] J. Hansen and F. Jensen, “Near-field measurements using directive antennas,” *Antennas and Propagation Society International Symposium*, vol. 8, pp. 284-287, Sep. 1970.
- [3] W. Leach and E. Joy, “Probe compensated near-field measurements: Basic theory, numerical techniques, accuracy,” *Antennas and Propagation Society International Symposium*, vol. 12, pp. 155-157, Jun. 1974.
- [4] D. Paris W. Leach “Basic theory of probe-compensated near-field measurements”, *IEEE Trans. Antennas Propagat.* vol. 26, no.3, pp. 373-379, May 1978.
- [5] A. Yaghjian, “An overview of near-field antenna measurements,” *IEEE Trans. Antennas Propagat.* vol. 34, no.1, pp. 30-45, Jan. 1986.
- [6] H. Chen and T. K. Sarkar, “Influence of the probe when computing far field from near field measurements,” *IEEE Conference on Antenna Measurement & Applications*, Jan. 2017, pp. 1-4.
- [7] H. Chen and T. K. Sarkar, “Using Planar Probe Array Near Field Measurement to Obtain Accurate Far Field Antenna Pattern Efficiently,” *IEEE International Conference on Computational Electromagnetics*, 2019.
- [8] H. Chen and T. K. Sarkar, “Use of Computational Electromagnetic to Enhance the Accuracy and Efficiency of Antenna Pattern Measurements”, *IEEE Journal on*

Multiscale and Multiphysics Computational Techniques, vol. 3, pp. 214-224, Dec. 2018.

- [9] H. Chen and T. K. Sarkar, "The Influence of the Size of Planar Probe Array Measurement on the Accuracy of NF-FF Pattern," submitted for publication to *IEEE Trans. Antennas Propagat.* 2019.
- [10] H. Chen and T. K. Sarkar, "A Fast and Efficient Methodology for Determining the Far Field Patterns of an Antenna along Principal Planes Using a Probe Array," submitted for publication to *IEEE Trans. Antennas Propagat.* 2019.
- [11] H. Chen and T. K. Sarkar, "Use Amplitude Only Data to Enhance the Efficiency of NF-FF Method," submitted for publication to *IEEE Trans. Antennas Propagat.* 2019.
- [12] P. Petre and T. K. Sarkar, "Planar Near-Field to Far-Field Transform Using an Equivalent Magnetic Current Approach," *IEEE Trans. Antennas Propagat.*, vol. 40, no. 11, pp. 1348-1356, Nov. 1992.
- [13] A. Taaghool and T. K. Sarkar, "Near-Field to Near/Far-Field Transformation for Arbitrary Near-Field Geometry, Utilizing an Equivalent Magnetic Current," *IEEE Trans. On Electromagnetic Compatibility*, vol. 38, no. 3, pp. 536-542, Aug. 1996.
- [14] C.A. Balanis, *Antenna Theory Analysis and Design*. John Wiley & Sons, 2005.
- [15] W.L. Stutzman, *Antenna Theory and Design*. John Wiley & Sons, 2013.
- [16] T. K. Sarkar, *Smart Antennas*, Wiley-IEEE Press 2003.
- [17] R.F. Harrington, *Time-Harmonic Electromagnetic Fields*. New York: McGraw-Hill, 1961

- [18] R.F. Harrington, "Matrix Methods for Field Problems," *Proceedings of the IEEE*, vol. 55, no. 2, pp. 136-149, Feb. 1967.
- [19] R.F. Harrington, *Computational Method for Electromagnetics*. Wiley-IEEE Press, 1997.
- [20] M.N.O. Sadiku, *Numerical Techniques in Electromagnetics*, CRC Press, 2009.
- [21] T. K. Sarkar, "On a class of finite step iterative methods for the solution of an operator equation arising in electromagnetics," *IEEE Trans. Antennas Propagat.*, vol. 33, no. 10, pp. 1058-1066, Oct. 1985.
- [22] T. K. Sarkar, E. Arvas, S. M. Rao, "Application of FFT and conjugate gradient method for the solution of electromagnetic radiation from electrically large and small conducting bodies," *IEEE Trans. Antennas Propagat.*, vol. 34, no. 5, pp. 635-640, May 1986.
- [23] T. K. Sarkar, Xiaopu Yang, "A limited survey of various conjugate gradient methods for solving complex matrix equations arising in electromagnetic wave interactions," *WAVE MOTION*, vol. 10, no. 6, pp. 527-546, Dec. 1988.
- [24] A. PeterSon and R. Mittra, "Convergence of the conjugate gradient method when applied to matrix equations representing electromagnetic scattering problems," *IEEE Trans. Antennas Propagat.*, vol. 34, no. 12, pp. 1447-1454, Dec. 1986.
- [25] A.V. Oppenheim and R. W. Shafer, *Digital Signal Processing*. Englewood Cliffs, NJ: Prentice-Hall, 1975.
- [26] J.C. Nash, *Compact Numerical Methods for Computers: Linear Algebra and Function Minimization*. John Wiley, 1979.

- [27] Y. Zhang and T. K. Sarkar, *High Order Basis Based Integral Equation Solver*. NJ: Wiley, 2012.
- [28] O. M. Bucci and G. D'Elia, "An Effective Near-Field Far-Field Transformation Technique from Truncated and Inaccurate Amplitude-Only Data," *IEEE Antennas and Propagation*, vol. 47, no. 9, pp. 1377-1385, Sep. 1999.
- [29] M. D. Migliore and F. Soldovieri, "Far-Field Antenna Pattern Estimation from Near-Field Data Using a Low-Cost Amplitude-Only Measurement Setup," *IEEE Transactions on Instrumentation and Measurement*, vol. 49, no. 1, pp. 71-76, Feb. 2000.
- [30] S. Costanzo and G. Di Massa, "A Novel Hybrid Approach for Far-Field Characterization From Near-Field Amplitude-Only Measurements on Arbitrary Scanning Surfaces," *IEEE Antennas and Propagation*, vol. 53, no. 6, pp. 1866-1874, Jun. 2005.
- [31] T. Brockett and Y. Rahmat-Samii, "A Novel Portable Bipolar Near-Field Measurement System for Millimeter-Wave Antennas: Construction, Development, and verification," *IEEE Antennas and Propagation*, vol. 50, no. 5, pp. 121-130, Oct. 2008.
- [32] F. Las-Heras and T.K. Sarkar, "A Direct Optimization Approach for Source Reconstruction and NF-FF Transformation Using Amplitude-Only Data," *IEEE Transactions and Propagation*, vol. 50, no. 4, pp. 500-510, Apr. 2012.
- [33] S. F. Razavi and Y. R. Samii, "Phaseless Measurements Over Nonrectangular Planar Near-Field Systems Without Probe Corotation," *IEEE Antennas and Propagation*, vol. 61, no.1, pp. 143-152, Jan. 2013.

Biographical Data

Name of Author: Heng Chen

Date and Place of Birth: Feb 13, 1990, Wuhu, Anhui Province, China

Education

2008 - 2012	B.E., Anhui Agricultural University
2012 - 2014	M.S., Syracuse University

Awards and Honors:

2014	Chair of Graduate Student Committee, IEEE Syracuse University Student Branch.
2013 & 2014	Inducted as a member of Golden Key International Honor Society.
2013	Inducted as a member of the Alpha Sigma Chapter of Phi Beta Delta.

Employment

May 2018 - Aug 2018	Research Foundation for SUNY of New York at Oswego
May 2017 - Aug 2017	PPC Co-op Position
May 2016 - Aug 2016	Arcom Co-op Position
Oct 2013 - Mar 2014	Anaren Co-op Position
From 2014	Teaching assistant and research assistant at Syracuse University

Publications

Journal

- [1] H. Chen and T. K. Sarkar, "Use of Computational Electromagnetic to Enhance the Accuracy and Efficiency of Antenna Pattern Measurements," *IEEE Journal on Multiscale and Multiphysics Computational Techniques*, vol. 3, pp. 214-224, Dec. 2018.
- [2] H. Chen and T. K. Sarkar, "The Influence of the Size of Planar Probe Array Measurement on the Accuracy of NF-FF Pattern," submitted for publication to *IEEE Trans. Antennas Propagat.* 2019.
- [3] H. Chen and T. K. Sarkar, "A Fast and Efficient Methodology for Determining the Far Field Patterns of an Antenna along Principal Planes Using a Probe Array," submitted for publication to *IEEE Trans. Antennas Propagat.* 2019.
- [4] H. Chen and T. K. Sarkar, "Use Amplitude Only Data to Enhance the Efficiency of NF-FF Method," submitted for publication to *IEEE Trans. Antennas Propagat.* 2019.
- [5] T. K. Sarkar and H. Chen, "Physics-Based Modeling of Experimental Data Encountered in Cellular Wireless Communication," *IEEE Trans. Antennas Propagat.* vol. 66, no. 12, pp. 6673-6682, Dec. 2018.
- [6] T. K. Sarkar and H. Chen, "Lessons Learnt through using a Physics Based Macro Model for Analysis of Radio Wave Propagation in Wireless Transmission," *IEEE Trans. Antennas Propagat.* vol. 67, no. 4, pp. 2150-2157, Jan. 2019.

- [7] M. Zhu, T. K. Sarkar and H. Chen, "On the Stability of Time-Domain Magnetic Field Integral Equation using Laguerre Functions," accepted for publication in *IEEE Trans. Antennas Propagat.* Feb. 2019.
- [8] M. Zhu, T. K. Sarkar and H. Chen, "A Stabilized Marching-on-in-Degree Scheme for the Transient Solution of the Electric Field Integral Equation," accepted for publication in *IEEE Trans. Antennas Propagat.* Feb. 2019.

Conference

- [1] H. Chen and T. K. Sarkar, "Using Planar Probe Array Near Field Measurement to Obtain Accurate Far Field Antenna Pattern Efficiently," *IEEE International Conference on Computational Electromagnetics*, 2019.
- [2] H. Chen and T. K. Sarkar, "Influence of the probe when computing far field from near field measurements," *IEEE Conference on Antenna Measurement & Applications*, Jan. 2017, pp. 1-4.